Pulsed Nd:YAG Laser Processing of Nitinol

by

Mohammad Ibraheem Khan

A thesis
presented to the University of Waterloo
in fulfillment of the
thesis requirement for the degree of
Doctor of Philosophy
in
Mechanical Engineering

Waterloo, Ontario, Canada, 2011

I hereby declare that I am the sole author of this thesis. This is a true copy of the thesis, including any required final revisions, as accepted by my examiners. I understand that my thesis may be made electronically available to the public.

ABSTRACT

The excellent pseudoelasticity, shape memory and biocompatibility of Nitinol have made it a leading candidate for applications in various fields, including aerospace, micro-electronics and medical devices. Challenges associated with laser processing need to be resolved before its full potential in practical applications can be realized. The current thesis details the effects of pulsed Nd:YAG laser processing on Ni-rich (Ni-49.2. at.% Ti) Nitinol.

First, the mechanical, pseudoelastic and cyclic loading properties for varying process parameters have been compared to those of the base metal. Process parameters were shown to greatly influence the mechanical performance. This was due to local yielding occurring within the processed material during tensile straining. In addition, laser processed samples showed higher permanent residual strain and exhibited a slightly higher efficiency for energy storage during the initial 5 cycles compared to base material. Fracture surfaces of base material revealed ductile dimpled surfaces while welded specimens exhibited both brittle (low peak power) and ductile (high peak power) failure modes.

DSC analyses conducted on the processed metal revealed additional high temperature transformation peaks. These peaks were attributed to the local phase conversion induced by laser processing. Further corroboration was made with room temperature XRD analysis, showing only austenite in the base metal and added martensite peaks in the melted metal. Temperature controlled TEM observations confirmed high temperature transformation peaks to be associated with processed metal. Furthermore, TEM analysis aided in identifying the submicron second phase particles observed in fracture surfaces as Ti_2Ni.

Finally, local phase conversion was correlated to change in local chemical composition. Preferential vaporization of nickel was determined to cause the change in Ni/Ti ratio. This in turn explained the altered mechanical performance and presence of the Ti-rich intermetallic (Ti_2Ni). Consequently, a novel method using a high power density energy

source to alter transformation temperature of shape memory alloys (SMA's) was developed. Results were used to successfully demonstrate a novel technology that can embed additional memories in Nitinol and other SMA's. Possessing the ability to control local transformation temperatures and as a result the shape memory effect of SMA's promises to enhance their functionality while enabling new applications to be realized.

ACKNOWLEDGEMENTS

I would like to sincerely thank my supervisor, Dr. Norman Zhou. I appreciate the freedom he gave me to pursue my academic interests, as well as the guidance and insight that was provided when needed. I am grateful for the opportunity to have worked with him during the period of this study.

I will also never forget the support of Dr. Lawson, whose infectious enthusiasm and guidance was always present. I would also like to thank my friends who have supported me throughout the years. I have learned so much about myself from each and every one of you. My sincerest thank you to the members of the Centre for Advanced Materials Joining (CAMJ).

This work has been supported by the Natural Sciences and Engineering Research Council of Canada (NSERC).

To my wonderful and loving family.

TABLE OF CONTENTS

LIST OF FIGURES

LIST OF TABLES

1. INTRODUCTION

1.1 Background

The unique properties of shape memory alloys have resulted in numerous applications, including couplings and fasteners, actuators and wear resistant components [1]. In particular, its excellent biocompatibility coupled with good strength and ductility has made Nitinol an attractive candidate for medical device applications. Laser processing (i.e. surfacing, ablation, welding, etc.) is a key fabrication step in the manufacture of many devices. However, difficulties associated with reduced mechanical performance after laser processing has limited its implementation for many vital components. Some of these issues have been detailed in two separate publications by Falvo et al. and Chau et al., both of which have expressed a need for further research before practical applications of NiTi can be achieved [2,3]. Hence, research detailing the effects of laser processing on Nitinol is essential to overcome many of these challenges. By clarifying its effects on this material, many more potential applications can be considered.

The interest and implementation of SMA in biomedical applications has increased in recent years. Temperature dependent characteristics of its functional properties, which make it disadvantageous in certain applications, are not critical due to the stable temperature maintained by the human body. Furthermore, specific surface treatments have been shown to greatly improve the biocompatibility of NiTi [4]. In many cases, laser processing techniques, such as welding, are implemented for the fabrication of miniature devices. For example, Figure 1-1 shows microscopic forceps utilized in endoscopic brain surgery, which are connected to 0.63 mm wire using laser welding. However, laser processing of Nitinol is generally difficult, which in turn limits flexibility in the design and fabrication of Nitinol devices and hence impedes high volume commercialization of the alloys.

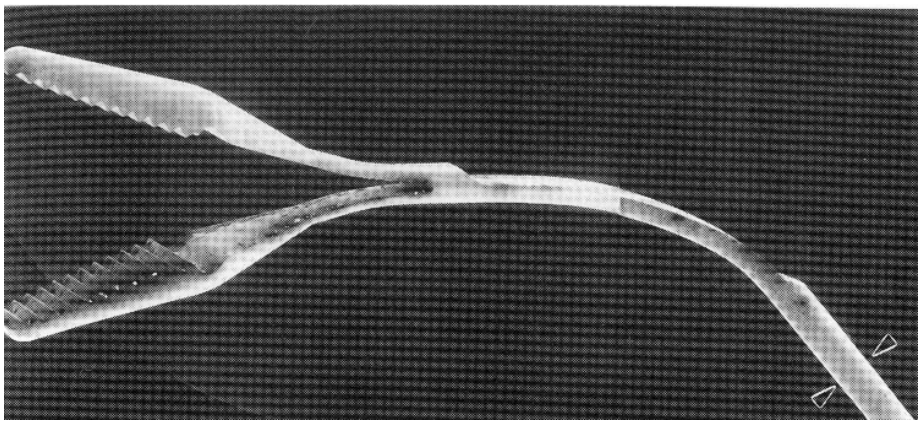

Figure 1-1: Laser welded microforceps made from Nitinol [5]

The initial aim of this thesis was to investigate pulsed Nd:YAG laser welding, more specifically for medical device applications. As a result, processing conditions mimicking those applied to create small scale welds were utilized for investigation. However, results revealed a clear change in microstructure and thermal properties which were applicable to more than just welding procedures. Moreover, these changes were determined to be controllable and have potential to revolutionize the applications of shape memory alloys as a whole using laser processing techniques. Hence the term “laser processing” was adopted as opposed to “laser welding”

1.2 Objectives

In the current work, the pulsed Nd:YAG laser processing of Nitinol has been studied with the aim of improving the understanding of its effects on the base metal. More specifically, the following work has been undertaken:

1) To clarify the effects of pulsed Nd:YAG laser processing on the room temperature mechanical performance, including pseudoelasticity and cyclic loading.
2) To document the effects of laser processing on the microstructure and solid-state phase transformation behavior.
3) To identify mechanisms responsible for the changes in properties and microstructure.

1.3 Justification

The knowledge and engineering know-how developed in this proposed work will make significant contributions to the science and technology of all aspects of Nitinol laser processing. In particular, the effects of laser processing parameters on the structure and subsequent properties of Nitinol alloys are essential before its full potential can be exploited. This work will provide a platform to help create engineering guidelines that optimize the process conditions. Ultimately this will increase flexibility for the design and fabrication of Nitinol devices. Finally this work will also foster development of laser processing expertise, as needed by manufacturing industries.

1.4 Criteria and Constraints

This work is limited to uncoated medical grade Nitinol with near equiatomic chemical compositions having thicknesses near 0.4 mm. This study is also limited to full penetration so that processing is conducted through the sheet thickness. Peak power inputs have ranged between 0.3 and 40 watts. Furthermore, all tests conducted on the mechanical performance are limited to room temperature. These constraints are based on material availability and equipment limitations.

As a result of knowledge gained in literature, the following principles were adopted for the experimental design: i) off-stoichiometric TiNi alloys should be quenched after high-temperature solution treatment to ensure that the obtained metastable martensite maintains the same composition as the parent phase (without precipitation of Ni_3Ti or Ti_2Ni) ii) the intermediate R-phase transition should also be avoided iii) interstitial atoms such as 0, N, and C should be kept as low as possible (e.g. by using inert shielding gas during annealing and during laser processing).

The assessment of base material Nitinol in this research is based upon the “American Society for Testing and Materials” (ASTM) recommendations, which have been closely followed [6,7,8,9,10]. For instance, transformation temperatures were determined by closely following ASTM F2004 "Standard Test Method for Transformation Temperature of Nickel-Titanium by Thermal Analysis"

1.5 Major Results and Contributions

1.5.1 Key Results

Local Yielding:

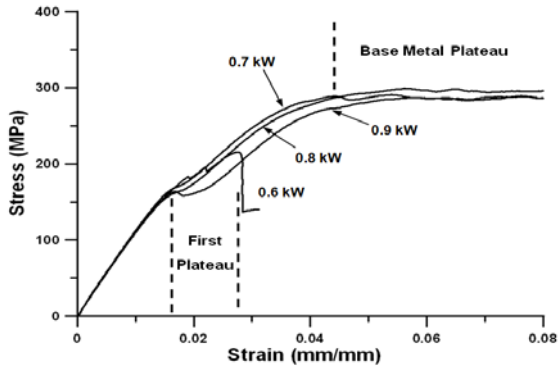

Transverse micro-tensile coupons enabled the characterization of local yielding prior to the onset of pseudoelastic behavior. This result, referred to as the 'initial plateau', led to higher permanent residual strain and improved efficiency of energy storage. Furthermore, it showed a distinct change in mechanical performance which needs to be considered in the design and fabrication of Nitinol devices implementing laser processing techniques.

Change in local composition:

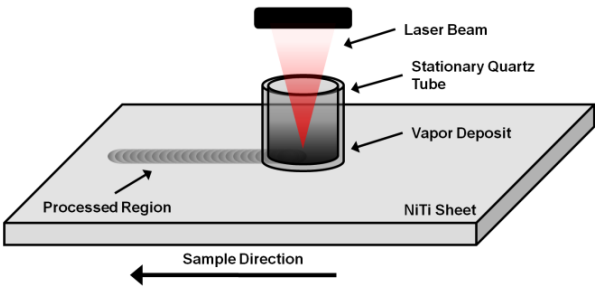

Local vaporization induced by laser processing was determined to preferentially remove nickel. This was done by capturing and analyzing the vapour using a quartz tube. The lower vapour pressure of nickel as compared to titanium was the primary cause for its evolution. This ultimately altered the local composition and transformation temperatures. Similarly to the altered mechanical performance, this change in transformation properties needs to be considered in applications exploiting the shape memory effects of Nitinol alloys.

Multi-Memory Material Technology:

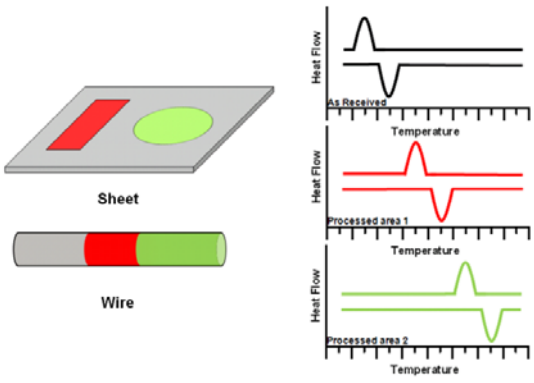

The discovery of locally modified transformation temperatures has led to the creation of the Multi-Memory Technology. This technology enables monolithic shape memory alloys to have additional memories (transformation temperatures) embedded in them by selectively vaporizing constituents to alter local chemistry. The precision and control provided by the laser processing system allows a user to predetermine the required transformation temperature. A proof-of-principle of this technology was provided with the development of several prototypes. Multi-Memory Material technology has the potential to revolutionize the manufacturing of SMA products.

1.6 Organization of Thesis

This thesis is subdivided into eight chapters. Chapter 2 provides the reader with a fundamental understanding of both Nitinol and pulsed Nd:YAG laser processing methods. In particular the unique functional properties of Nitinol alloys are detailed. The current “state of the art” in laser processing of Nitinol and associated shortcomings are reviewed.

Chapter 3 provides details on experimental methods and conditions, including material, test equipment and procedures.

Chapter 4 reports the mechanical performance of laser processed Nitinol for select processing conditions, as compared to the base metal. It shows results for the stress strain behavior, pseudoelasticity, cyclic loading and micro-hardness. Scanning electron microscopy (SEM) was also implemented to analyze the sample fracture surfaces.

Chapter 5 documents investigations of the influence of select laser processing conditions on the microstructure and phase transformation of Nitinol. More specifically, representative samples exhibiting high, low and intermediate tensile performance were studied. Differential scanning calorimetery was implemented to identify changes in the transformation temperatures of processed and base metal samples. Metallographic characterization was conducted using optical and transmission election microscopy (TEM). Temperature controlled TEM facilitated the in-depth characterization of altered transformation temperatures. Moreover, results enabled a correlation between the observed local microstructure and mechanical properties detailed in Chapter 4.

Chapter 6 describes investigation of the possible factors responsible for altering transformation temperatures. Process parameters were isolated and tested in order to determine their effects. Further experimental testing was conducted to validate the cause of altered transformation temperatures. Finally, this chapter correlates the mechanism involved with the final nonstructural analysis.

Chapter 7 provides a proof-of-principle for the new Multi Memory Material Technology developed from this work. Three unique prototypes created using laser processing techniques are displayed.

Finally, Chapter 8 lists the conclusions and provides recommendations for future research.

2. LITERATURE REVIEW

Both Nitinol and laser processing techniques were first discovered in the 1960's and have been rapidly integrated in various applications. Over the past 50 years, advances have been and continue to be made. Nonetheless, compared to conventional alloys and processing techniques, both are still in their infancy. The aim of the current chapter is to provide a brief review of SMA's and fundamental details on the pulsed Nd:YAG laser processing techniques. In addition, some of the current challenges faced with applying laser processing techniques to Nitinol will be discussed.

2.1 Nitinol shape memory alloy

The near equatomic Nitinol intermetallic compound (IMC) was first discovered in 1963 by Beuhler et al. [11]. Unlike conventional IMCs, the alloy belongs to a class of special materials called shape memory alloys (SMA) which when properly processed, exhibits pseudoelastic and shape memory properties. Similar effects were detailed earlier in other alloys (Cu-Zn-Al, Cu-Al-Ni, and Au-Cd) [12,13]; however the better mechanical properties of Nitinol alloys brought them more acclaim. Other advantages of Nitinol compared to the other SMA's include its low elastic anisotropy, high electrical resistivity, and good corrosion resistance [14]. Since its discovery, Nitinol has revolutionized many traditional engineering designs with greater functional capacity for products such as stents and actuators.

The functional properties of Nitinol and other SMA's are closely linked to their reversible diffusionless solid-solid phase transformations. The primary phases involved include a simple cubic high temperature austenite phase (Figure 2-1a) and monoclinic low temperature martensite phase (Figure 2-1b). Transformation temperatures for alloys can range from -150^{o}C to 200^{o}C, which is mainly dependent on the chemical composition and thermomechanical pressing. These transformations can be induced either thermally (i.e. temperature change) or via mechanical deformation. In either case,

they undergo a martensitic transformation that underlies Nitinol's unique mechanical behavior and needs to be clearly understood [17].

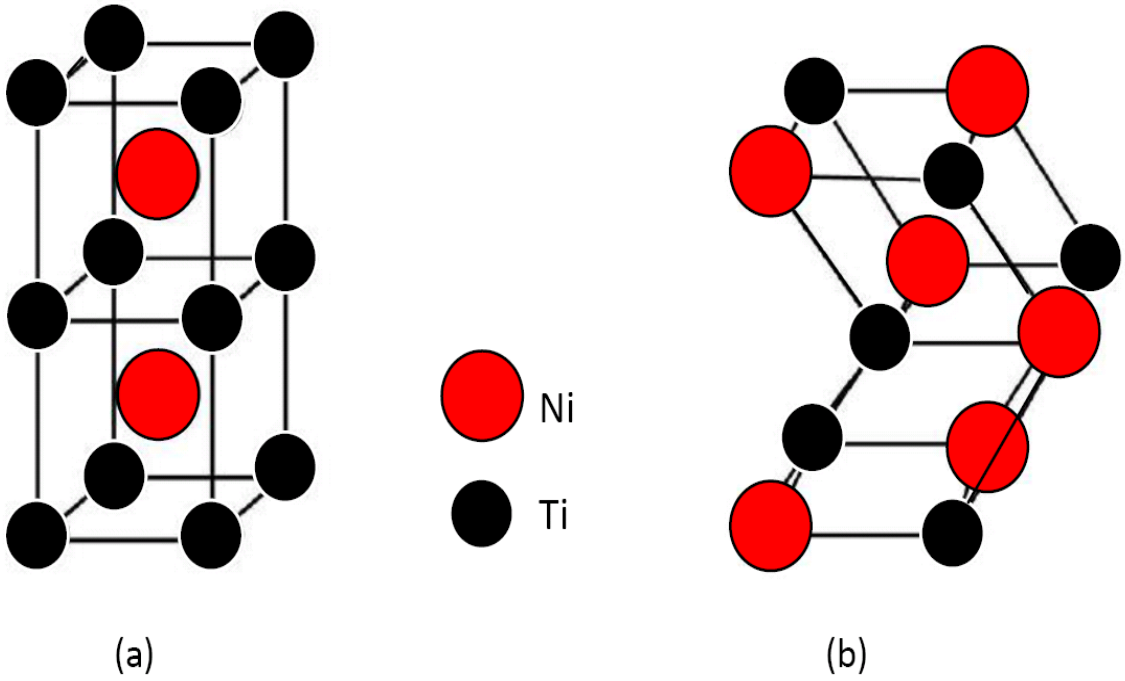

Figure 2-1: Lattice structure of (a) austenite and (b) martensite

2.1.1 Martensitic Transformation

Martensitic transformations are diffusionless and military in nature and commonly experienced in steel alloys. Macroscopic changes in dimension during transformation have to be self-accommodated by either slip or twinning, a schematic of which is shown in Figure 2-2. Slippage of lattice planes is an irreversible process, which is capable of accommodating both shape and volume changes (Figure 2-2a). Furthermore, during atomic slip, bonds are typically broken resulting in a change in atomic arrangements. Twinning only accommodates a shape change, but is reversible (Figure 2-2b). During thermally-induced martensitic transformation in steel, atomic rearrangement in the new

phase inherits a different shape and volume associated with slip. In contrast, Nitinol undergoes reversible twinning and experiences only a shape change.

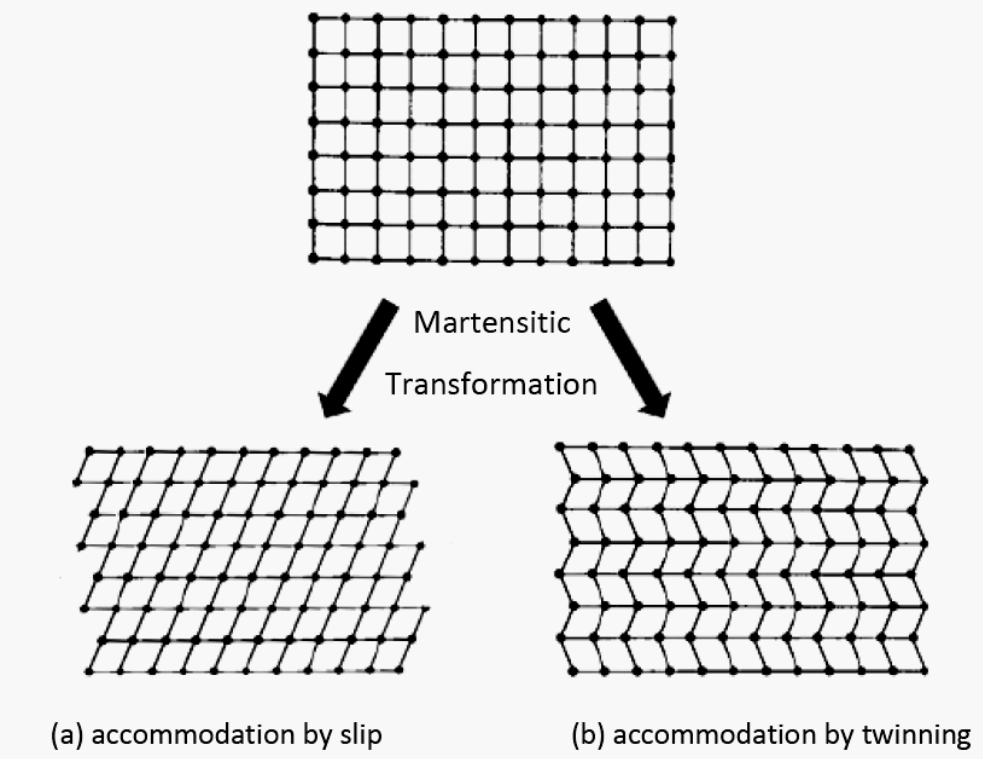

Figure 2-2: Schematic representation of the atomic motions associated to the self-accommodation step of a martensitic transformation: (a) by slip and (b) by twinning [17]

Twinning is the creation of mirrored structures as a result of atomic displacement across a particular atomic plane [17]. Atoms situated at the twin boundary see the same number and types of bonds in both directions [17]. As opposed to accommodation by slip, bonds are not broken during the twinning process. For this reason, twin boundaries have low energy and are highly mobile. Figure 2-3 shows twin boundaries reorienting themselves from one orientation to another in favour of the direction of applied stress, also known as detwinning [17,23]. During reorientation of the martensitic structure from twin variants to a single variant, a large amount of strain can be produced. This unusual mechanical response is macroscopically represented by a stress plateau in a stress-strain curve. The twin movement process can accommodate limited martensitic

deformation and exceeding it will result in permanent plastic deformation of the structure.

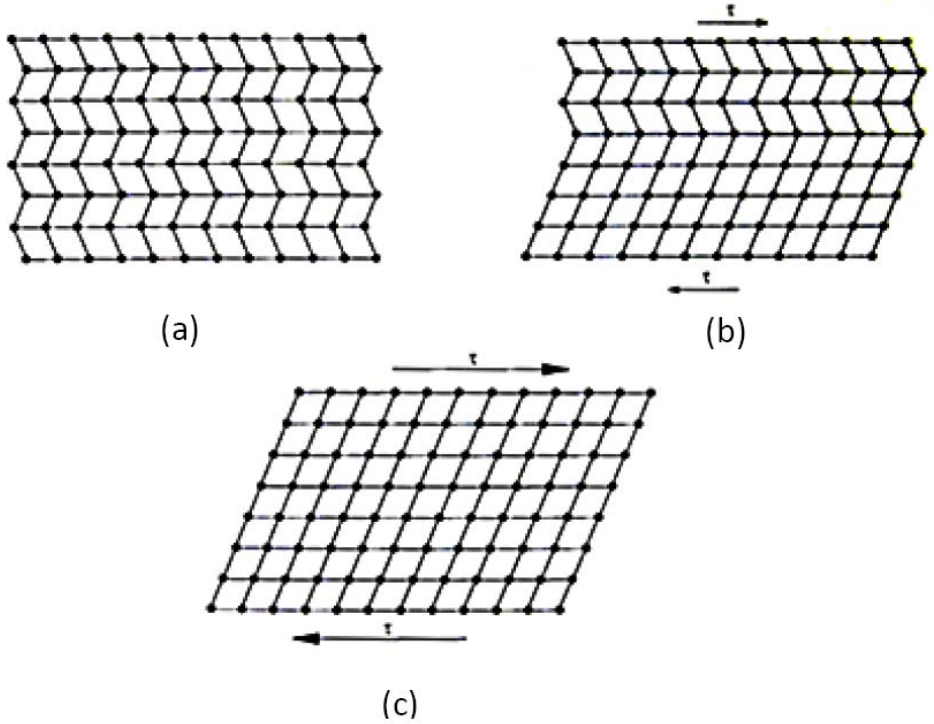

Figure 2-3: During the application of a shear stress, the twin structure can readily move to accommodate the strain by undergoing a detwinning process [17]

2.1.2 Temperature Induced Transformation

Reversible transformations occurring with temperature change are typically characterized by four temperatures; including austenite start (A_s) and austenite finish (A_f) during heating and martensite start (M_s) and martensite finish (M_f) during cooling. A_s and A_f indicate the start and finish of martensite to austenite, while M_s and M_f describe the reverse austenite to martensite transformation. For simplification, the onset of martensite, M_s, temperature is generally used for classification purposes. A schematic showing the volume fraction transformed as a function of temperature is shown in Figure 2-4. Temperature spans for complete transformation can typically range 5K-30K. Temperatures differences associated with the overall hysteresis of transformation are in the range of 10K-50K [18]. Transformation hysteresis is known to result from the frictional force experianced during lattice movement across interfaces and defects [14].

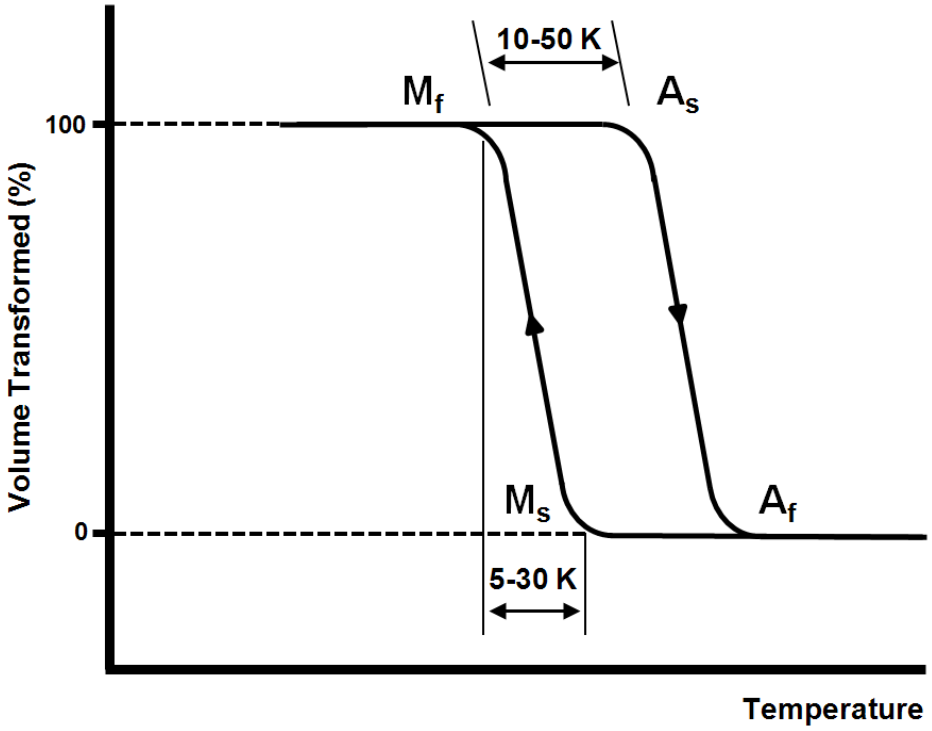

Figure 2-4: Schematic of the volume transformed as a function of temperature [19].

Transformation temperatures are largely influenced by metallurgical factors which influence the elastic strain energy and frictional resistance for transformation, and chemical composition [72]. Metallurgical factors are more prominent in materials that have undergone thermo-mechanical processing. Thermo-mechanical processing is an effective way to modify the phase transformation behaviour of Nitinol, a technique often employed to achieve better mechanical properties. In particular, cold working gives higher yield strength, but can alter other functional properties since it hinders the mobility of twin boundaries.

The Ni/Ti ratio plays a significant role in the Nitinol transformation temperature. The strong dependence of transformation temperature on composition has been closely linked to the altered lattice dynamics and elastic constant [15]. Sensitivity to composition change has been shown to be severe in the nickel-rich alloys, with changes of 1at. % altering M_s temperature by as much as 250^{o}C [15, 23]. In the past, many attempts to correlate Nitinol composition with M_s temperature were made [16,17,18]. Figure 2-5 shows the evolution of data and predictions regarding M_s temperature as a function of

Ni content for quenched binary NiTi starting from 1973. It was generally accepted that a decrease in M_s temperature occurred as Ni content increased, although data in earlier literature [16] for the Ti-rich domain was later proven to be incorrect. This correlation was refined in more recent literature by Tang who showed the composition dependence using calculated thermodynamic properties and experimental data. This correlation, shown in Figure 2-5c, has been largely adopted as the correct one. It showed that the Ti-rich side is almost horizontal near 65°C while on the Ni-rich side a linear decrease is seen. Hence, transformation temperatures are largely influenced by Ni content in the Ni-rich Nitinol alloys.

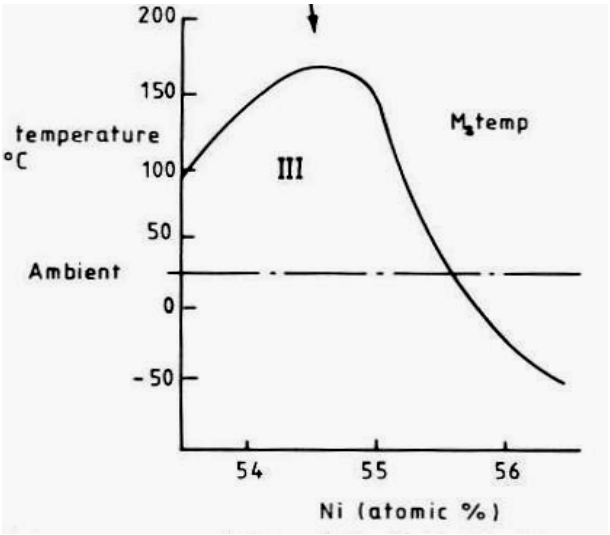

a) From 1973 by Hawkins [16]

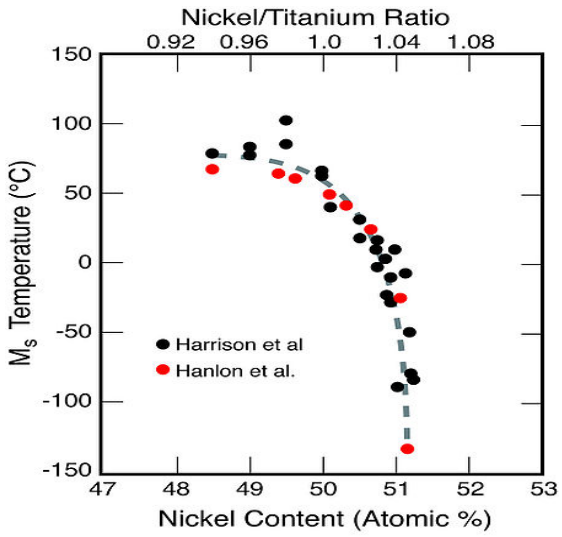

b) From 1990 by Duerig [17]

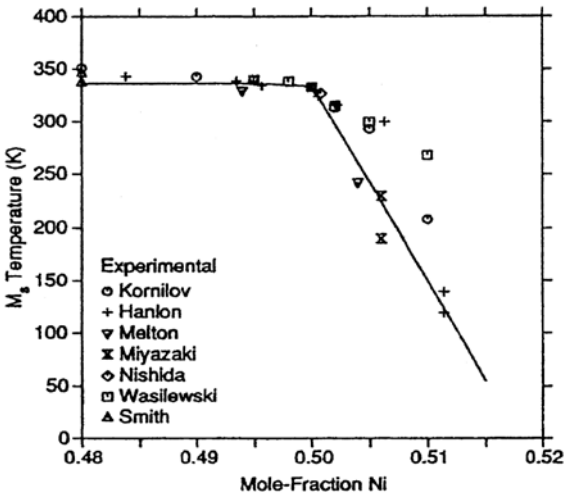

c) From 1997 by Tang [18]

Figure 2-5: M_s Temperature as a function of Ni content for binary NiTi

2.1.3 Stress-strain Behavior and Pseudoelasticity

Figure 2-6a shows a typical stress-strain curve until fracture for pseudoelastic base metal consisting of three distinct deformation zones: elastic (region 1), pseudo-elastic (region 2) and plastic deformation (region 3). At temperatures above M_s, the pseudoelastic properties of Nitinol enable it to be strained beyond the linear elastic (region 1) portion on a stress-strain curve while undergoing phase transformation. The applied stress transforms the austenite parent phase to martensite which is termed stress induced martensite (SIM). Upon removal of stress within region 2 most of the mechanically induced martensite reverses back to austenite, as shown in Figure 2-6b. However some permanently transformed martensite results in remaining residual strain. The magnitude of pseudoelastic strain for Nitinol can reach 13% [19]. Straining beyond the pseudoelastic region results in the plastic deformation of martensite until full fracture occurs.

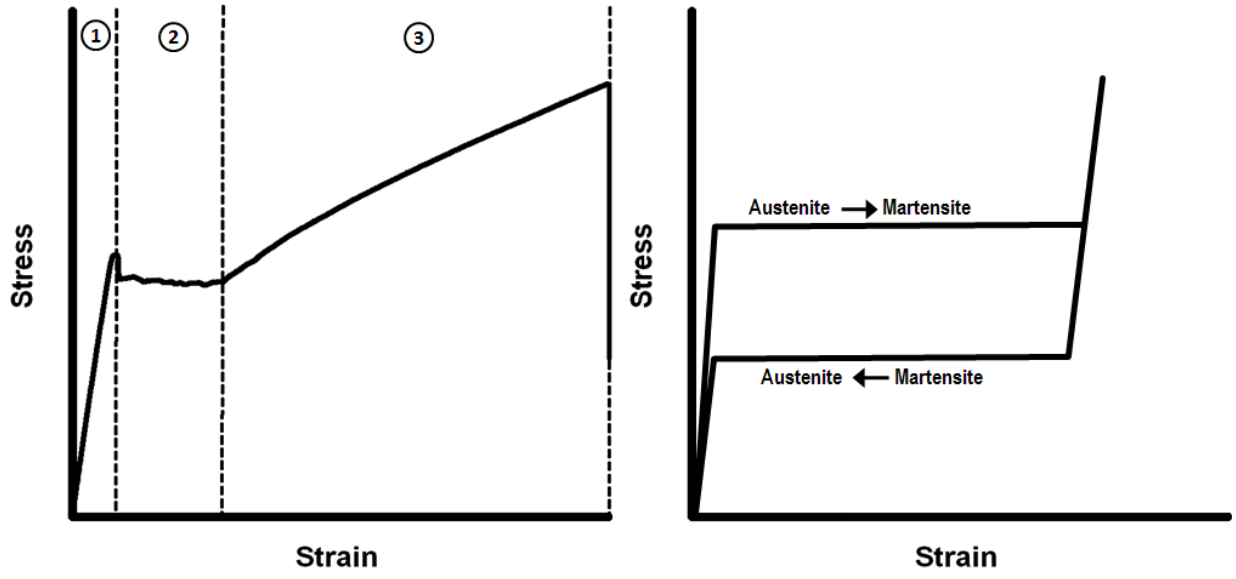

a) Stress-strain curve until fracture **b) Pseudoelastic Loading-unloading curve [19]**

Figure 2-6: Schematic of a typical stress-strain curve for pseudoelastic NiTi alloy

The stable phase at the working temperature dictates which functional property is active. This dependence of temperature is shown in Figure 2-7. Below M_f, the temperature at which the phase transformation to martensite is complete, the

predominant functional property is the shape memory effect. Pseudoelasticity is only observed at temperatures above A_f but below the martensite deformation temperature (M_d), the highest temperature at which martensite will form from austenite in response to applied stress [28]. Above Md, the critical stress exceeds the stress that would cause permanent yielding in austenite. At temperatures where the transformation is partially completed such as between M_s and M_f or A_s and A_f, the two phases will co-exist. Additionally, SIM generally occurs at higher stresses than detwinning of martensite because martensite in Nitinol is much softer than austenite.

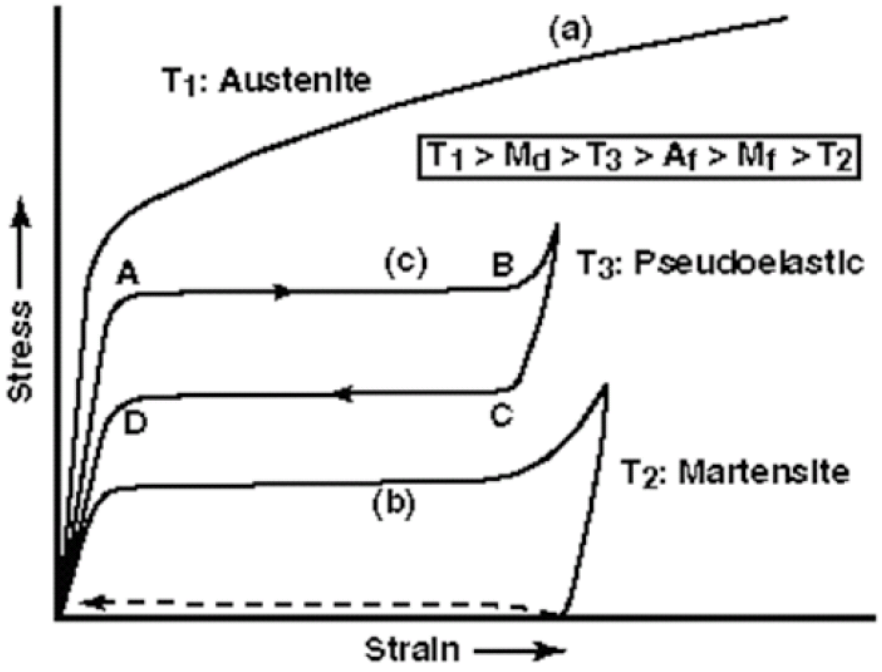

Figure 2-7: Hypothetical stress-strain curves of Nitinol conducted at different temperatures: (a) T1 is above M_d, (b) T_3 is above A_f but below M_d, and (c) T_2 is below M_f.

The effects of temperature on the shape memory effects of SMA are shown in Figure 2-8. This figure shows the stress at which the M_s and A_s transformations occur with varying temperature when a sample is put through a loading and unloading cycle. It can be shown that stresses required to attain M_s and A_s vary linearly with temperatures and at higher temperatures greater stresses are required for transformation. This linear correlation between temperature and transformation has been shown to obey the Clausius-Clapeyron relation [20].

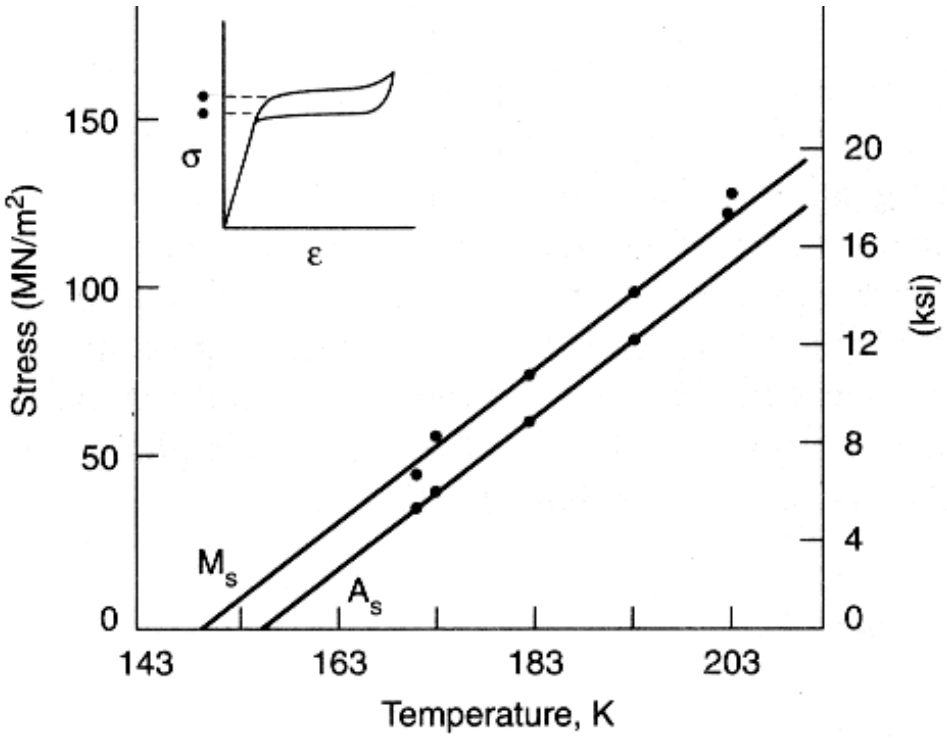

Figure 2-8: Temperature dependence of transformation stress [21]

2.1.4 Shape Memory Effect

Nitinol stress-strain curves at temperatures below M_s do not exhibit the pseudoelastic recovery observed at temperatures above M_s. However, heating a specimen enables the strain to be recovered and the specimen to regain its original shape. This effect is known as shape memory effect (SME) and is schematically detailed in Figure 2-9. During this cycle the initial parent material is brought to a temperature below M_s, where it can be easily deformed and maintain an altered shape. During deformation detwinning occurs to accommodate the large strains that can reach 13%. Subsequent heating to above A_f would result in phase transformation and recovery of the original shape.

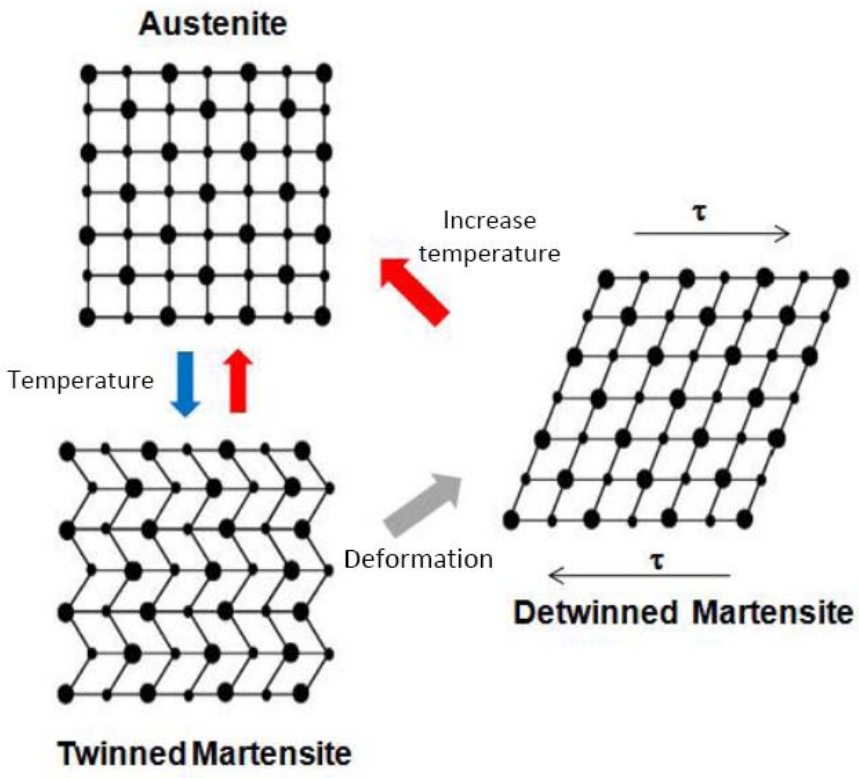

Figure 2-9: Phase transformation from austenite to martensite for SMA [22]

2.1.5 Ni-Ti Phase Diagram

The nickel-titanium phase diagram is shown in Figure 2-10. The Nitinol phase (NiTi) is restricted to the central region of the phase diagram between the Ti_2Ni and $TiNi_3$ phases, near the equiatomic composition. A detailed close-up view of the central region also reveals the presence of Ti_3Ni_4, which is a metstable intermediate phase. It has been reported that at lower aging temperatures the Ti_3Ni_4 phase appears while at higher aging temperatures the $TiNi_3$ phase is more stable [23]. However, Nishida et al. reported the Ti_2Ni_3 phase as an additional intermediate metastable phase [24]. Hence, it was shown that the diffusional transformations occurred in the following order with increasing aging temperature:

$$Ti_3Ni_4 \rightarrow Ti_2Ni_3 \rightarrow TiNi_3$$

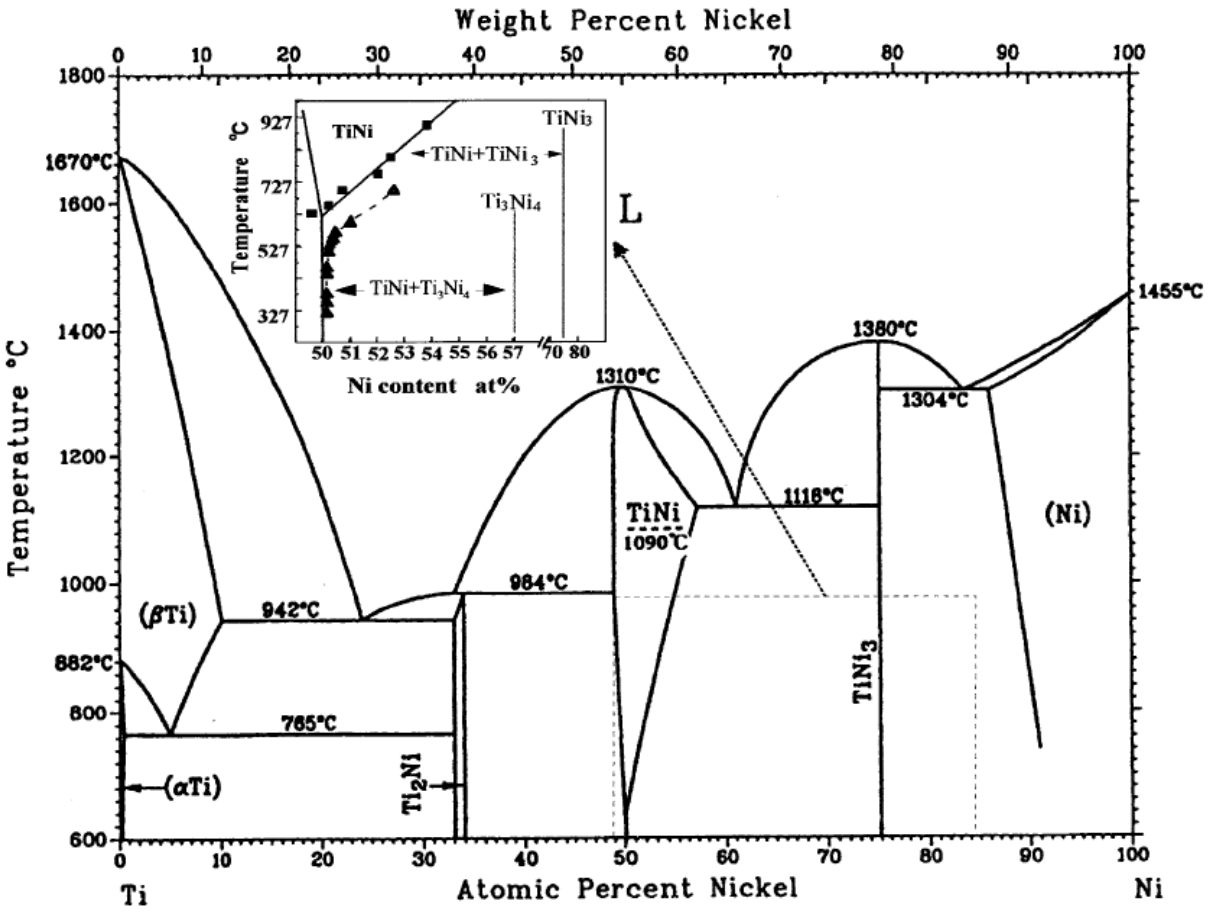

Figure 2-10: Ni-Ti phase diagram [25]

2.1.6 Fabrication and Processing of Nitinol alloys

Fabrication of Nitinol alloys has been continuously refined since its discovery in 1963. Virtually all Nitinol alloys undergo similar fabrication processes in order to produce a material in its final form (i.e. wire, ribbon, sheet and bar). The fabrication steps and sequence typically include [26]:

1) Ingot Melting
2) Hot Working
3) Cold Working
4) Heat treating

Since Nitinol alloys are highly sensitive to composition variations, melting typically occurs in an inert or vacuum atmosphere. Although several melting methods can achieve this, the two most common methods include vacuum induction melting (VIM) and vacuum arc melting (VAR). Both methods are also commonly used in combination to attain higher purity alloys. The resulting as-cast ingot subsequently undergoes hot working procedures in order to attain higher ductility and bring it to a more useful shape. Hot working is typically conducted between 600-800^{o}C using various techniques that can include forging, extruding and rolling.

Cold working is an effective way to modify the phase transformation behaviour of Nitinol, a technique often employed to achieve better mechanical properties. During this step a balance between mechanical and physical properties is achieved. It also destroys the shape memory effect and pseudoelasticity since random added dislocations impede the mobility of twin boundaries. Permanent deformation of the detwinned structure also reduced the latent heat of transformation and broadening the temperatures at which transformation occurs [27,28,29]. Permanent deformation of Nitinol is typically limited to between 30-50% before annealing is required due to excess work hardening. Common cold-drawing processes include wire drawing, tube drawing and sheet rolling to produce the final desired material form.

Cold-working is generally coupled with heat treatment to increase toughness as well as to “restore” the memory effect by removing some of the lattice strain. Typical treatment temperatures range between 450-800^{o}C. At high enough temperature and/or prolonged times, the precipitation of Ti_2Ni can be induced in the Ti-rich side, and Ti_3Ni_4, Ti_2Ni_3 and $TiNi_3$ in the Ni-rich side. Precipitation of IMCs can modify the chemistry, which has been shown to change the transformation temperatures [30]. Moreover, a 2 stage phase transformation between martensite, an intermediate phase referred to as R-phase, and austenite can be introduced after aging [33, 37]. A detailed description of R-phase and its development can be very complex and is beyond the scope of this thesis. Nonetheless, it can be seen from Figure 2-11 that the phase transformation behaviour of Nitinol can be altered significantly via different thermomechanical treatments.

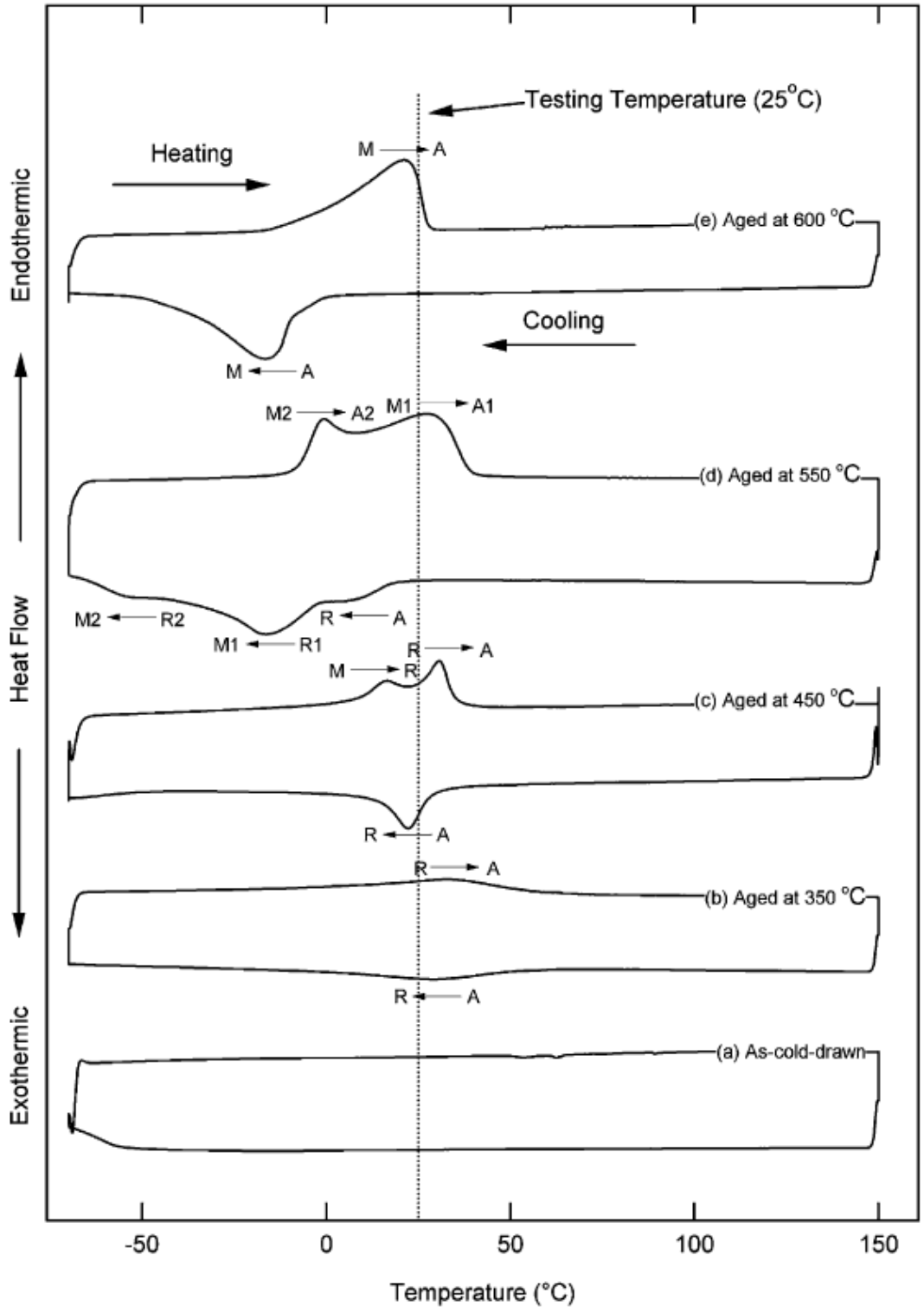

Figure 2-11: DSC curves of cold-drawn Nitinol after different heat treatments [34]

2.2 Laser Processing

Laser emission at optical wavelengths was first reported in 1960 and led to advances in communications, imaging and materials processing [31]. Lasers are defined as devices that generate high intensity light beams that are monochromatic with high spatial and temporal coherence [32]. The high level of coherency in laser light produces beams with very low diffraction that can be focused with simple optics to a small spot [33]. This can produce extremely high power densities. By manipulating the high power densities produced by lasers, various manufacturing processes have been realized. Today, they are commonly implemented for joining, cutting, drilling and heat treatment.

Different energy densities can be achieved by the manipulation of lasing hardware (fibre optic, output coupling optics) and process parameters (time, power, focal distance). Depending on the duration, a material may interact with the laser differently. Figure 2-12 shows the range of phenomena expected as a function of power density and pulse duration [34]. Optimization of welding parameters is important to attain desired effects while preventing undesired ones [34].

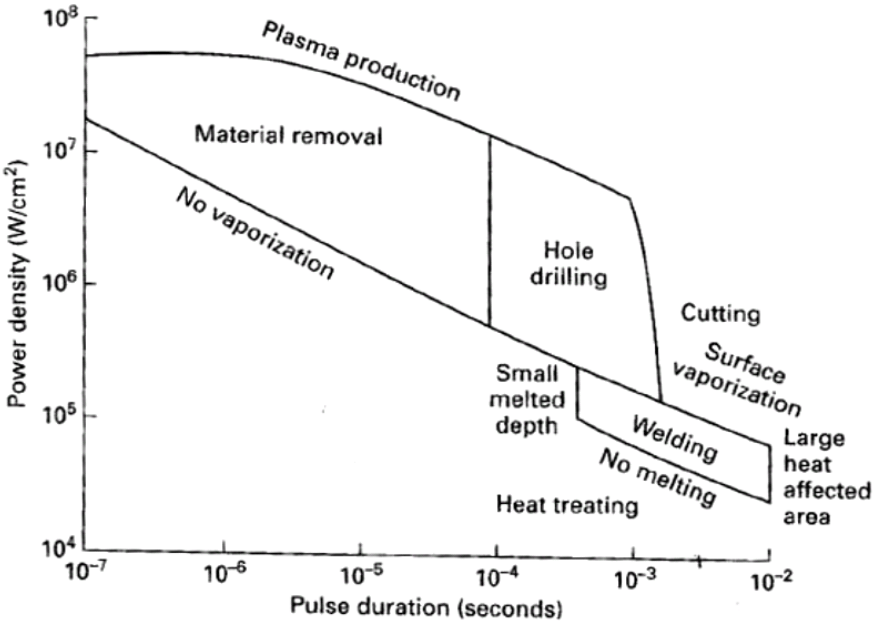

Figure 2-12: Laser-material interaction phenomena expected as a function of pulse duration and beam power density [34]

2.2.1 Laser Fundamentals

Laser describes the emission of radiation as light wave via a stimulated emission process. The emitted light is spatially and temporally coherent with very low diffraction, which can be coupled with transmittance optics to focus the high intensity beam to a single spot of high energy density [31,35]. Stimulated emission is the primary mechanism responsible for light amplification. It creates population inversion, a required state for laser operation that exists when the number of photons being amplified per unit time is greater than the number of photons being absorbed [35,36]. There are generally two scenarios in which photons can be emitted: spontaneous emission and stimulated emission. The former describes a 1:1 ratio of photon emission to electron relaxation. In stimulated emission, the incident photon collides with another energized atom causing an emission of another photon of equal frequency, phase polarization, and direction of travel.

During the operation of a laser, atoms are energized from the ground state to the excited state by pumping. Incoherent photons are emitted when the atoms relax back to the ground state. Photons that do not travel parallel to the optical axis of the laser are quickly lost in the resonator while photons that travel parallel to the optical axis are oscillated in the resonator with the possibility of inducing stimulated emission, which in turn can create additional coherent photons [35]. Further populating the monochromatic and unidirectional photons produces the highly energetic laser beam suitable for welding.

The occurrence of a population inversion is required to amplify the amount of light. When a population inversion is present in the laser cavity the laser can interact with excited atoms and lower the energy level, while releasing additional quanta of light [37]. Otherwise, without a population inversion, the energy from the laser will be absorbed to energize electrons and hence reduce the laser beam energy. After being amplified, the beam is released through the partially reflective mirror in the cavity.

A laser system consists of three main components: (1) amplifying medium, (2) means of exciting the medium to its amplifying state or pump source and (3) an optical resonator

[35]. The active medium is comprised of materials that produce energy-carrying photons of specific wavelengths when excited. The pump source is determined by the type of active medium used. Examples of pump sources include flash lamps and electrical discharges for Nd:YAG and CO_2 media, respectively [35]. The optical resonator, in the simplest form, is composed of two parallel mirrors, one fully and one partially reflective, placed around the active medium to filter and transmit photons that fully satisfy specific conditions for oscillation [35].

A schematic of how a laser cavity produces a laser beam is shown in Figure 2-13. Laser light is produced when a valence electron drops from a higher energy electron state to lower energy electron state within an atom. However, before this can occur the electrons in the lasing medium must be stimulated from an external energy source. Electrons can be energized either by directing a stream of electrons or by flashing high intensity light at the medium. When energized, the electrons move to higher energy shell within the atom and during decay release energy in the form of light and the energy difference associated with the decay determines the wavelength of the light. The spontaneously released quanta are reflected within the laser cavity to collide with other energized atoms to induce the release of more light, hence amplifying the amount of light.

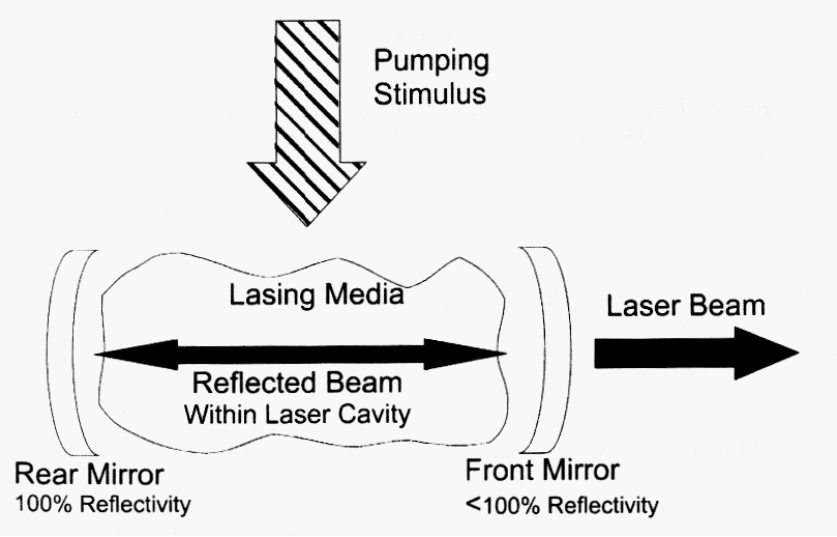

Figure 2-13: A schematic of how a laser cavity produces a laser beam [38]

The wavelength of light produced by a laser depends on the materials used to make the semiconductor and can vary from 0.1 to 10 μm. Common lasers include CO_2, Nd:YAG and diode lasers. Figure 2-14 shows the absorptivity of some materials as a function of wavelength [33]. Nd: YAG lasers have the shortest wavelength of the aforementioned lasers and their emission can more efficiently be absorbed by most materials. This indicates that materials welded using Nd:YAG absorb energy more efficiently to melt a specific volume of material when compared to most other lasers. Also, Nd:YAG laser beams can effectively be transmitted through glass, enabling increased flexibility for the use of fiber optics to control beam transfer.

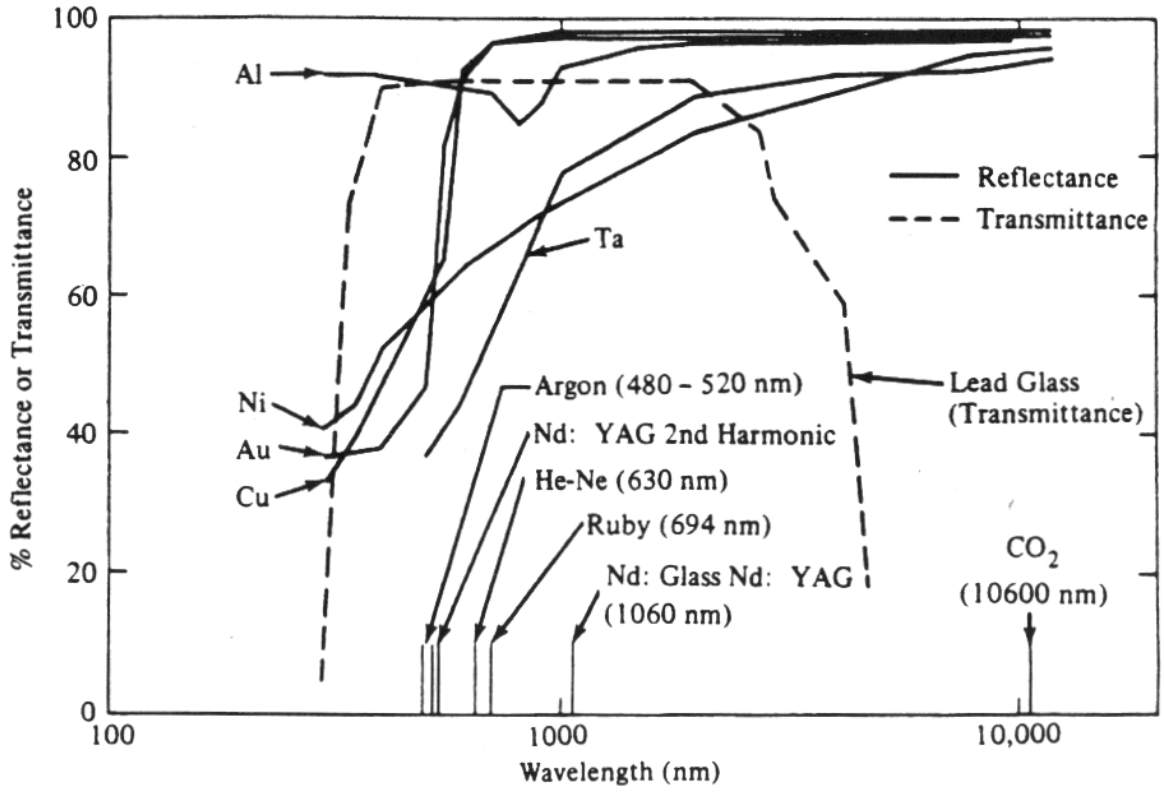

Figure 2-14: Material absorptivity as a function of wavelength [37]

2.2.2 Pulsed Nd:YAG Laser Processing

Their stable power output and high power density have made pulsed Nd:YAG lasers ideal for industrial applications. A schematic diagram of the layout of a Nd:YAG laser system is shown in Figure 2-15. The cavity assembly is composed of an active medium, pumping source and resonator. When a yttrium aluminum garnet (YAG) crystal doped with neodymium (Nd) atoms is excited, it produces photons with a wavelength of 1064 nm [35]. Excitation radiation is pumped using flash lamps. The laser output is transmitted through the input coupling optic and into an optical fiber that connects to the working head before being delivered on the workpiece. Nd:YAG lasers offer several advantages over other laser systems. The ability to deliver photons via a fiber is advantageous for fabrication of complex components. Other advantages include higher processing efficiency, ability to create narrow welds with small heat affected zones (HAZ) and welding of special materials (i.e. titanium and quartz) [31**Error! Bookmark not defined.**,35].

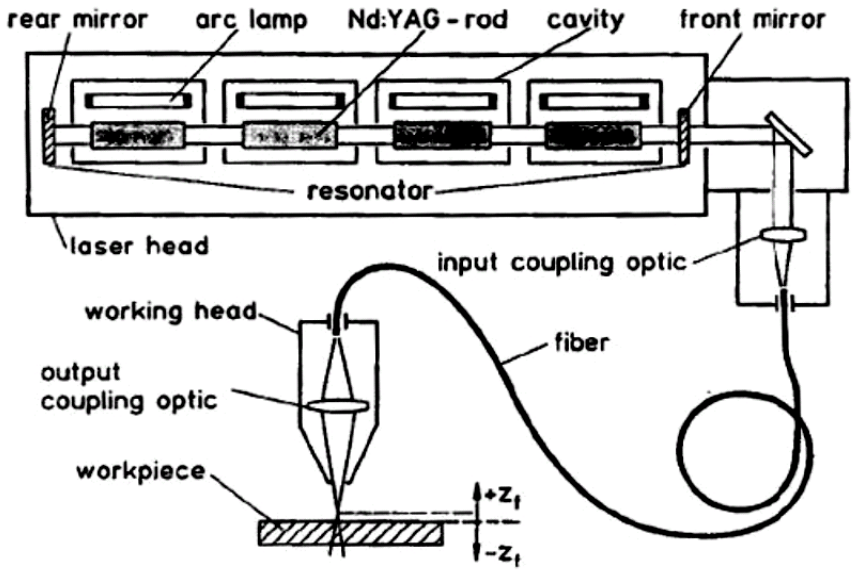

Figure 2-15: Schematic of Nd:YAG laser setup

2.2.3 Pulsed Nd:YAG Laser Processing Parameters

Several key parameters are used to control the pulsed Nd:YAG laser process. These parameters include pulse width, peak power, frequency, travel speed and defocus

distance. Individual pulses can be defined by peak power and pulse width, whereas multiple pulses are often applied, with each pulse successively overlapping the previous one. A schematic showing pulse interaction is shown in Figure 2-16. The amount of overlap between individual pulses is controlled by frequency and weld travel speed for a given spot diameter. Equation 1 correlates the various welding parameters including frequency (f), spot diameter (d_s), processing speed (V) and percent overlap (%OL).

$$f = (100V)/d_s*(100-\%OL) \qquad [1]$$

From the above equation it can be shown that the pulse frequency and speed are directly related (i.e. higher pulse frequency correlates with higher speed). Pulse frequency and processing speed are typically controlled to attain the desired spot overlap Minimum criteria typically include full penetration and hermetic seal conditions. Spot overlap is typically varied from 50% for strength applications and 75%-80% for hermetical sealing applications [39,40].

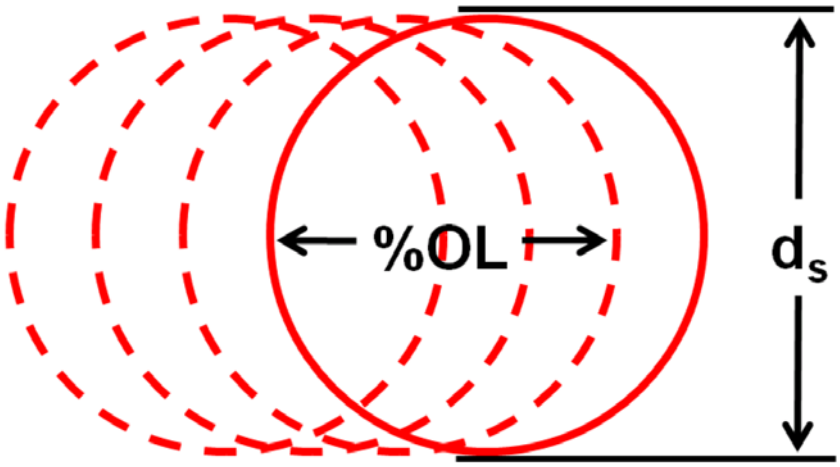

Figure 2-16: Schematic of laser pulse interaction during pulsed Nd:YAG laser welding

Average peak power and pulse energy are for process feedback to conceptualize the amount of energy that is applied, which may be deceptive in terms of the actual processing schedule. Figure 2-17 is a schematic of a temporal profile of laser pulses produced with the Nd:YAG laser process. Pulse energy and average power are compound units which are typically used to characterize power transferred to the workpiece. The pulse energy is the amount of energy transferred during each pulse and

is a function of pulse width and peak power. The average power is the amount of overall power being transferred towards the workpiece and is a function of pulse energy and frequency. However, it should also be mentioned that all of the output power is not absorbed by the work piece. This is due to substantial energy losses associated with factors, such as reflection, making it difficult to precisely determine the energy absorption by the workpiece.

The operator sets the peak power, pulse width and frequency on the laser processing machine. The peak power is the instantaneous power of the laser pulse and can influence the temperature rise of the material. Melting is initialized when there is sufficient heat to raise peak temperatures above the liquidus temperature of the workpiece. This involves overcoming heat loss due to conduction and convection. The pulse width is the time each pulse irradiates the workpiece. The larger the pulse width the longer the time the peak power is applied. Finally, the pulse frequency is the number of times the laser is pulsed per second, which can be used to control the amount of pulse overlap and heat input to the workpiece.

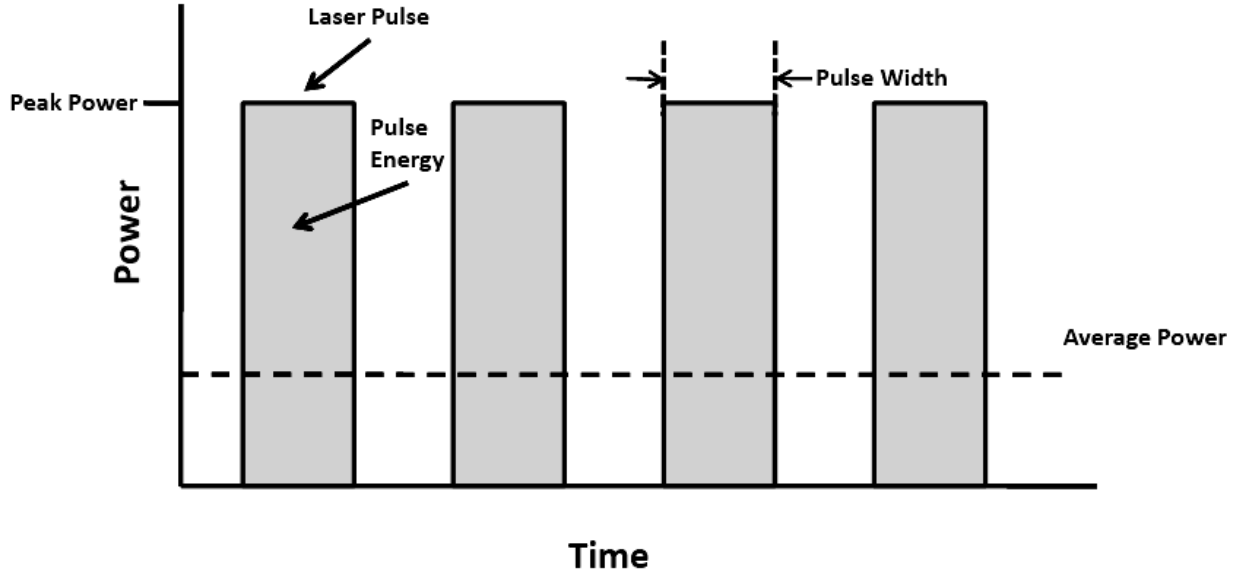

Figure 2-17: Schematic of pulsed Nd:YAG output

The advantage of laser processing is the ability to attain high energy densities and hence producing maximum penetration in the workpiece. This is achieved when the light

is focused to a minimum waist diameter or focus spot size at the zero defocus distance, as shown in Figure 2-18 [35]. Offsetting from this distance will defocus the light resulting in a decrease in power density. Focus spot size is determined by the interplay between optics, laser characteristics and parameters. A laser in its convergence range has the highest energy efficiency, whereas the focus position relative to the workpiece is dependent on mode (conduction or key-hole) and geometry [35]. The general rule is to focus at a distance where maximum penetration depth is empirically attained through experimental verification.

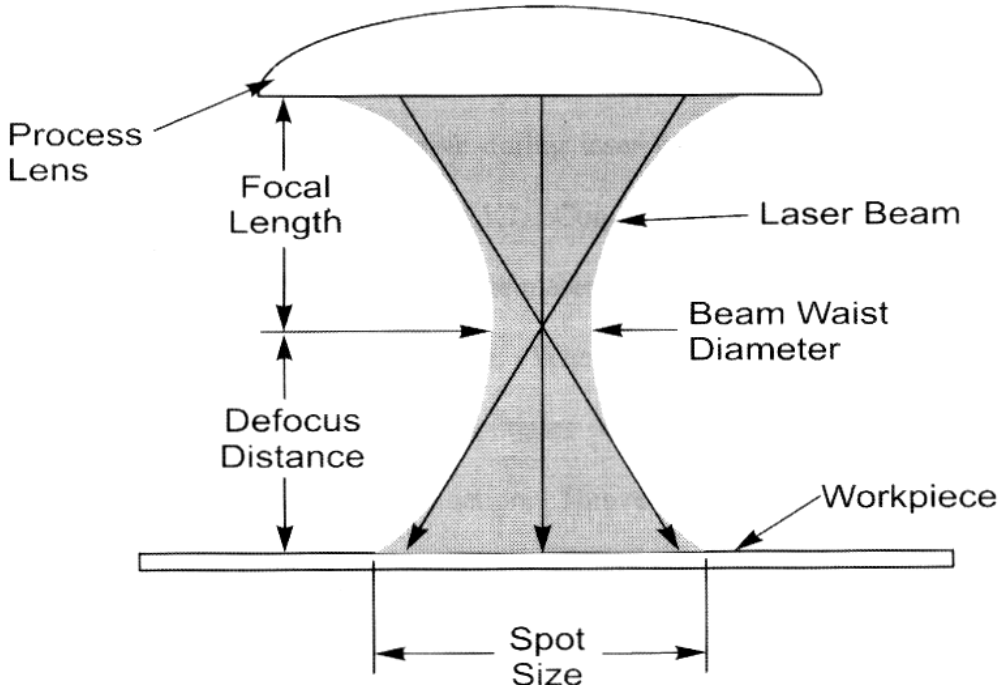

Figure 2-18: Schematic of propagation and convergence of laser beam [38]

2.2.4 Laser Processing Modes

Figure 2-19 illustrates the conduction and keyhole processing modes that occur during laser welding. In conduction mode the laser intensity is only sufficient to melt the workpiece. The pool initiates at the surface and grows due to conduction in all directions, resulting in a semi-elliptical shape. Since the laser energy is only absorbed by the top surface of the material, material reflectivity can substantially reduce the

amount of heat transfer. In contrast, keyhole occurs when peak temperatures at the surface are sufficient to vaporize the workpiece material. The keyhole depression in the molten pool is created from the pressure of vaporization. This results in a narrow weld with deep penetration. Compared to conduction mode, keyhole mode more efficiently transfers heat to the workpiece. The keyhole traps the laser energy and the internal reflection within the keyhole can act as a blackbody.

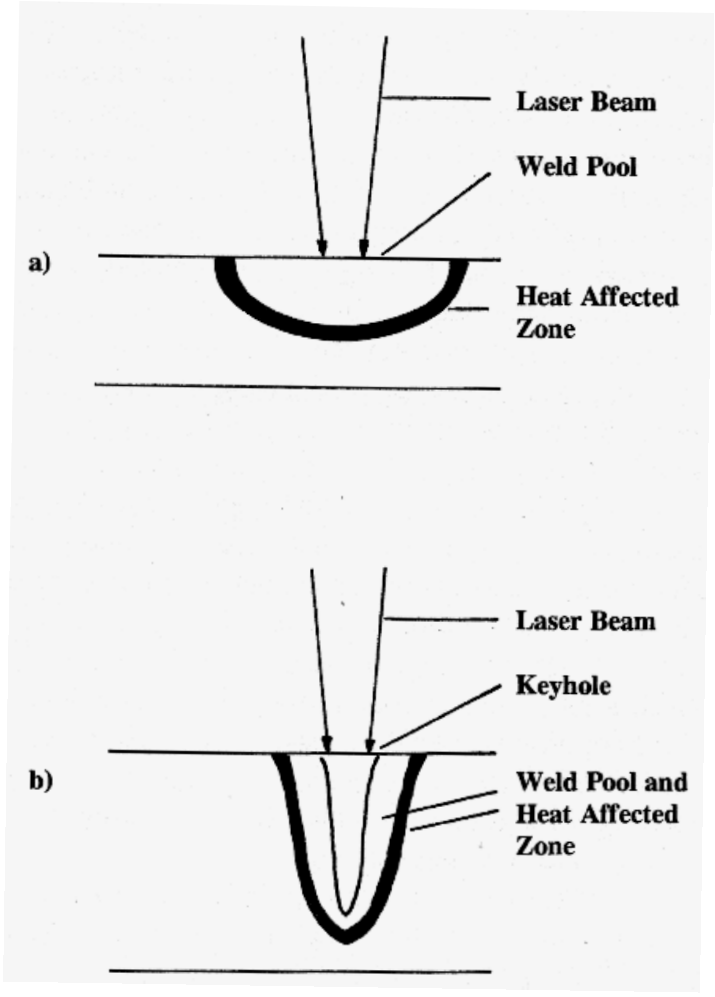

Figure 2-19: Comparison of (a) conduction and (b) keyhole welding modes [31]

2.2.5 Shielding Gas

Since most materials can be readily oxidized, shielding gas of argon or helium is generally used to prevent reaction of atmospheric oxygen or nitrogen with the molten

pool during welding. Atmospheric enclosures are typically implemented in order to attain reliable shielding. Oxide inclusions in the processed metal microstructure are often detrimental to material properties [**Error! Bookmark not defined.**,35]. Proper selection of shielding gas has also been shown to enhance the transmission of the incident laser beam for absorption by the workpiece [41].

2.3 Laser Processing of Nitinol

To date, only limited literature has been reported on the effects of laser processing on the mechincal properties of Nitinol sheet. Despite a lack of systematic analysis, fundamental understanding and often inconsistent and conflicting results in the literature, the following sections attempt to chronologically summarize the current "state of the art" in joining of Nitinol to provide a rationale or starting point for the current proposed work. It should be noted that most studies have been intended to investigate the effects of laser welding on the mechanical properties of Nitinol and use 'bead on plate' procedures in which a monolithic sheet is processed using a laser.

The following sections are subdivided to describe the effects of laser processing on the mechanical performance and phase transformation of Nitinol alloys (Ni and Ti rich). Furthermore, other processing methods similar to laser processing were also reviewed in order to gain a comprehensive understanding of the effects of processing.

2.3.1 Mechanical Performance

Earlier studies done in 1994 and 1997 by Schloßmacher et al. focused on laser processing of Ni- rich and Ti-rich Nitinol [42,43]. Figure 2-20 shows the stress-strain curves for base and welded metal at varying temperatures conducted on Ti-rich alloys. Compared to the base metal, substantial reductions in tensile strength and elongations were observed. This was suggested to be due to the changes in weld microstructure, e.g., the formation of other more brittle intermetallic compounds (IMC), such as Ti_2Ni, or increased grain size. In contrast, the Ni-rich alloys retained pseudo-elastic properties and formed Ni_3Ti IMC within the weld.

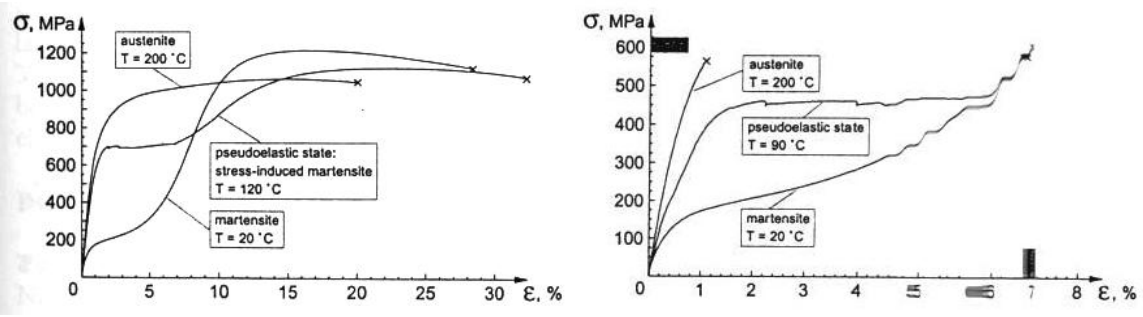

(a) (b)

Figure 2-20: Stress strain curves for (a)Ti-rich base metal and (b) welded Nitinol [42]

In 1997, a study on micro-machining and joining of Ni-rich Nitinol using Nd:YAG lasers was conducted by Schüßler [44]. Two different tensile coupon designs were tested, including a locally processed region (referred to as laser welded) and another fully 're-molten' sample, shown in Figure 2-21a. As observed in Figure 2-21b, each sample produced a distinctly different curve with the re-molten sample showing a clear drop in pseudoelastic stress. The author attributed this lower plateau stress to recovery experienced during the remelting procedures. This study also emphasized the difference that tensile test geometry has on test results. Furthermore, the same study also analyzed the effect of high cycle fatigue at low strain on Ni-rich Nitinol and reported nominal change as compared to the base material.

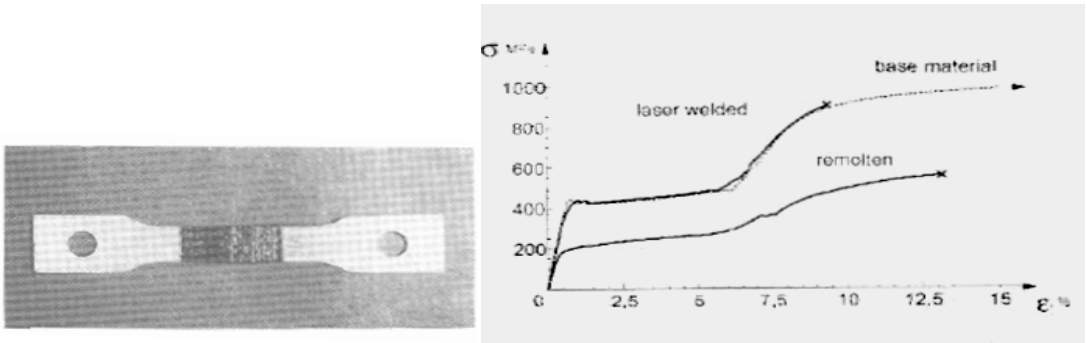

(a) **(b)**

Figure 2-21: Geometry of re-molten tensile coupon (a) and associated stress-strain curve (b)

Similarly, in 1999 Tuissi et al. investigated the effect of laser welding on the functional properties of Ni-rich Nitinol and reported a slight decrease in pseudoelastic properties

[45]. The studies of Tuissi et al. and Schüßler et al. [44] are contrary to the work presented by Schloßmacher et al. [45] which reported limited change in pseudoelastic properties.

In 2001, Hsu et al. isolated and tested the laser welded material for equiatomic Nitinol [46]. It was shown that the equiatomic weld metal exhibited higher strength when compared to the base metal, although it did not exhibit pseudolelastic properties at room temperature. Interestingly, in this publication the stress-strain results for the Ni-rich alloys were not reported or discussed. However, the cyclic loading results for the laser welded Ni-rich Nitinol were shown. As shown in Figure 2-22 an increased permanent residual strain and efficiency of energy storage (η) was observed for the laser welded metal as compared to the base metal.

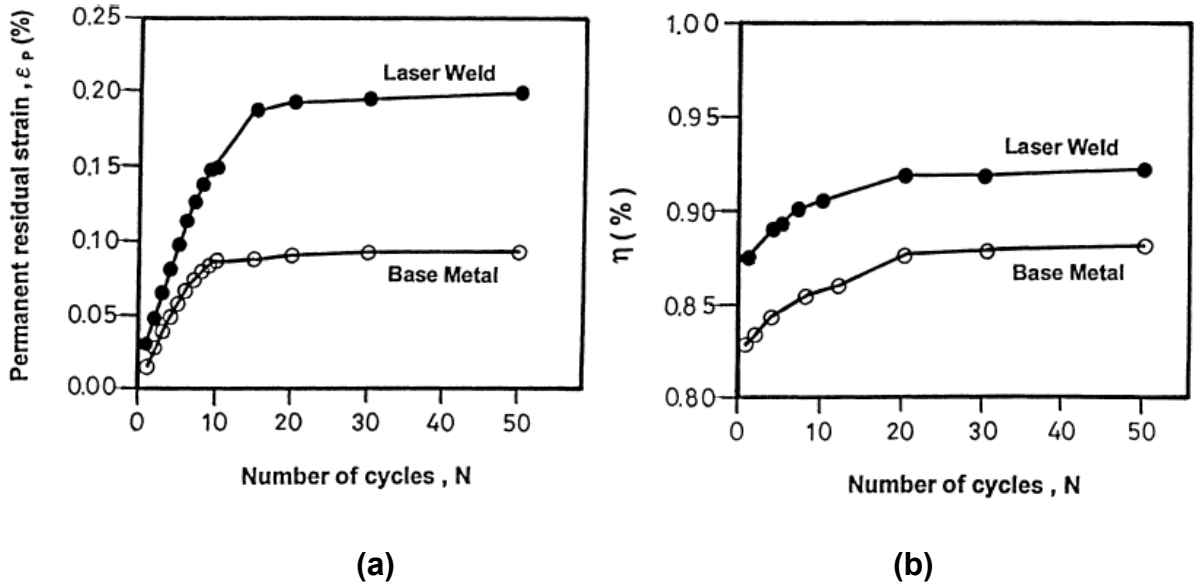

(a) **(b)**

Figure 2-22: Effects of cyclic loading on (a) permanent residual strain and (b) efficiency of energy storage for welded and un-welded Nitinol [46]

The work by Hall [51] on Ni-51.5Ti (Ti-rich) and Ni- 49.5Ti (Ni-rich) wires is probably the only one that investigating cracking during welding. This provided some valuable insight into the cause of reduced mechanical performance consistently observed in Ti-rich alloys. The onset of solidification cracking in the re-molten region is very sensitive to Nd:YAG laser lap welding of the Ti-rich alloy was, shown in Figure 2-23, which resulted

in very low weld strength. On the other hand, the Ni-rich alloy showed no cracking in laser welds. However, no detailed analysis was provided on cracking mechanisms, e.g., whether the cracking was caused by impurities (such as S and P) or other elements that could lead to low-melting-point phases (e.g., eutectic reaction at 942°C at the Ti-rich side of the Ni-Ti phase diagram). Moreover, little research (e.g., using transmission electron microscope, TEM) confirms the types of IMCs and/or precipitation sequences in welds. Many questions need to be answered, e.g., whether metastable phases exist in the processed metal as observed during the aging of Nitinol alloys [47].

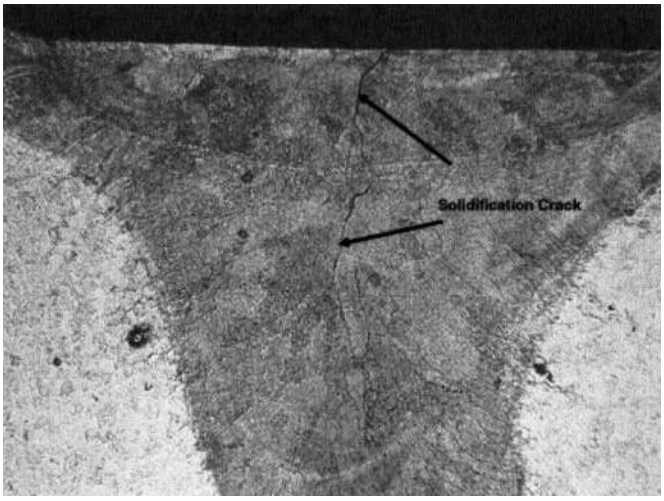

Figure 2-23: Cross-section of laser welded Ti-rich Nitinol [51]

In 2004 Ogata et al. [57] reported a 30% decrease in tensile strength with brittle fractures and loss of pseudoelasticity in Nd:YAG laser welds of Ni-49.09Ti wire even though no IMC was observed. This was believed to be caused by the increased grain size to 1-3 μm in the re-molten metal and 3-10 μm in the heat affected region, compared to about 0.1 μm in the base metal. The detrimental influence on pseudoelasticity could be minimized by reducing the re-molten area and by limiting grain growth in the heat affected region. The latter was done by welding Nitinol wires in the cold-rolled state and performing shape memory treatment after welding, which resulted in a grain size of about 1 μm due to recrystallization.

All of the aforementioned publications reported a reduction in strength for laser processed Nitinol alloys with reductions being more prominent in Ti-rich alloys. More

recently, Falvo et al. stated that large strain applications of Ti-rich Nitinol should be avoided and stated a need to further investigate the effects of process parameters [48]. A technical appraisal of shape memory alloys conducted by Chau et al. reiterated that much more research needs to be undertaken before practical applications can commence [49].

2.3.2 Phase Transformation

As detailed in section 2.1, functional properties of Nitinol are largely linked to its ability to reversibly transform from low temperature martensite to high temperature austenite. However, existing publications on laser processing have reported only preliminary results on its effect on mechanical performance. Detailed analysis of structural and phase changes is still lacking, but required in order to better understand the influence of laser processing on mechanical performance. In particular, the tensile properties of the low temperature martensite phase are substantially different from the high temperature austenite phase, which typically exhibits reversible stress induced transformation (pseudoelasticity). However, publications have thus far shown minimal effect of laser processing on these discrete transformation temperatures, including studies by Schloßmacher et al. [43], Tuissi et al. [45], and Flavo et al. [48]. These all reported only minor increases in transformation temperature whereas Hsu et al. [50] noticed a slight decrease (Figure 2-24,). None of the aforementioned changes in transformation temperature were found to be severe enough to alter the room temperature mechanical performance.

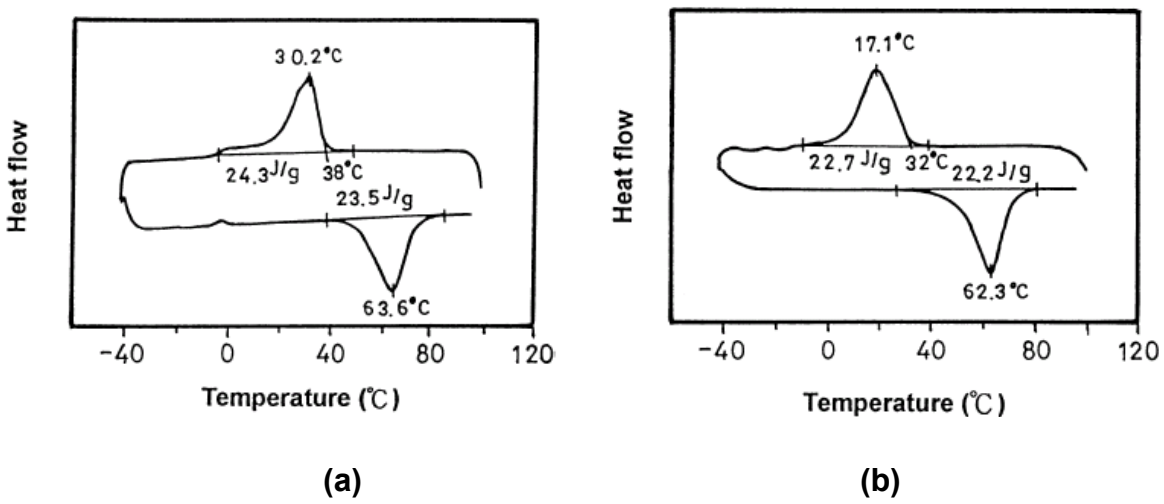

Figure 2-24: DSC results for equiatomic Nitinol (a) base metal and (b) laser welded [46]

2.3.3 Effects of Other Processing Methods

Almost all the publications have reported lower strength or altered pseudoelasticity to some extent due to laser processing. Many of the physical phenomena experienced during laser processing (i.e. heating, melting, and solidification) occur in other processes (i.e. resistance heating/welding and arc melting/welding); thus, some insight can be gained by reviewing this related research on Nitinol [51,52,53,54,55,56,57].

For example, similar to laser processing of Ti-rich alloys, the formation of Ti_2Ni (Figure 2-25) during arc percussive welds of Ni-51.5Ti resulted in very low welding strength [51]. IMC formation is obviously sensitive to the Ti/Ni ratio and welding conditions since arc percussive welds of Ni-49.5Ti showed no IMC and were 30% stronger than the Ni-51.5Ti welds. Similarly, while Ti_2Ni was observed in resistance welds of Ni- 51.5Ti, an increase in Ni content using Ni foil inserts resulted in a change of the IMC from Ti_2Ni to $TiNi_3$, which was also very brittle and cracked due to the shrinkage stresses during welding [51].

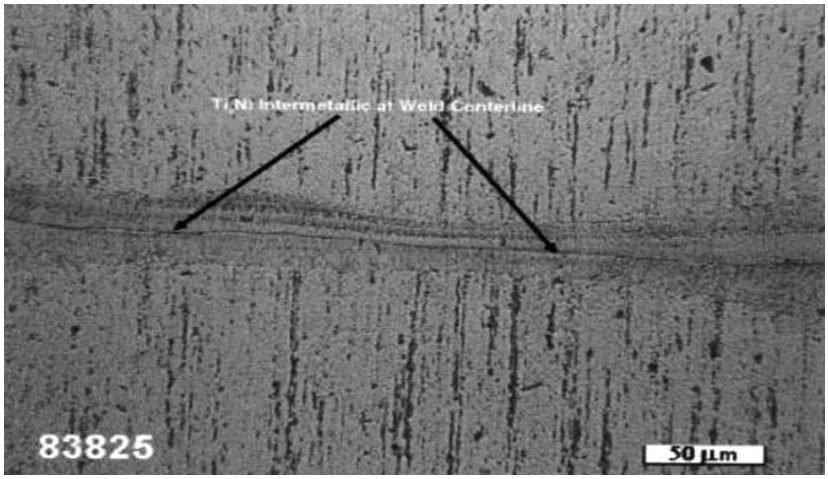

Figure 2-25: Ti_2Ni intermetallics in Ti-rich arc-percussive weld [51]

Solidification cracking was also shown to be suppressed in pressure welding processes (such as resistance and arc percussive welding) because the forging force could counteract the natural shrinkage stresses in the weld [51]. However, cracking was relocated to the heat affected zone (HAZ) in resistance welding trials, as shown in Figure 2-26a, which was attributed to HAZ overheating that produced recovery stress and possible grain boundary liquidation. The use of Ni foil inserts, to increase contact resistance and hence reduce HAZ heating and recovery stress, eliminated the HAZ cracking (Figure 2-26b) and resulted in a 37% increase in weld strength. But this improvement left the strength only 50% of the base metal strength, presumably due to the formation of brittle $TiNi_3$ formed because of the Ni foil addition.

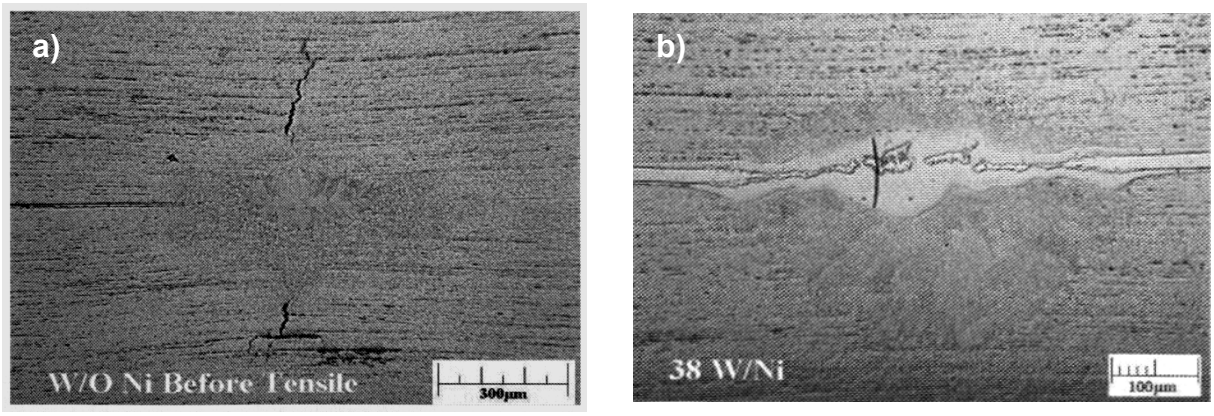

Figure 2-26: Resistance weld on Ti rich Nitinol (a) without and (b) with Ni foil [51]

It has also been suggested that post-weld heat treatment (PWHT) is needed to restore pseudoelasticity of friction processed Ni-43.99Ti. Mechanical deformation and thermal cycling was shown to lower the transformation temperatures significantly by about 60K [52]. It was reported that grain size refinement in friction stir welding could improve strength and retain pseudoelasticity [53], but this process is not suitable for small- and micro-sized medical devices because the current form of friction stir welding lacks the required precision.

3. EXPERIMENTAL METHODS AND CONDITIONS

3.1 Material

Commercially available SE508 Nitinol strip that were 0.37 mm thick were used in this study. The composition of this particular alloy is 55.8 wt. % Ni and 44.2 wt. % Ti with maximum oxygen and carbon contents of 0.05 wt. % and 0.02 wt. %, respectively. The as-received cold-rolled material was heat treated for 1 hour at 800^{o}C to attain pseudoelastic properties. Argon gas was continuously passed over the the sample during annealing procedures so as to limit oxidation of test strips. A dilute solution of hydrofluoric and nitric acid was subsequently used to remove the black oxide before laser processing commenced. The DSC curve detailing transformation temperatures for the base material is shown in Figure 3-1. Both austenite finish (A_f) and martensite start (M_s) temperaturs were below room temperature at -8.6 ^{o}C and -33.2 ^{o}C respectively. Therefore pseudoelastic behavior should be exhibited during tensile testing at room temperature.

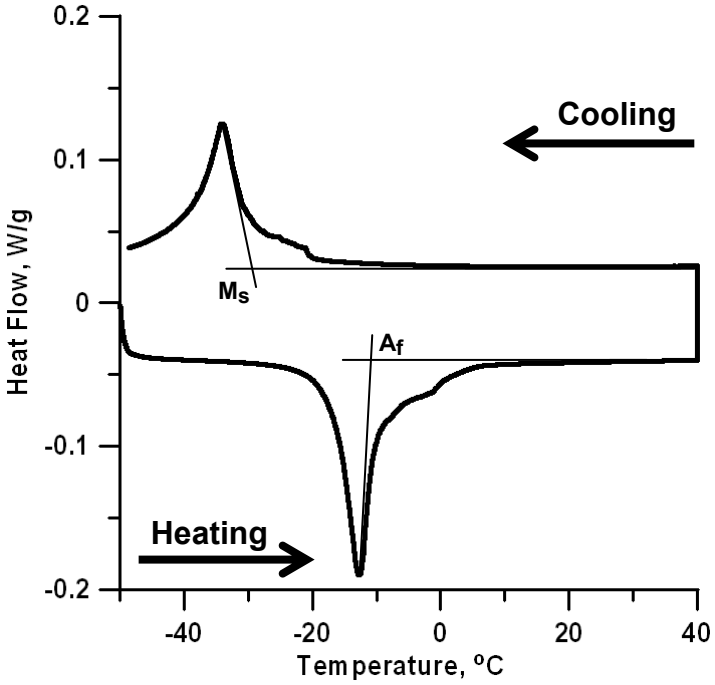

Figure 3-1: DSC curve for base-metal NiTi alloy

3.2 Laser Equipment and Process Parameters

Samples were produced using a Myachi Unitek pulsed Nd:YAG (neodymium-doped yttrium garnet) laser welder (Model LW50 A) shown in Figure 3-2 which produces a beam with a 1.06 μm wavelength. This particular system is intended for laser welding applications, although it is capable of other applications such as cutting and annealing. It is also equipped with a power monitor allowing for accurate *in situ* assessment of power output to ensure consistency. Laser processing was conducted on monolithic sheets. Top and bottom shielding of argon was implemented to minimize oxidation; a flow rate of 30 CFH was selected on the bases of a previous study on titanium alloys [58].

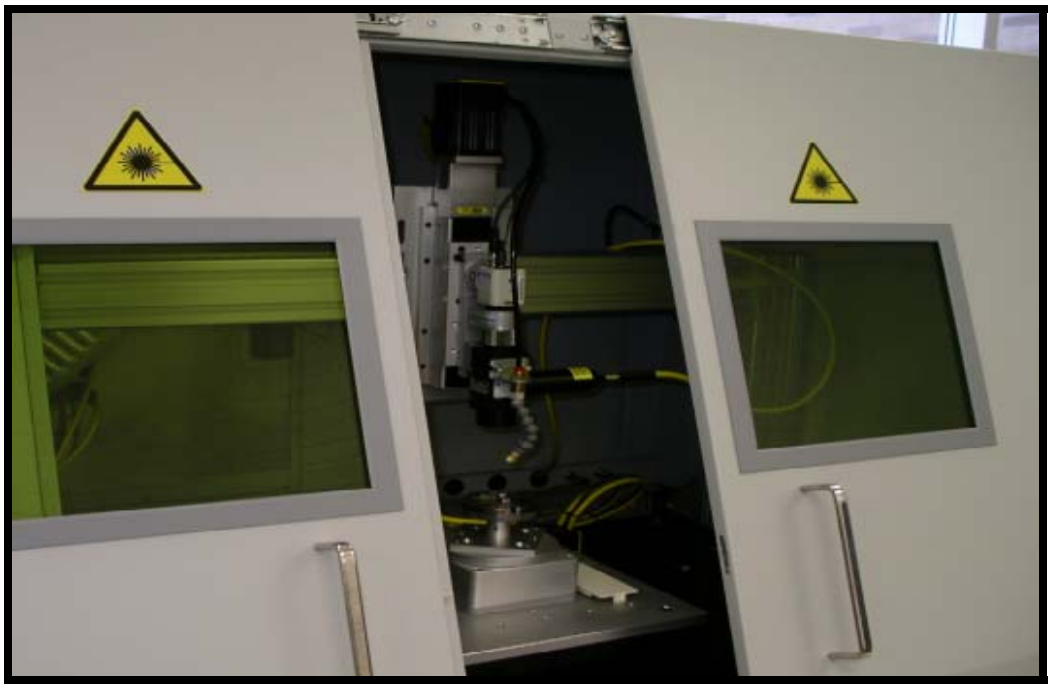

Figure 3-2: Myachi Unitek Nd:YAG laser system

Samples were produced using a 400μm spot diameter and 3 ms pulse time. Minimum criteria included full penetration (i.e. through the sheet thickness) and overlapping that mimicked hermetic seal conditions. It was determined that 0.6kW peak pulse power was sufficient for producing full penetration welds. References have shown that 80%

overlap of melted spots is used to produce hermetic welds [59]. Table 1 shows the selected process parameters, variable process parameters included pulse frequency and peak power. Parameters were selected using Equation 2, which correlates the frequency (f), spot diameter (d_s), welding speed (V) and percent overlap (%OL).

$$f = 100V/(d_s)(100-\%OL) \quad [2]$$

From the above equation it is evident that the pulse frequency and speed are directly related (i.e. higher pulse frequency leads to higher speed). Hence the terminology speed (V) will be referred to as pulse frequency (f).

Table 1: Selected processing parameters to maintain 80% overlap

condition (peak power, frequency)	***Speed***
0.6 kW, 10 pps	48.0 mm/min
0.7 kW, 10 pps	48.0 mm/min
0.8 kW, 10 pps	48.0 mm/min
0.9 kW, 10 pps	48.0 mm/min
0.6 kW, 1 pps	4.80 mm/min
0.6 kW, 5 pps	24.0 mm/min
0.6 kW, 15 pps	72.0 mm/min

Preliminary measurements of sample cross-sections were conducted for all conditions to ensure full penetration and characterize minimum width. Figure 3-3 shows the effect of pulse frequency and peak power on the minimum width for the selected processing parameters. Minimum width is depicted in the schematic shown in Figure 3-3a. Nominal change to the width was observed with increasing pulse frequency while maintaining

peak power (Figure 3-3b). However, on the other hand the minimum weld width increased from 260 μm to 460 μm with power increasing from 0.6kW to 0.9 kW.

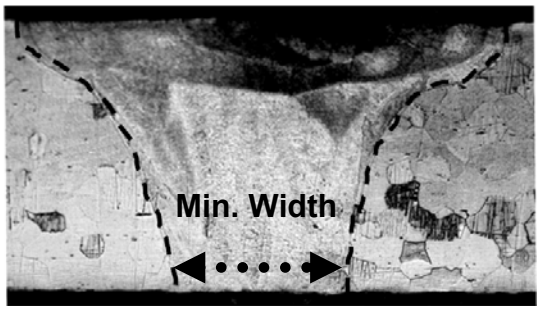

a) Cross-section showing minimum width

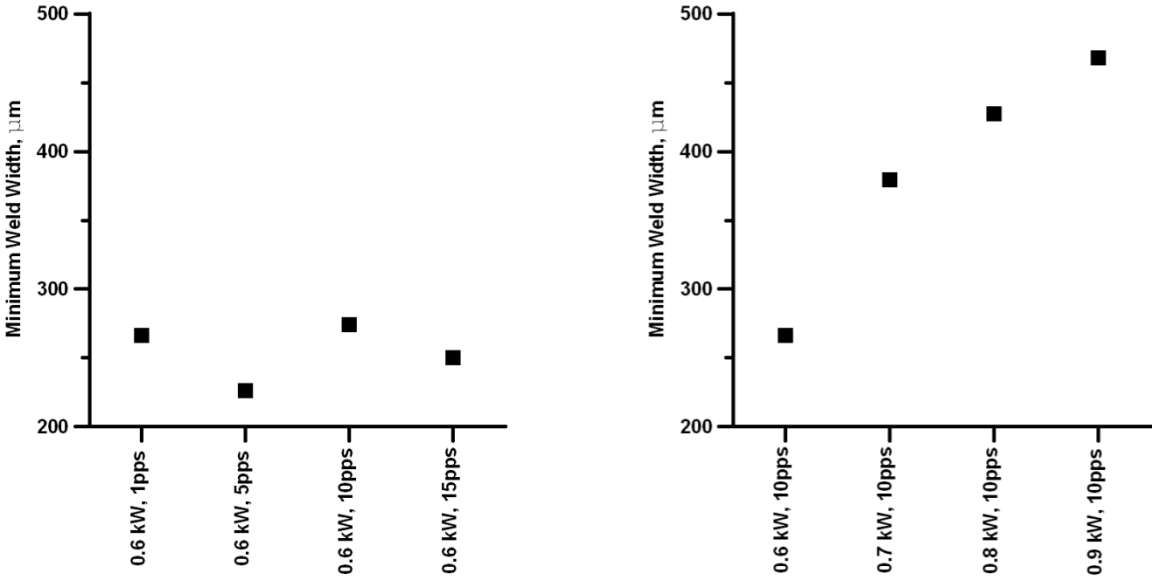

b) Increasing speed

c) Increasing Power

Figure 3-3: Effect of process parameters on minimum width

3.3 Mechanical Testing

3.3.1 Tensile Testing

Tensile specimens were prepared using wire Electrical Discharge Machining (EDM) cutting in order to minimize effects of burrs during mechanical deformation. A transverse weld configuration was selected to investigate the effects of both weld and base metal. Figure 3-4 shows a schematic of the tensile specimen with dimensions; the sub-sized samples were selected to maximize weld area along the gauge length. Tests were

performed using an Instron model 5548 micro tensile machine with a load cell resolution of ± 3 N. All tests were performed at room temperature (25^{o}C). A minimum of 5 tensile samples were tested for each condition. However to avoid visual saturation of data and maintain simplicity, representative tensile curves were selected for comparison of stress strain curves.

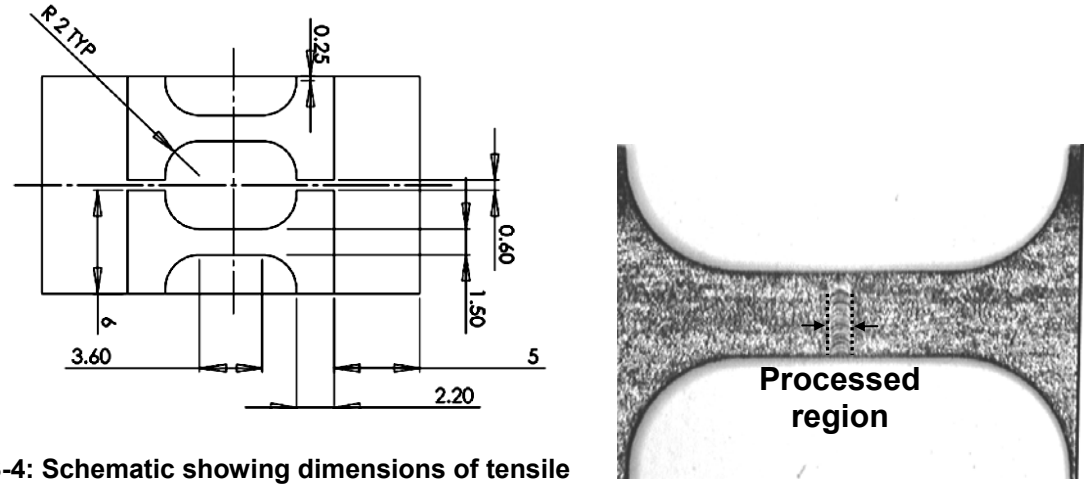

Figure 3-4: Schematic showing dimensions of tensile coupons in mm

3.3.2 Cyclic Loading

Cyclic loading tests followed conditions defined by Lin and Wu [60]. Tests were conducted using a cross head speed of 0.04 mm/min to apply a first loading cycle up to a strain of 0.06 mm/mm followed by an unloading cycle down to a stress of 7 MPa. The same cycle was repeated 50 times (50 cycles) for both parent and laser welded specimens. After completion of 50 cycles the specimens were strained at a cross head speed of 0.4 mm/min until fracture.

A schematic of the stress strain curve of a loading-unloading cycle for a typical NiTi exhibiting pseudoelastic behaviour is shown in Figure 3-5. It is well known that the pseudoelastic characteristic of Nitinol makes it an excellent material for energy storage [61]. The pseudoelastic parameters E_1, E_2 and permanent residual strain are defined in this figure. E_1 is the energy dissipated per unit volume in one complete cycle and E_2 is the stored energy per unit volume on loading and available for release during unloading. The efficiency for energy storage (η) is expressed in Equation 3.

$$\eta = E_2/(E_2+E_1) \quad [3]$$

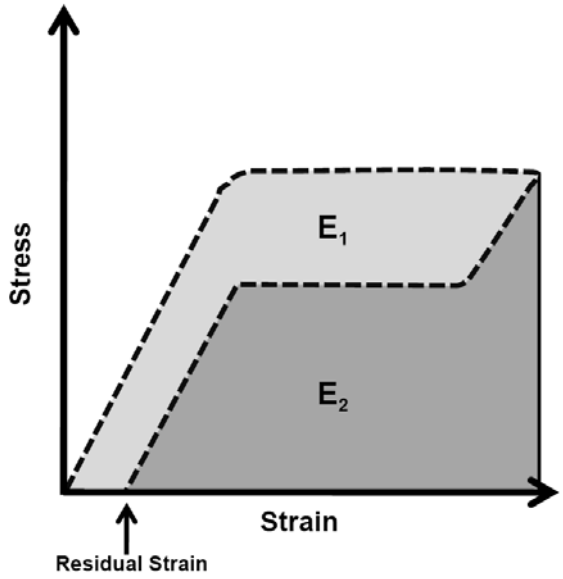

Figure 3-5: Typical loading-unloading curve for pseudoelastic NiTi alloy

3.4 Metallurgical Examination

Metallographic samples were prepared by polishing down to 2 μm diamond followed by 0.03 μm colloidal silica. Samples were etched in a 14 mL HNO_3, 3 mL HF and 82 mL H_2O solution for 25 s to 30 s to reveal their microstructure. Transmission electron microscopy (TEM) was carried out using a Philips CM12 microscope at 120 keV accelerating voltage. Hot and cold stages were implemented to permit control of phase transformation. TEM sample preparation was conducting using a Fischione ion milling system at -90^{o}C to minimize heat induced artifacts.

3.5 Thermal Analysis

Base metal DSC analysis was conducted using a Thermal Analysis Q2000 system equipped with a refrigerated cooling system (RCS). DSC curves were recorded over a temperature range from -50 ^{o}C to 40 ^{o}C under controlled heating and cooling rates of 5 ^{o}C/min. DSC samples were carefully extracted using an Acutome 50 precision saw with a ± 0.01 mm tolerance, as shown in Figure 3-6. However, due to the small specimen dimensions, remnant base metal material remained on the cut samples. DSC

analysis was conducted using a Thermal Analysis Q2000 system equipped with a refrigerated cooling system (RCS). Curves were recorded over a temperature range from -75^{o}C to 150^{o}C using controlled heating and cooling rats of 5^{o}C/min. Peak onsets were measured using TA Universal Analysis software (version 4.5). For simplification, the M_s temperature was used as a representative measure of overall transformation ranges, which is also used in literature to indicate changes in transformation behavior.

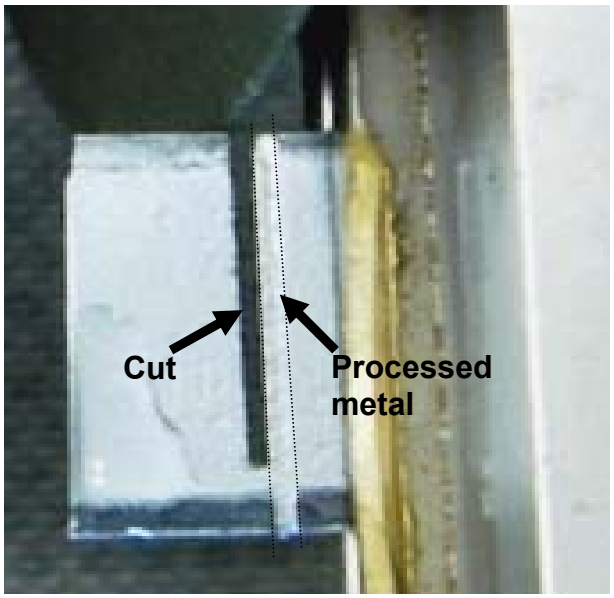

Figure 3-6: Laser processed sample being cut in Acutome 50 precision saw

4. EFFECTS OF LASER PROCESSING ON MECHANICAL PROPERTIES

Understanding the effects of laser processing on the mechanical performance of Nitinol is essential before its safe integration can commence in most applications. As comprehensive research on the base metal properties of various Nitinol alloys continues to be conducted [62], challenges faced with laser processing have plagued its integration and have yet to be resolved (Section 2.3.1). Previous studies have shown that laser processing parameters can greatly influence the mechanical properties of processed materials. As acknowledged in recent publications, the influence of laser processing parameters on the mechanical properties of Nitinol have yet to be detailed [2,3]. The current chapter details the effects of selected process parameters on the mechanical and pseudoelastic properties of Nitinol. In particular the stress strain behaviour of transverse laser processed tensile samples, hardness, energy absorption, residual strain and fracture surfaces were compared to the base metal.

4.1 Stress Strain Behavior

Comparisons between engineering stress-strain curves for representative un-processed and processed specimens of varying pulse frequency and power input are shown in Figure 4-1 and Figure 4-2, respectively. Typical pseudo-elastic behavior of austenite was observed for the base metal specimen, indicated by a flat region (plateau) after linear elastic straining near 0.03 mm/mm strain and 290MPa stress. Beyond 0.12 mm/mm strain, plastic deformation of martensite occurred and the load increased due to strain hardening, followed by failure near 0.90 mm/mm strain.

Figure 4-1 shows that the ductility and strength decreased significantly for the 0.6 kW laser processed specimen with higher pulse frequency (5pps, 10pps and 15 pps). This was due to premature failure in the processed region before sufficient stress could be applied to transform the adjacent base metal into martensite. However, a slight increase in ductility and strength was observed at the lowest pulse frequency of 1pps in the

0.6 kW sample (Figure 4-1). The 1pps sample was also able to reach strains capable of inducing plastic deformation of martensite along the gauge length. The engineering stress-strain curves for varying peak power (0.6, 0.7, 0.8 and 0.9 kW) with constant pulse frequency (10 pps), are shown in Figure 4-2. Except for the 0.6 kW sample, each of the other conditions (0.7, 0.8 and 0.9 kW) surpassed the pseudo-elastic region. However, the failure strength and ductility of all processed specimens were less than 70% and 50% of those of the base metal, respectively. The effects of processing parameters showed an increase in tensile strength with increasing peak power. Previous studies have shown similar reduction of fracture strain for laser welded NiTi alloys [44,46,48]. This reduction has been attributed to several factors including segregation of solute during solidification and the coarse-grain and dendritic structure in the processed metal. However current results showed that processing parameters can influence the mechanical properties; more specifically, higher energy input and lower pulse frequency yielded better mechanical performance.

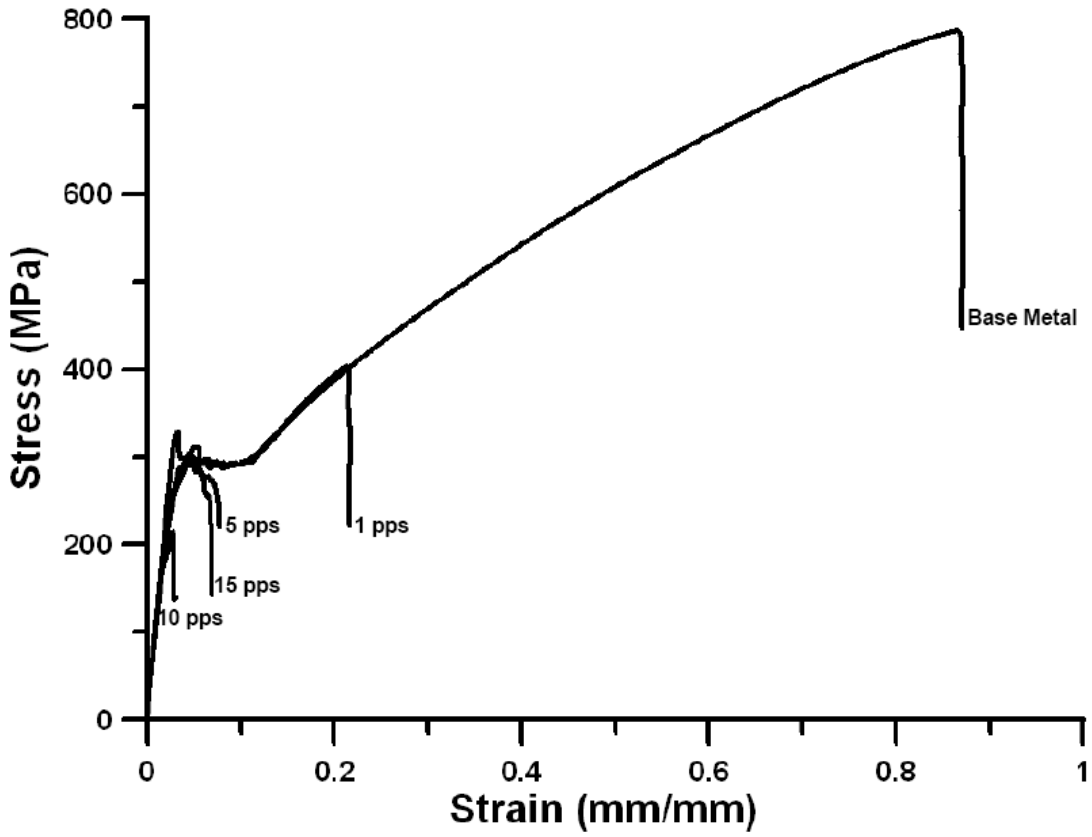

Figure 4-1: Representative tensile curves for varying pulse frequency for 0.6 kW power

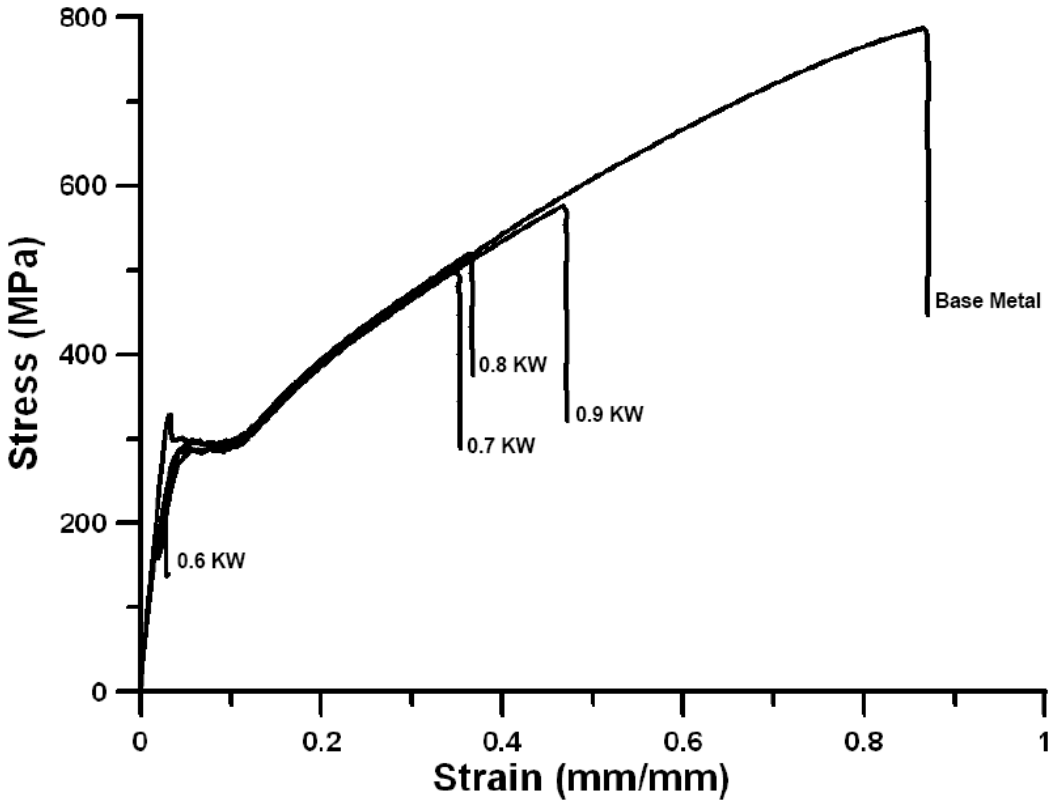

Figure 4-2: Representative tensile curves for varying peak power input for 10pps frequency

4.2 Pseudo-elasticity

Figure 4-3 details the stress-strain diagrams from elastic to the onset of pseudo-elastic deformation for un-processed and laser processed specimens for different peak powers. Typical pseudo-elastic behavior of NiTi due to stress induced martensite (SIM) transformation was observed during straining (austenite→ martensite) for most tensile specimens [1,62,63]. However, upon closer examination results revealed evidence of what appeared to be an initial plateau in the processed specimens which became more pronounced with increasing peak power. The initial plateau occurred in the processed region between 0.015 mm/mm and 0.022 mm/mm strain, while the second plateau is interpreted as reflecting the SIM transformation in the base metal (BM) stress-strain curve. This result suggests the processed area did not undergo similar SIM

transformation during straining before the usual pseudoelastic behavior of the base metal.

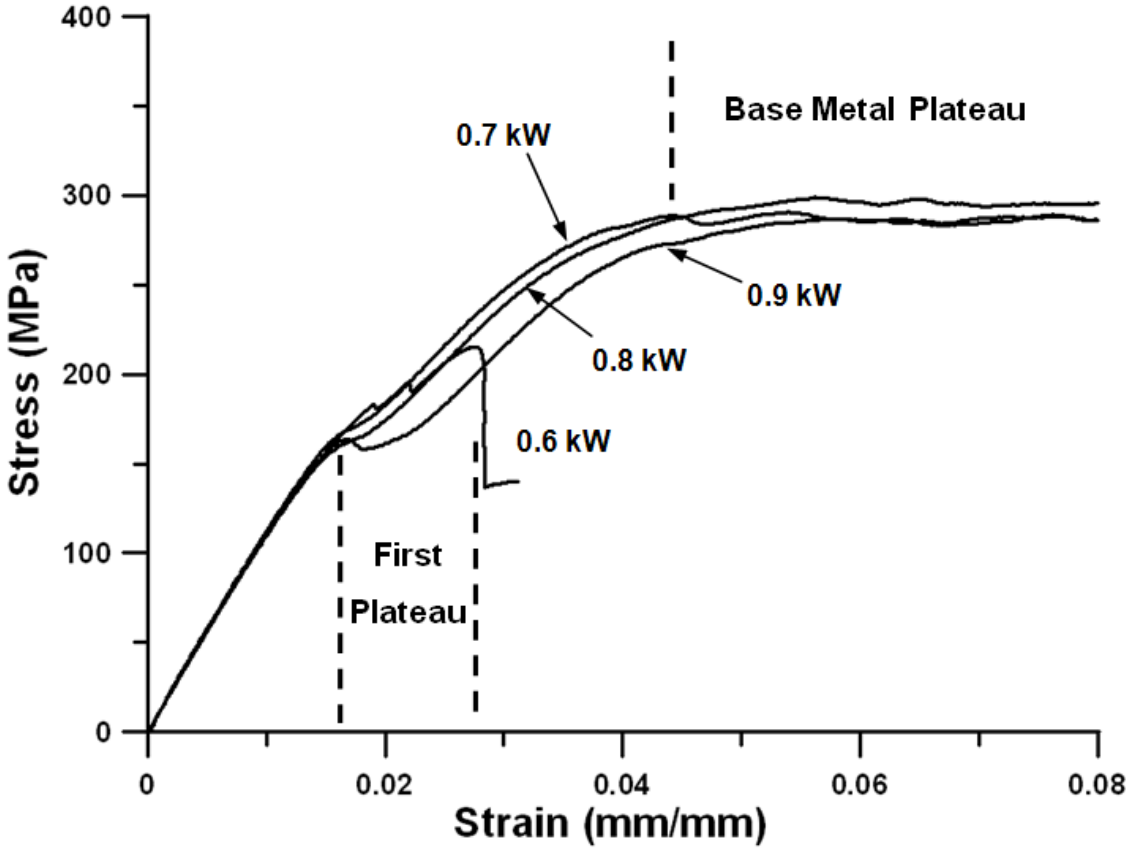

Figure 4-3: Detailed view of multiple plateaus in processed samples

During loading of the processed samples, the transverse tensile coupon induced stress in both the base and processed metal. Figure 4-4 shows a schematic of the different stages of deformation experienced during loading in Figure 4-3. As described in Chapter 3, the tensile sample consisted of unaffected base metal and a central region which has undergone processing. As shown in Figure 4-4a, the processed metal was only a fraction of the whole gauge length while the remaining material consisted of the unaffected base metal. Upon initial tensile loading, both regions experience elastic deformation until a critical stress is reached where the onset of the initial plateau occurs. Local permanent deformation experienced within the processed region, illustrated in Figure 4-4b resulted in the formation of the initial plateau. Additional straining then induced further elastic deformation of the remaining unaffected gauge length followed

by SIM transformation in the remaining gauge length (Figure 4-4c). Hence the presence of multiple plateaus results from separate deformation mechanisms occurring in the two separate regions. Furthermore, the amplified definition of the first plateau with increasing peak power may be attributed to the increasing width, as observed in Figure 3-3. Increasing peak power resulted in a larger minimum width. Accordingly, a larger area within the gauge length underwent the initial deformation.

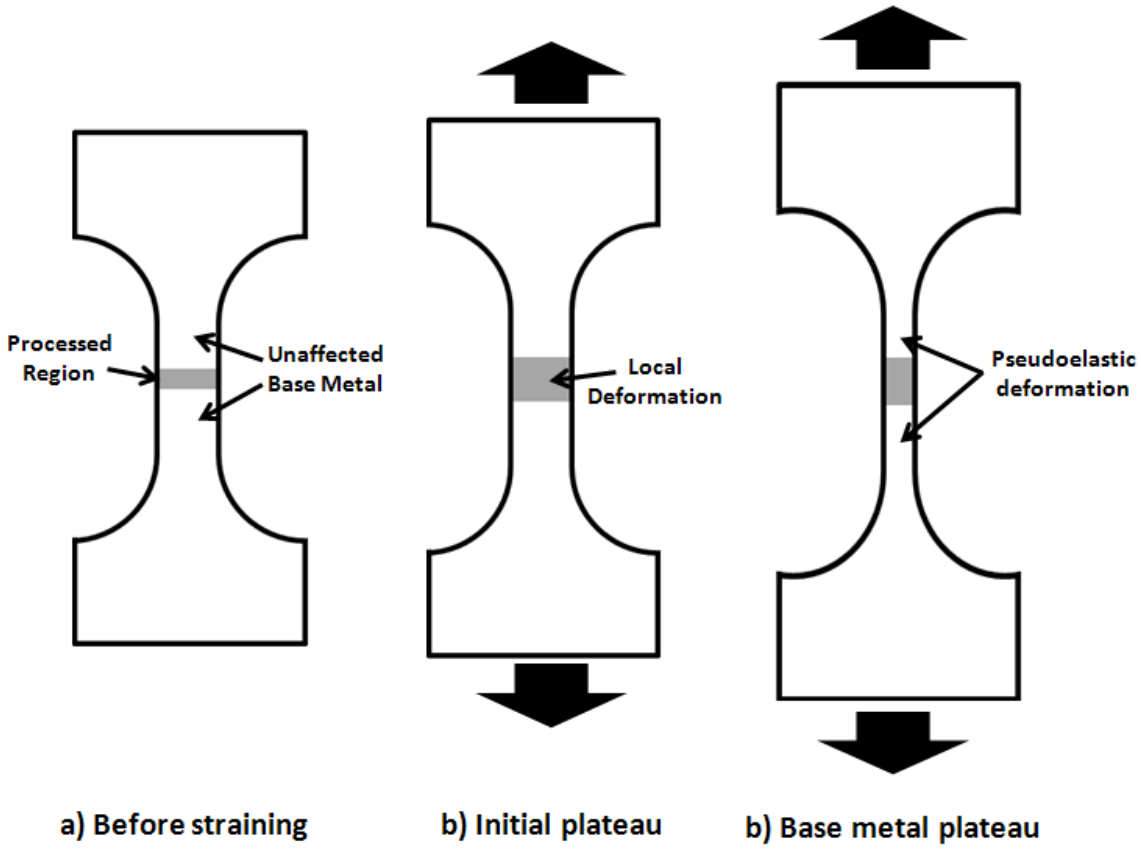

Figure 4-4: Schematic of deformation occurring in Figure 4-3

Nitinol properties can be strongly influenced by processing routes and techniques [1,23]. Re-melting due to laser welding alters base metal microstructure, which for Nitinol can result in the formation of dendrites or coarse grains and segregations at grain boundaries [44,45]. For example, in 1997 Schüßler conducted tensile tests on entirely re-melted test specimens (which consisted of a fully laser processed gauge length) [44]. A lower plateau stress for SIM formation and lower strain hardening during plastic deformation were observed compared to the base metal. Similarly in Figure 4-3

the initial plateau in the processed specimens appears to occur at a lower stress, which suggests SIM transformation possibly occurred in the processed region.

It is well known that SIM transformation is irreversible when sufficient additional stress is applied to induce plastic deformation of martensite [63]. In order to further examine the possibility of dual SIM transformation, a 2-cycle loading test was conducted. Figure 4-5 shows the first and second loading curves for the 0.9 kW, 10pps weld condition, which was strained up to 0.06 mm/mm. During initial loading, SIM transformation of the weld metal occurred followed by stresses high enough to induce plastic deformation of martensite. The second loading cycle showed the absence of the initial plateau and large permanent residual strain. This indicates permanent local deformation, possibly due to irreversible SIM transformation occurring within the processed region.

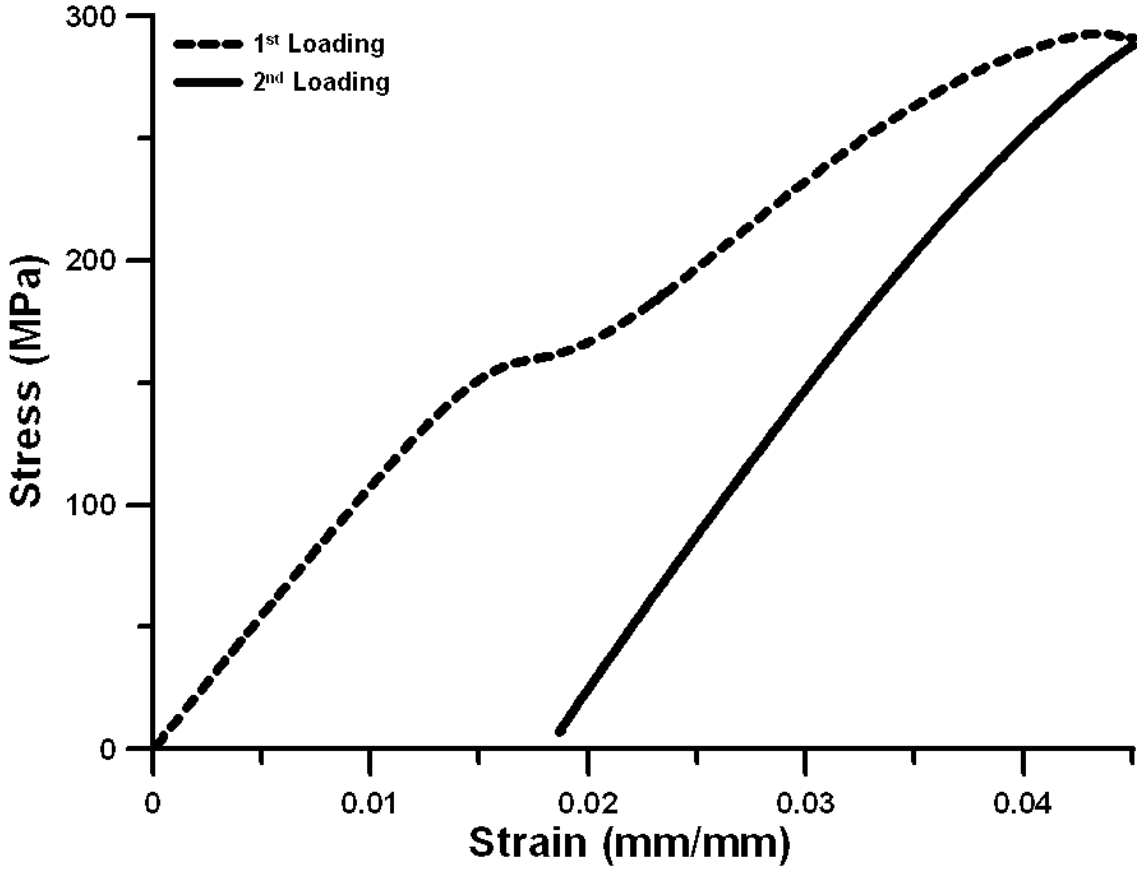

Figure 4-5: First and second loading curves for 0.9 kW, 10pps sample

Although the aforementioned results may suggest the occurrence of a lower SIM plateau, other factors can be responsible for the initial plateau. For example, abnormal room temperature phase shifts in Nitinol due to laser welding have also been previously reported [46]. These modifications to the processed metal may contribute to its altered SIM transformation behavior. However, more detailed microstructural analysis of the processed region is required in order to determine the key factors responsible for the initial plateau.

4.3 Energy Absorption and Cyclic Loading

The variation of efficiency for energy storage (η) and permanent residual strain with number of cycles (N) are plotted in Figure 4-6. Cyclic loading was not conducted on the 0.6 kW power laser processed samples with 5pps, 10pps and 15pps since premature failure occurred before 0.06 mm/mm strain. Figure 4-6a shows a rapid increase in permanent residual strain between 1 and 5 cycles for both unaffected base metal and processed samples. Beyond 5 cycles each material reached a steady state. The ability of a material to regain its original shape after unloading can be measured by permanent residual strain. All processed specimens showed higher permanent residual strain compared to the BM when straining up to 0.06 mm/mm. After 10 cycles the magnitudes of residual strain for base metal and processed samples were 0.020% and 0.026%, respectively. Figure 4-6b shows efficiency for energy storage (η) as a function of cycles (N). Both base and processed materials showed an increase in η up to 5 cycles. Laser processed material showed a slightly improved efficiency during the first 5 cycles. Beyond 20 cycles the efficiency stabilized near 0.9%. Hence compared to the base metal, processed samples showed higher overall permanent residual strain and exhibited slightly higher efficiency for energy storage during the initial 5 cycles.

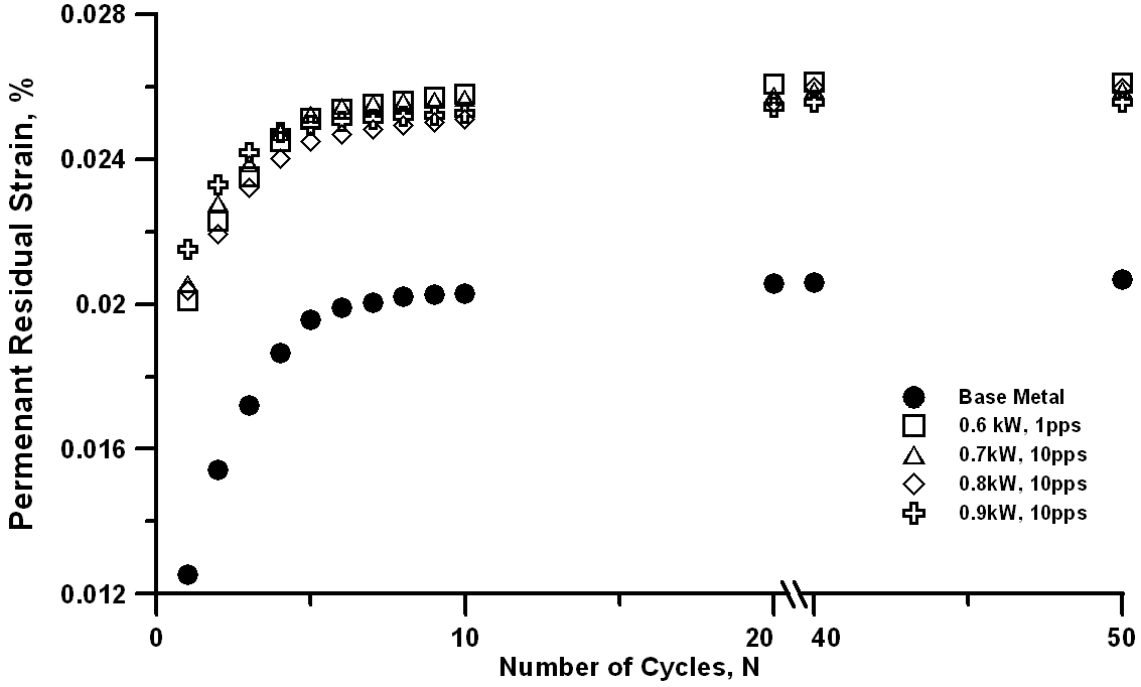

a) Permanent residual strain Vs number of cycles

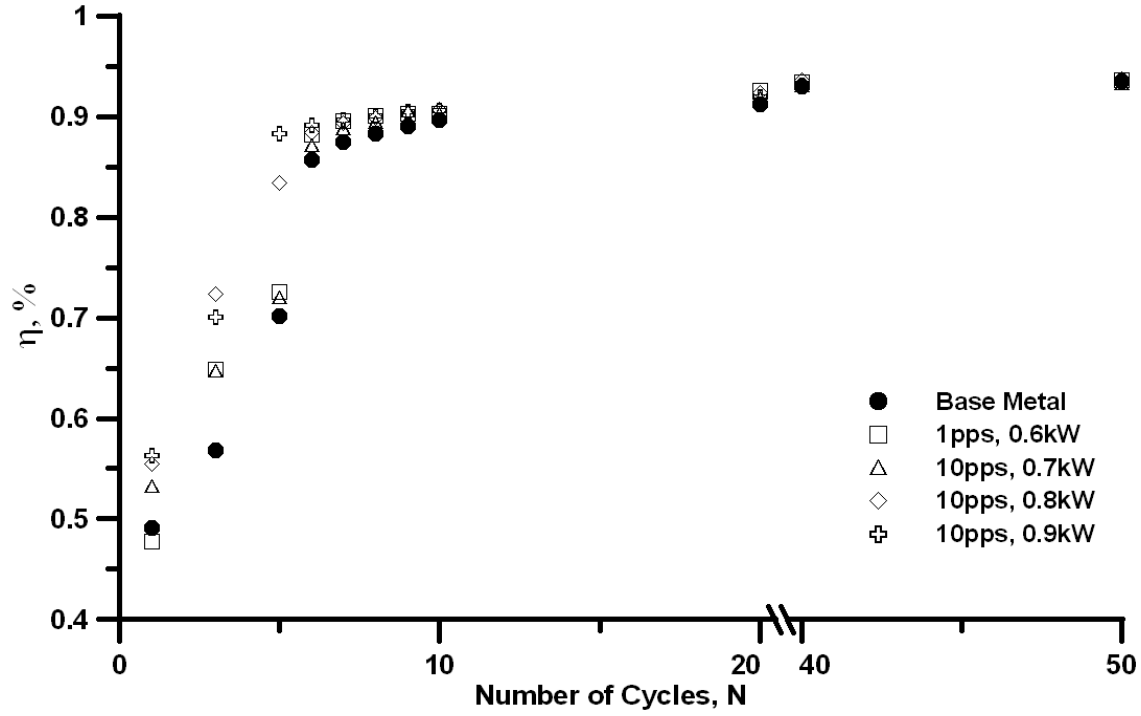

b) Efficiency for energy storage Vs number of cycles

Figure 4-6: Cyclic loading of unwelded and laser welded specimen up to 6% strain

As detailed in Figure 4-5, permanent deformation occurred in the processed region during the initial cycle. Therefore the increase in permanent residual strain of processed samples can be due to the permanent local yielding after the initial loading. In addition slight increase in permanent residual strain in the specimens made at higher power input can be attributed to the increased width. In 1994, Lin and Wu showed that improved η values can be attained by cold working of TiNi SMA [**Error! Bookmark not defined.**]. Similarly, the local processed area in the processed sample showed permanent deformation, similar to those experienced during cold working. Hence the improved efficiency for the welded specimens during the initial cycles may be attributed to the plastic deformation of the weld metal after the initial cycle where SIM transformation is induced.

4.4 Fracture Surfaces

Fracture surfaces for processed and base metal tensile specimens are shown in Figure 4-7 to Figure 4-9. For all laser processed tensile specimens, failure occurred within the re-melted region, whereas base metal samples failed arbitrarily in different region within the gauge length. The base metal fracture surface, shown in Figure 4-7, revealed a dimpled structure which was indicative of a ductile failure. Appropriately, the base metal sample experienced almost 90% strain while exhibiting the highest tensile strength of all tested samples.

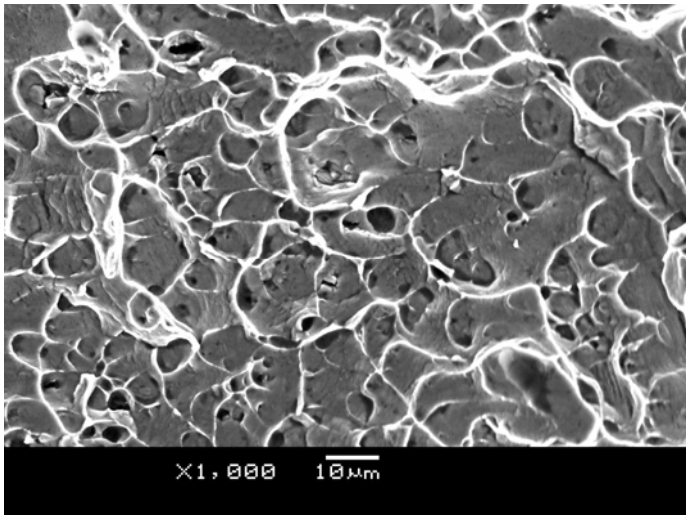

Figure 4-7: Fracture surface of base metal tensile sample

Distinctly different fracture surfaces were observed for laser processed samples having low tensile strength (i.e. below pseudoelastic plateau) as compared to the higher tensile strength. Figure 4-8a shows the fracture surface of the 0.6 kW and 1pps condition, which exhibited lowest tensile strength and did not surpass the pseudoelastic region of the stress-strain curve. A smooth fracture surface showing the directional dendritic solidification structure of the re-melted region was observed. This structure is indicative of transgranular failure where fracture propagates at the dendrite interface. Furthermore, dispersed fine particles were observed on the fracture surface; however, they were difficult to detail using the conventional SEM. Closer examination was facilitated using an FESEM, shown in Figure 4-8b, and revealed the particles were circular in shape and about 100-200nm in diameter. Attempts were made for compositional analysis; however, the relatively large interaction volume associated with SEM-coupled EDX analysis limited the identification of the phase of these particles.

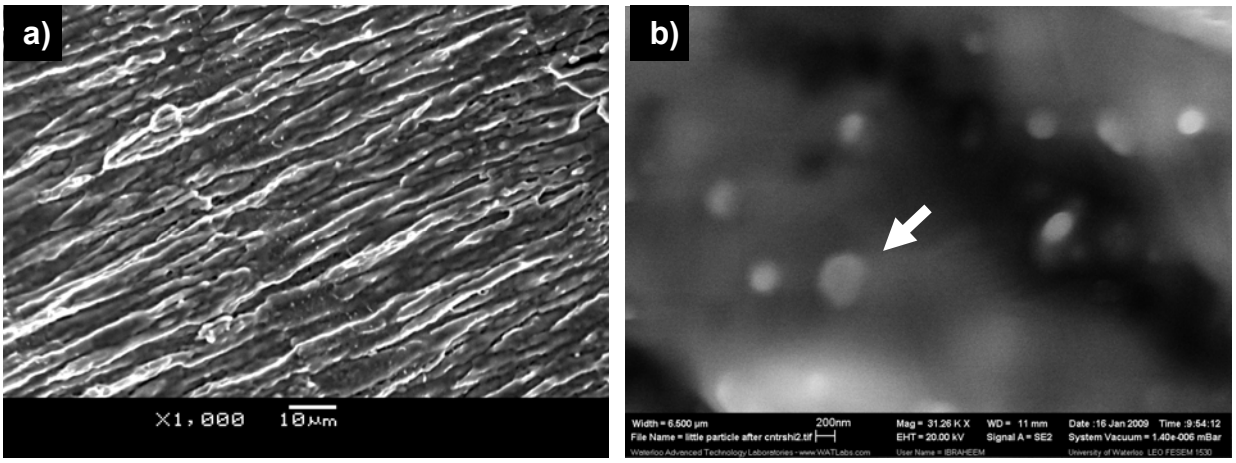

Figure 4-8: Fracture Surface of a) 0.6 kW, 10pps tensile sample with b) higher magnification showing finely dispersed particles

In contrast, the fracture surface for the highest strength condition (0.9kW, 10pps), shown in Figure 4-9, revealed a relatively coarser surface. When observed at higher magnification (Figure 4-9b) a finer dimpled structure was exposed, suggesting ductile intergranular failure through the dendrites within the re-melted region. In addition, the finely dispersed particles were not as prevalent in this sample. These results reveal that changing process parameters can result in different failure modes. However, at this

point detailed microstructural analysis of the re-melted region is required to determine the mechanism responsible for failure mode transition.

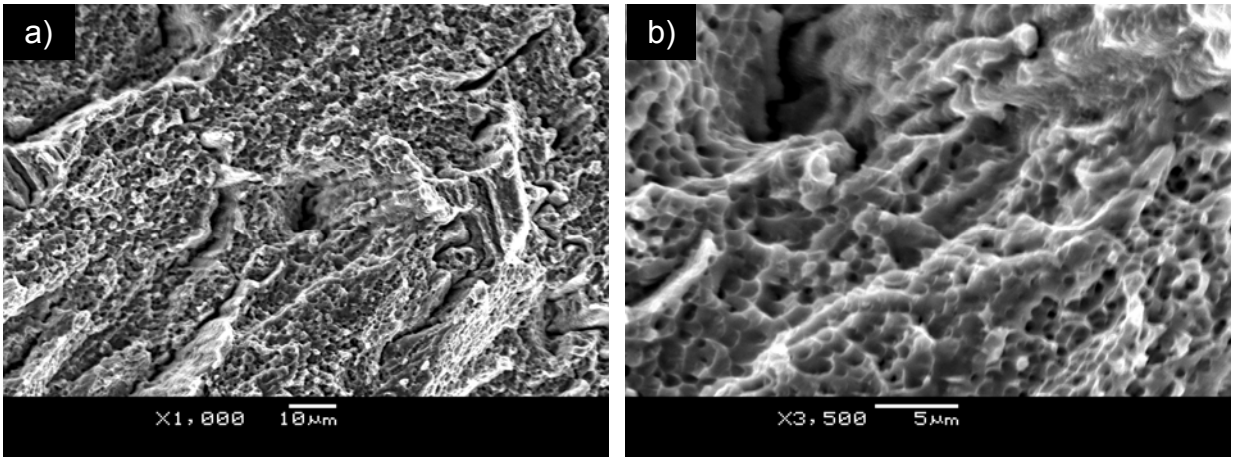

Figure 4-9: Fracture surfaces of a) 10pps 0.9k W, 10pps tensile specimens with b) high magnification image

4.5 Hardness Traces

Figure 4-10 shows the hardness traces along the cross-sections of the processed region. Along the x-axis, all samples exhibited a decrease in hardness within the processed region. Hardness values increased gradually away from the weld centerline before finally converging to that of base metal. Base metal hardness values ranged near 370-400Hv. Minimum weld hardness was observed in the 0.6 kW, 10 pps condition, which approached 250 Hv. In contrast the 0.6 kW, 1 pps and 0.9 kW, 10 pps conditions exhibited minimum hardness values near 280Hv. Lower hardness in the centre of the previously annealed materials can be attributed to resolidification induced by processing, which can result in larger nearly strain-free recrystallized grains.

Hardness values along the y-axis of the centerline, shown in Figure 4-10, were similar among samples. Hardness values of the 0.6 kW, 10 pps condition bottom showed slightly lower hardness values when compared to the surface. Hardness of the 0.6 kW, 1 pps was scattered across the centerline, similar to the pattern in the longitudinal direction. However, 0.9 kW, 10 pps showed relatively uniform hardness values in the transverse direction.

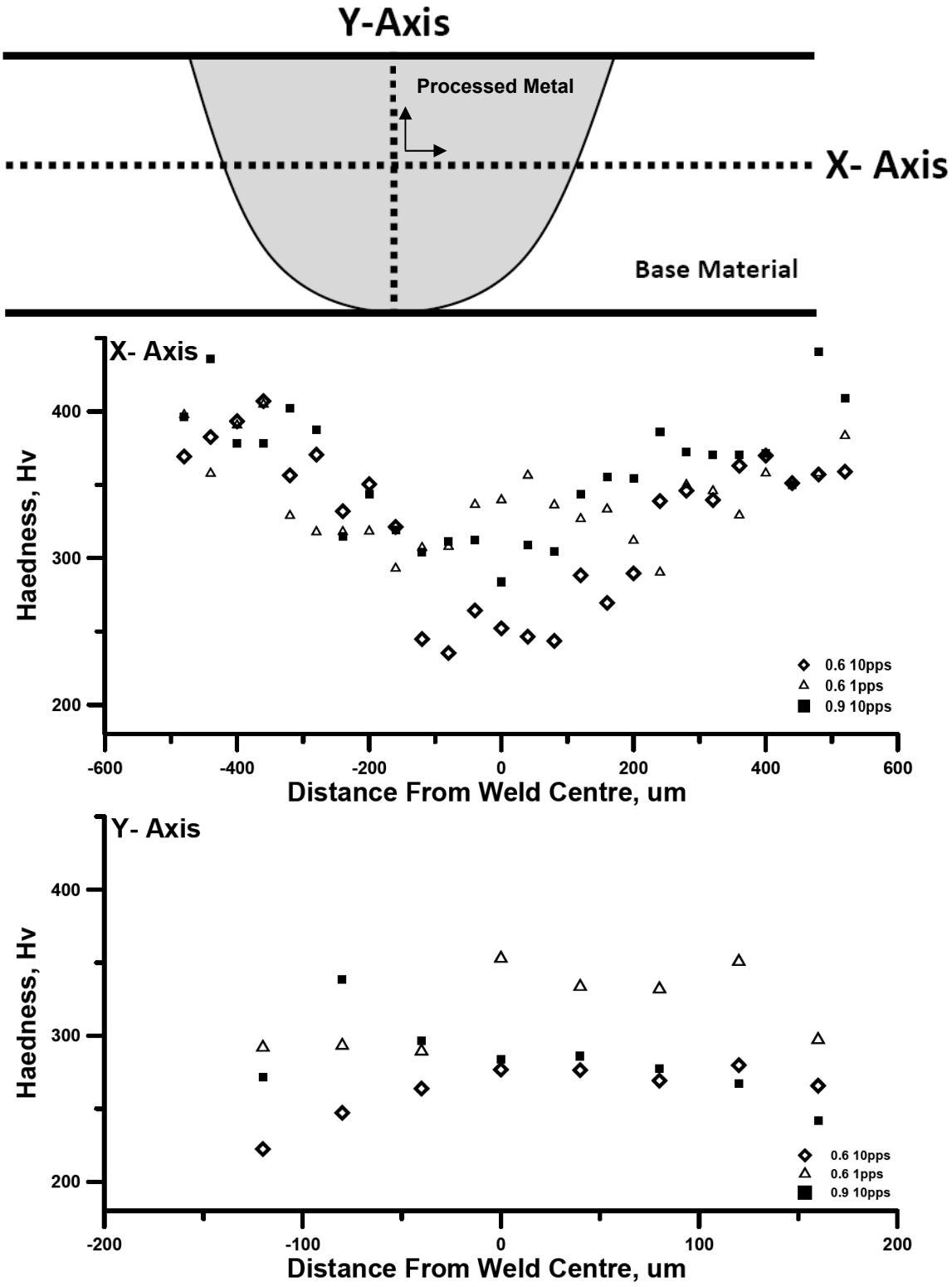

Figure 4-10: Microhardness trace along vertical and horizontal axis

4.6 Chapter Summary

The current chapter detailed the mechanical properties of pulsed ND:YAG laser processed Nitinol. The strength, pseudoelastic and cyclic loading properties for varying process condition were compared with the base material and fracture surfaces were analyzed. Parameters (energy input and welding speed) were shown to strongly influence the mechanical properties (tensile strength and ductility) of the laser processed Nitinol alloy. Higher energy input and lower speed resulted in improved mechanical performance. The laser processed samples also showed higher permanent residual strain and exhibited slightly higher efficiency for energy storage during the initial 5 cycles compared to base material.

Evidence of multiple plateaus was observed in laser processed specimens during transverse tensile loading. These plateaus resulted from two separate SIM transformations during tensile deformation (remolten and base metal). The additional plateau became more pronounced with increasing peak power. In the context of this chapter, it was unclear *what caused this initial yielding plateau.*

Fracture surfaces of base material revealed ductile dimpled surfaces. In contrast, both ductile and brittle failure modes were observed in laser processed samples depending upon process parameters. Finally, submicron second phase particles were also present within the fractured samples but the small size made it difficult to characterize and identify the origins.

5. EFFECTS OF LASER PROCESSING ON MICROSTRCUTRE AND PHASE TRANSFORMATION

Results in the previous chapter showed that some degree of deterioration in mechanical performance in laser processed samples always occurred, when compared to the as-received Nitinol base metal. Laser processing parameters were also shown to greatly influence the mechanical properties, with some parameters having substantially more positive effects than others. However, another key functional property of Nitinol alloys is their ability to undergo solid-state diffusionless transformation which greatly influences the shape memory effect and has also been closely linked to its pseudoelastic performance. Hence, the aim of the current chapter is to detail the effects of select laser processing conditions on the stable room temperature phase. In particular, the effects on microstructure and phase transformation temperatures are examined. Processing conditions selected for analysis in the current chapter represents the lowest (0.6 kW, 10pps), intermediate (0.6 kW, 1pps) and highest (0.9 kW, 10pps) mechanical performance from the previous chapter. Finally, correlations are made between the transformation behavior and altered mechanical properties observed in Chapter 4.

5.1 Optical Metallographic Analysis

Optical micrographs showing overall cross-sections of samples obtained under the selected processing conditions, with and without polarized light, are shown in Figure 5-1. As expected from quantified measurements in Figure 3-3, the lower peak power (0.6kW at 1pps and 10pps) processing conditions yields a smaller minimal width as compared to the higher peak power (0.9kW, 10pps) condition. All conditions yield a typical banded structure within the processed region, created during each pulsing thermal cycle. Segregated second phases could be observed within the process region. The use of polarized light aided in highlighting locations of higher second phase concentrations near the top surface for each condition.

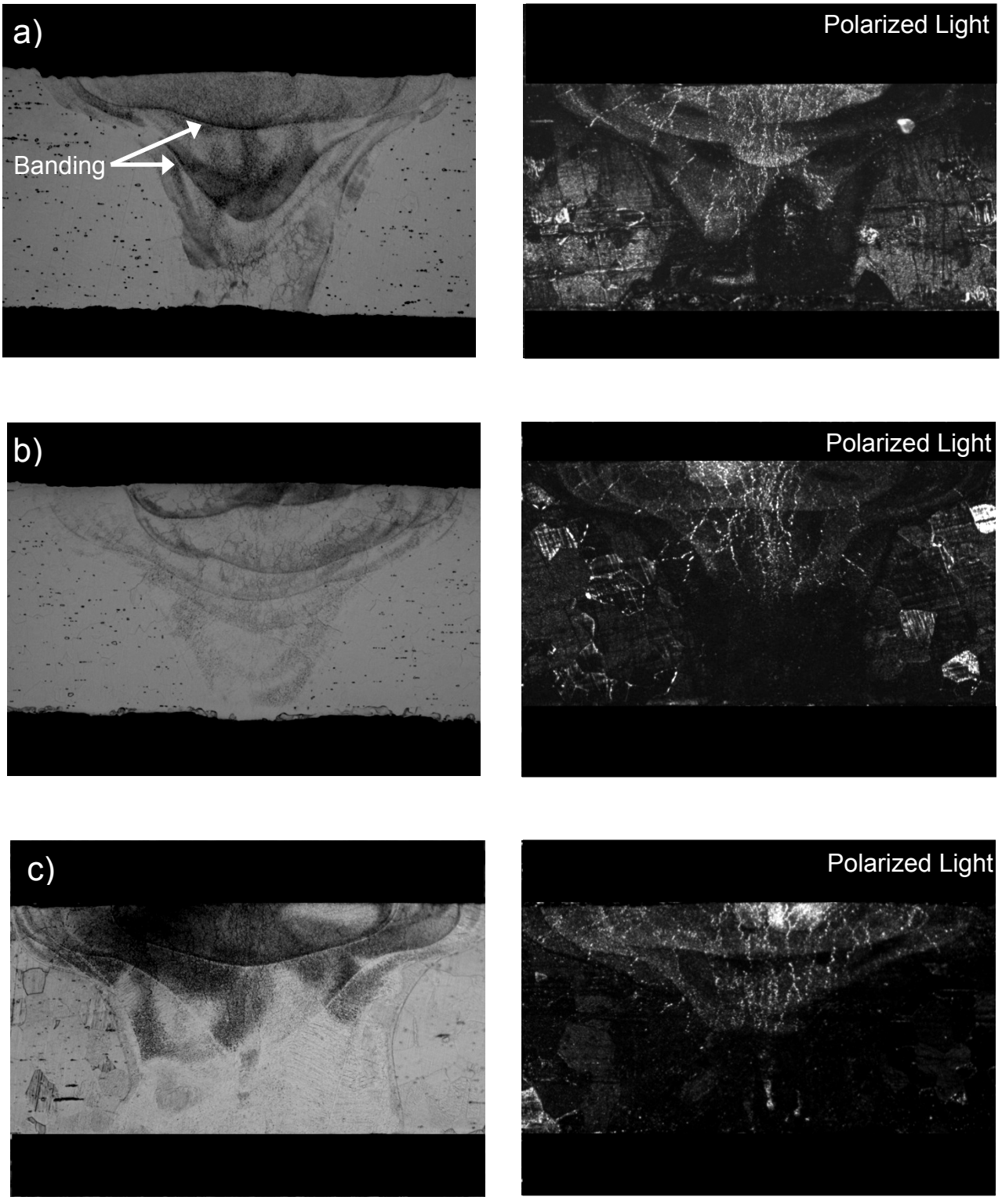

Figure 5-1: Cross-section of samples generated at (a) 0.6 kW, 10 pps, (b) 0.6 kW, 1 pps, and (c) 0.9 kW, 10 pps processing conditions

Closer views of the base metal and boundary near the re-solidified region are shown in Figure 5-2a and b. Annealing of the as-received material resulted in a homogeneous single-phase microstructure, with the formation of relatively large NiTi grains (about 20-40um). A similar base metal grain structure is observed near the interface of the re-solidified region, shown in Figure 5-2b. However, a heat affected region is not identifiable, which is expected due to the large base metal grains and low heat input inherent to the pulsed Nd:YAG process [**Error! Bookmark not defined.**]. Columnar dendritic growth was observed along the solidification interface. Within the re-solidified region, finely dispersed circular particles are visible; however their characterization using optical microscopy is limited.

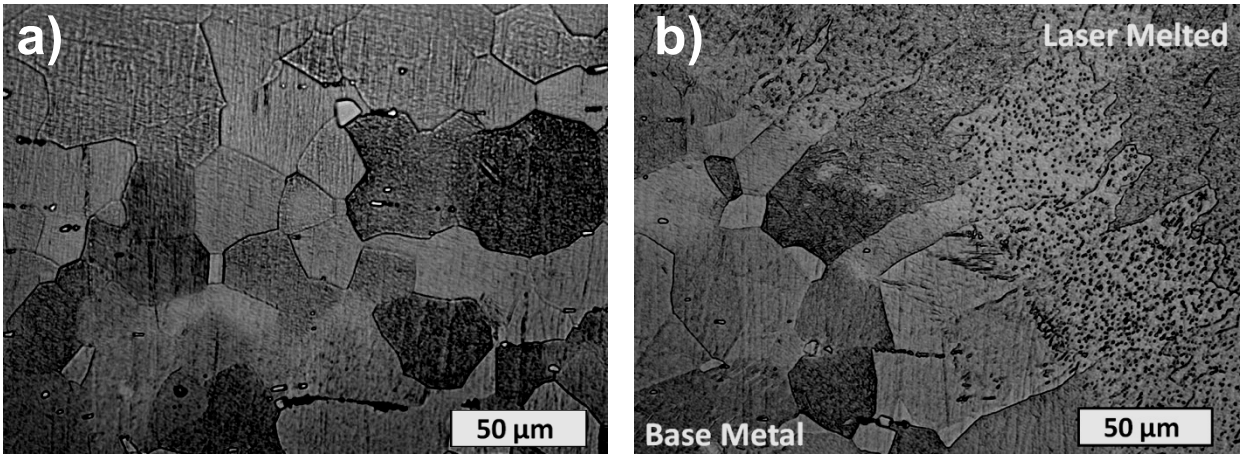

Figure 5-2: Optical micrographs of (a) base material and (b) re-solidified interface

High magnification microstructures near the top of the processed region for the selected conditions are shown in Figure 5-3. Each condition exhibits varying amounts of continuous sub-micron segregation. The 0.6 kW, 10 pps sample shows a high density of continuous intergranular segregation. In contrast, the 0.6 kW, 1 pps condition shows a relatively lower density of similar segregation. However, intermittent second phase distribution is observed at 0.9 kW, 10 pps. Segregated phases in the processed metal can act as preferential sites where failure initiates or propagates. The varying amounts of segregation can be correlated to the mechanical performance observed earlier in Section 4.1 (in Figure 4-1 and Figure 4-2). The densely segregated condition (0.6 kW, 10 pps) exhibits the poorest mechanical performance while the condition showing intermittent segregation 0.9 kW, 10 pps (0.6 kW, 10 pps) is founds to have relatively

better performance. Hence these second phase particles may contribute to the altered mechanical performance observed in Chapter 4.

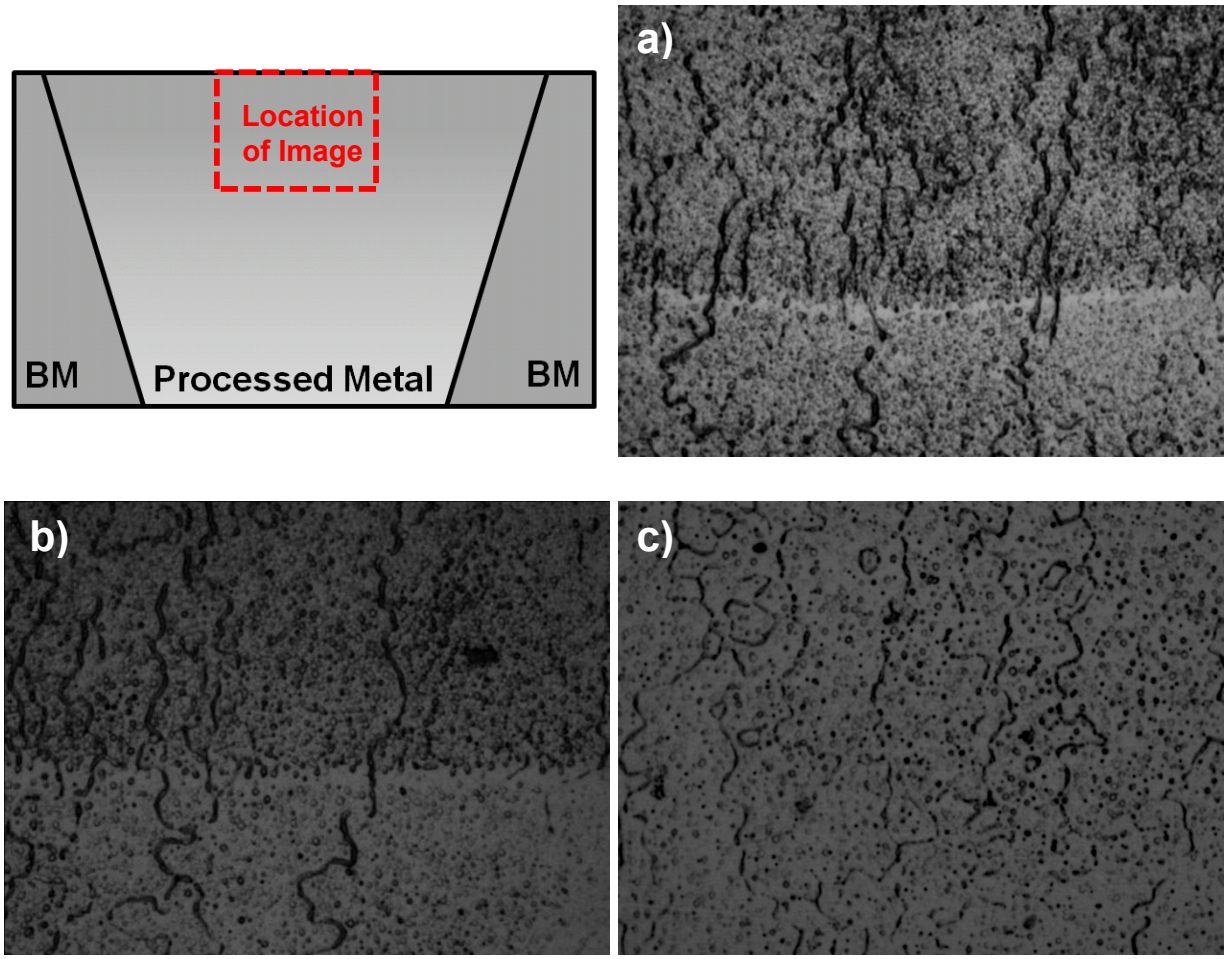

Figure 5-3: Fusion zone microstructure for (a) 0.6 kW, 10 pps (b) 0.6 kW, 1 pps, and (c) 0.9 kW, 10 pps

5.2 Thermal Analysis

Laser processed samples were subjected to thermal analysis using DSC methods, the results of which were compared to unaffected base metal. Figure 5-4 shows a schematic of the test specimens of the laser processed sample used for DSC analysis which included both unaffected base metal and the processed region. Although DSC samples were carefully extracted using a precision saw, remnant unaffected base metal material remained on the cut samples due to the small specimen dimensions.

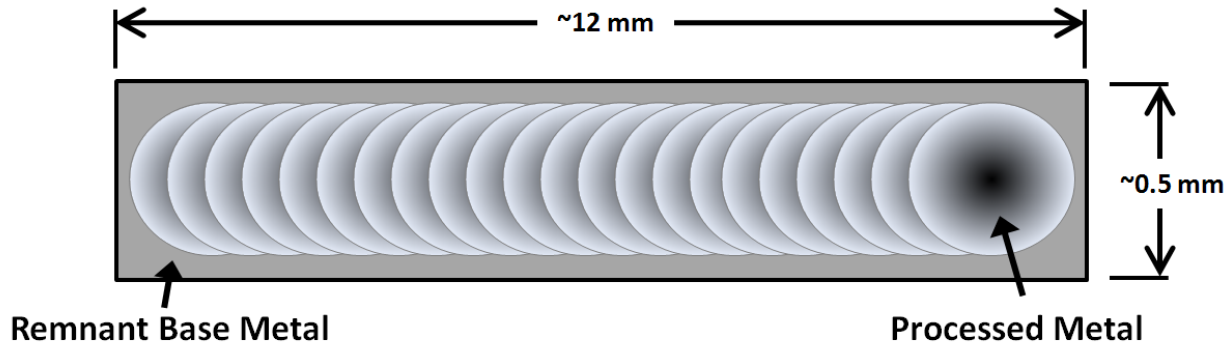

Figure 5-4: Schematic of laser processed DSC sample with overlapped pulses

DSC curves for the base material and select processing conditions are shown in Figure 5-5. For the base metal, both austenite finish (A_f) and martensite start (M_s) temperature were below room temperature at -8.6°C and -33.3°C, respectively. This indicated the phase at room temperature is predominantly austenite and so pseudoelastic behavior should be observed during tensile testing. In comparison, the processed samples exhibited multiple thermal events, including a pair of high temperature and low temperature peaks. Similar low temperature thermal events were observed for all samples; however the pair of higher temperature peaks was unique to each variety of the processed samples. Residual un-melted material on these samples after cutting could account for the low temperature peaks, which also had transformation temperatures similar to the base metal. The distinct high temperature peaks then suggest the occurrence of a completely separate transformation.

It should be noted that additional DSC peaks are typically observed in cold worked or aged Nitinol during R-phase transformation. However, in the presence of the R-phase, an intermediate transformation would produce a peak between austenite and martensite during cooling [64]. The present data show two distinct transformation peaks outside of that range. In addition, the fully annealed base material did not show any presence of R-phase transformation, due to preservation of the solid solution by quenching to room temperature. Hence, these additional peaks suggest the presence of multiple phase transformations, including a low temperature (< room temperature) and high temperature (> room temperature) transformation. In turn, quantified peak onsets provided in Table 2 assume two separate starts and finish temperatures (high and low) for the reversible austenite/martensite transformation.

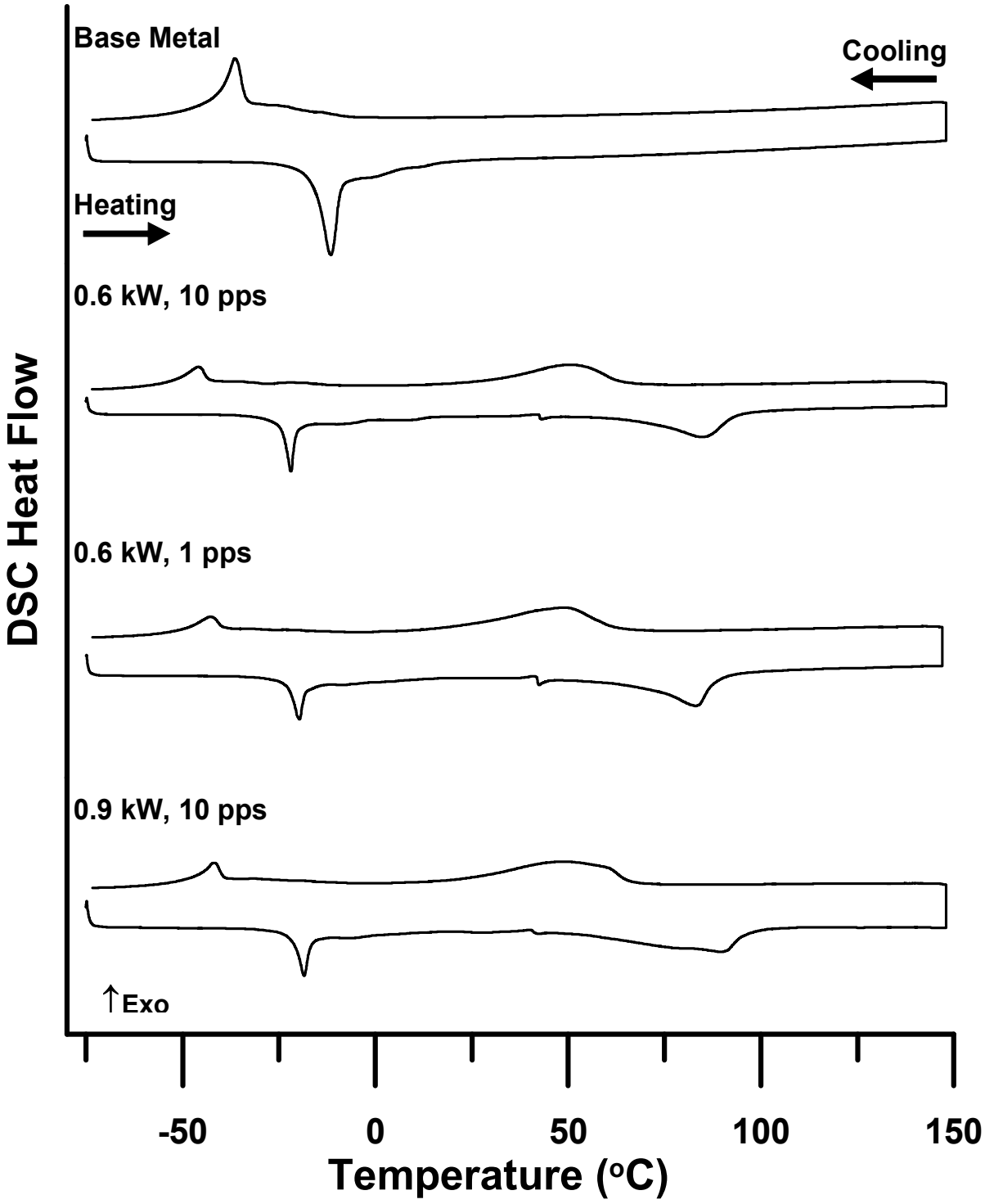

Figure 5-5: DSC scans for base and processed metal

Table 2: Peak onset temperatures for DSC scans in Figure 5-5

	Low Temperature Transformation (^oC)				*High Temperature Transformation (^oC)*			
	A_s	A_f	M_s	M_f	A_s	A_f	M_s	M_f
Base Metal	-16.1	-8.6	-33.3	-44.2	Not Present			
0.6 kW, 10 pps	-20.2	-14.8	-37.7	-48.8	71.0	89.3	62.6	22.1
0.6 kW, 1 pps	-21.0	-16.0	-39.3	-47.2	52.1	96.8	66.1	24.0
0.9 kW, 10 pps	-24.5	-21.0	-43.3	-53.0	67.6	94.0	64.5	29.3

Grain coarsening has been shown to slightly lower transformation temperatures of Nitinol alloys [65]. Materials that have undergone laser processing often contain a heat affected zone (HAZ) where grain coarsening is often observed. This is more prominent in materials originally having a small grain structure induced by thermo-mechanical processing during the manufacturing stages. This was observed by Ogata et al. who showed increased grain size in the HAZ region after laser processing of heavily cold worked NiTi alloys [66]. However, as observed in Figure 5-2, in the present case the annealing procedures carried out prior to laser processing retained a relatively large base metal grain structure, such that HAZ coarsening was not detectable in the microstructure. Influences of HAZ coarsening on transformation temperatures were expected to be removed due to the annealing procedures. Furthermore, transformation temperatures showed a distinct increase, which is contrary to the effects observed in coarsening. Hence, in-depth phase analysis was required for identifying the multiple thermal events occurring in laser processed DSC results.

5.3 Room Temperature Micro-XRD Phase Analysis

Room temperature (21^{o}C) XRD data showing indexed peaks for the base and processed material are shown in Figure 5-6. As expected from the DSC results, base metal peaks identified the sole presence of the simple cubic austenite phase. Conversely, both austenite and martensite phases were detected in the laser processed samples. The collimator diameter (~500 μm) implemented in collecting XRD data was slightly larger than the width of the processed region (~400 μm) and can account for the detection of austenite. However, the detected martensite clearly indicated that local

phase change was induced by the laser processing technique. XRD results corroborated well with the DSC data, which showed transformation to austenite for the processed metal completed above 89.3^{o}C, which is well above room temperature (Table 2).

It is important to note the effects of sample texture on XRD results. In particular, there are notable differences in relative peak intensities within the processed material. The development of a directional solidification structure can cause abnormally high intensities for certain peaks depending on the sample orientation. Although all peaks may not be detected, the XRD method can still provide reliable phase identification for such samples. As such, the additional unlabeled faint peaks in Figure 5-6 (i.e. near 35, 57, 69, and 74 degrees) within the processed metal also corresponded to martensite, as determined by the referenced work [67]. In addition, XRD analysis was unable to detect the presence of the second phase particles that were observed optically in Figure 5-3. This is likely due to the lack of grain population required to produce a detectable signal. Hence detailed microstructural observations (including TEM) were required to identify and characterize the submicron segregated phases within the processed metal.

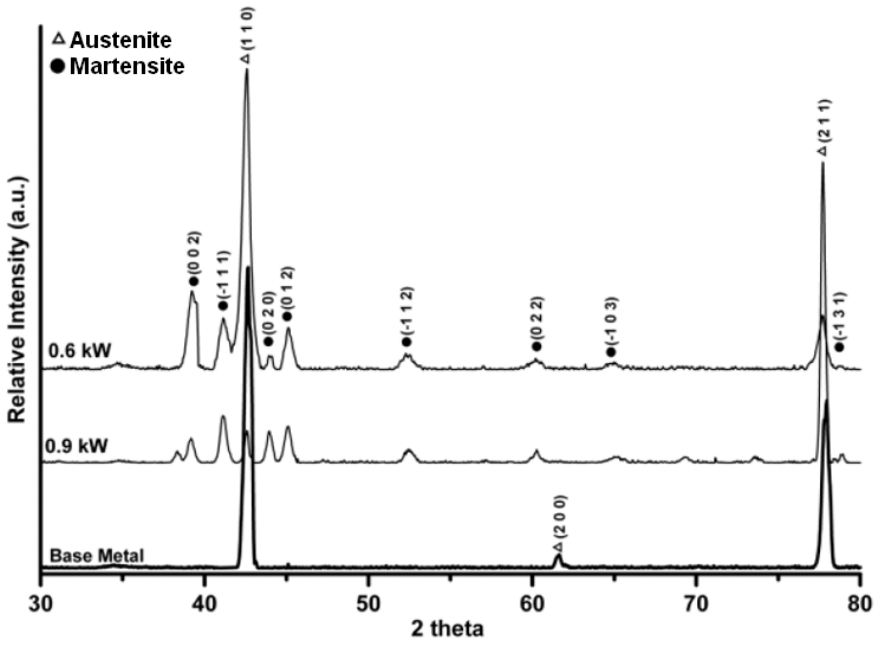

Figure 5-6: Room temperature XRD data for processed and base metal

5.4 TEM Analysis

Detailed phase characterization facilitated by temperature controlled TEM microscopy further confirmed the local phase alteration due to laser processing. First, base metal TEM microstructure was observed at 21°C and -50°C at the same site, shown in Figure 5-7a and b, respectively. Recalling the DSC results in Figure 5-5, base metal completes martensitic transformation at temperature near -50°C. Similarly, decreasing sample temperature demonstrated the transformation from simple cubic austenite to twinned martensite. Upon heating back to room temperature complete reversal of the transformation was observed.

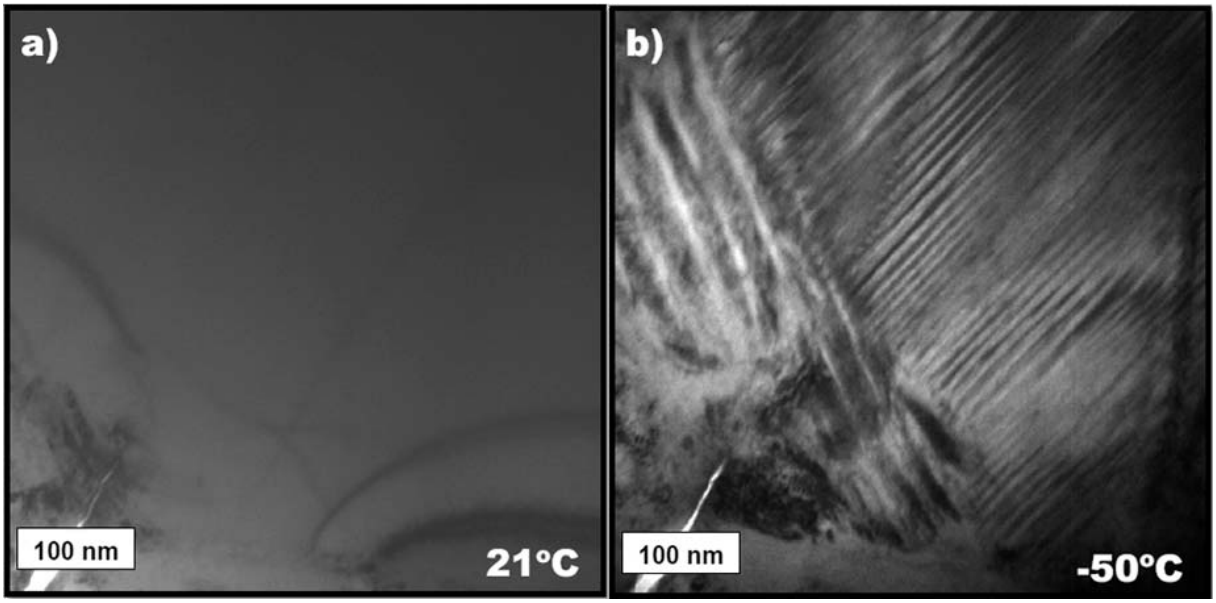

Figure 5-7: Base metal TEM microstructure at a) 21°C and b) -50°C

TEM observation of the representative 0.6kW, 10pps processed metal at 21°C and 100°C is shown in Figure 5-8. The presence of existing twinned martensite at 21°C confirmed the aforementioned XRD and DSC results. Figure 5-8b shows the effect of subsequent heating of the sample to 100°C that induced the solid state transformation into simple cubic austenite. Hence, observations show laser processed material exhibiting higher transformation temperature when compared to the original base metal which coincides with the high temperature DSC peaks.

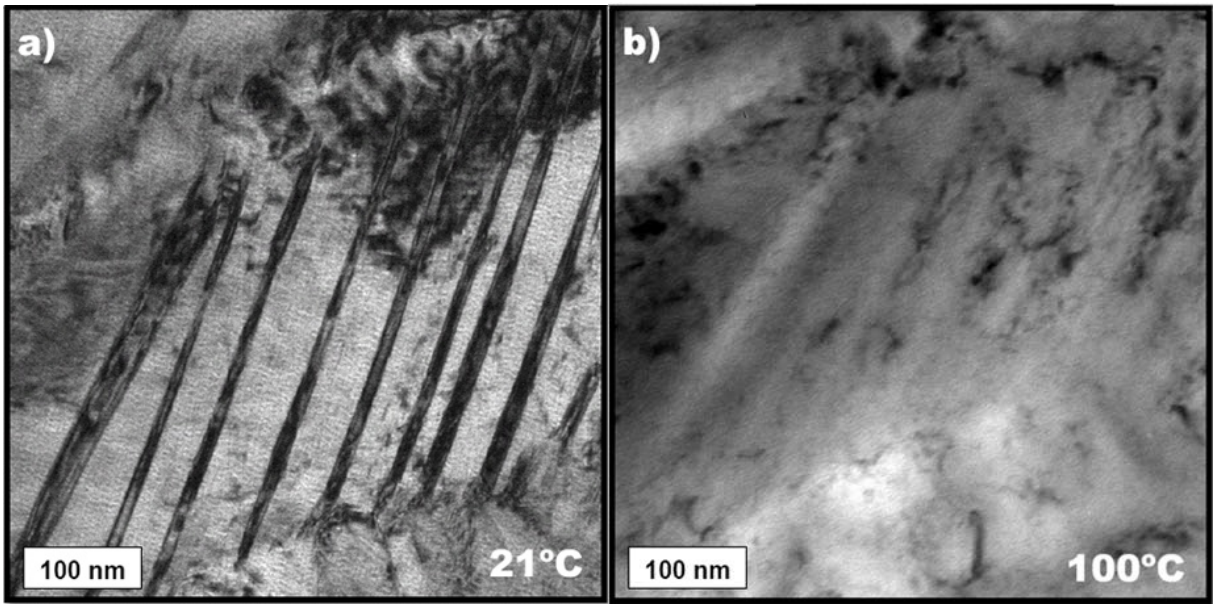

Figure 5-8: 0.6 kW processed metal TEM microstructure

Further TEM microscopy was implemented to characterize the finely dispersed particles observed optically in the processed metal. Figure 5-9 shows a pair of circular particulates roughly 100-150nm in diameter and surrounded by a twinned martensite matrix. Energy dispersive x-ray analysis (EDX) identified the particles as Ti_2Ni intermetallic by detection of Ti and Ni atomic compositions of 66.3at.% and 33.6at.%, respectively.

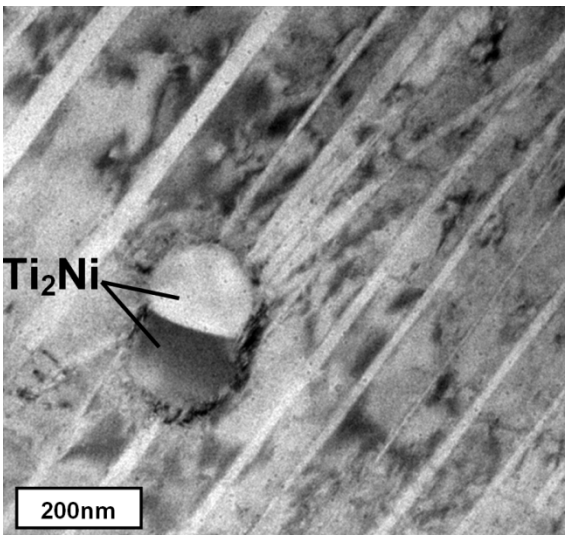

Figure 5-9: TEM micrograph showing Ti_2Ni embedded in martensite matrix

Similarly, aligned particles were observed within the processed region, as shown in the FESEM image in Figure 5-10a. TEM-coupled EDX analysis also identified these as aligned Ti_2Ni particles embedded within a twinned martensite matrix. Although Ti_2Ni is an intermetallic present in the binary NiTi phase diagram (Figure 2-10), it is most stable in the Ti-rich domain alloy. However, in the present study, a Ni-rich alloy was formed which would intuitively be more susceptible to form stable Ni-rich intermetallics (i.e. Ni_3Ti). Hence the presence of this Ti-rich intermetalic suggests a local change in chemistry toward a Ti-rich composition.

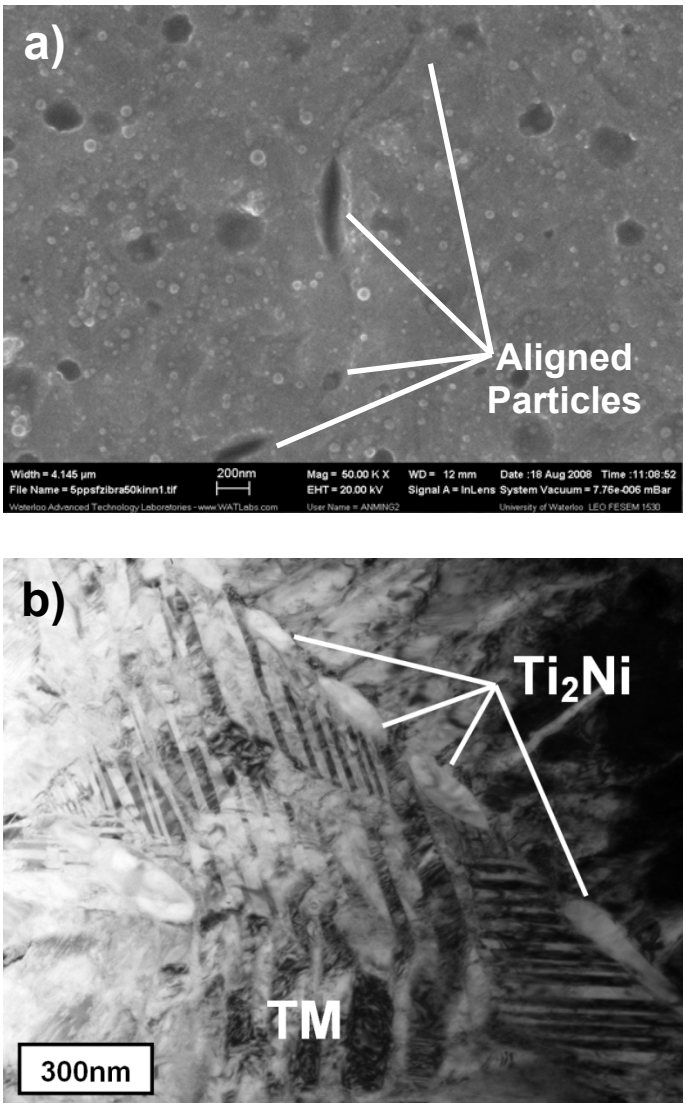

Figure 5-10: Processed region a) FESEM and b) TEM microstructure showing aligned Ti_2Ni particles

5.5 Effect of Laser Processing on Solid-state Transformation

A schematic detailing the thermal events observed during DSC analysis is shown in Figure 5-11. The three distinct temperatures shown occur below (T_1), between (T_2) and above (T_3) the high and low thermal events. Figure 5-11a shows the laser processed DSC samples comprised primarily the processed metal with remnant base material. Although Ti_2Ni was discovered via TEM analysis of the processed metal, it does not partake in the low temperature solid-state transformation. At T_1 temperatures below the lower thermal event the whole sample is in the martensitic phase (Figure 5-11b). As the temperature increases (heating) to T_2, the remnant base metal transforms from martensite to austenite and produces the endothermic DSC peak, while the processed material remains unchanged (Figure 5-11c). Upon further increase in temperature to T_3, the processed material subsequently undergoes the final solid-state transformation into austenite and produces the second endothermic DSC peak (Figure 5-11d). The reversible properties of these transformations means upon cooling similar exothermic peaks would be produced which would be slightly offset due to the hysteresis nature of transformation.

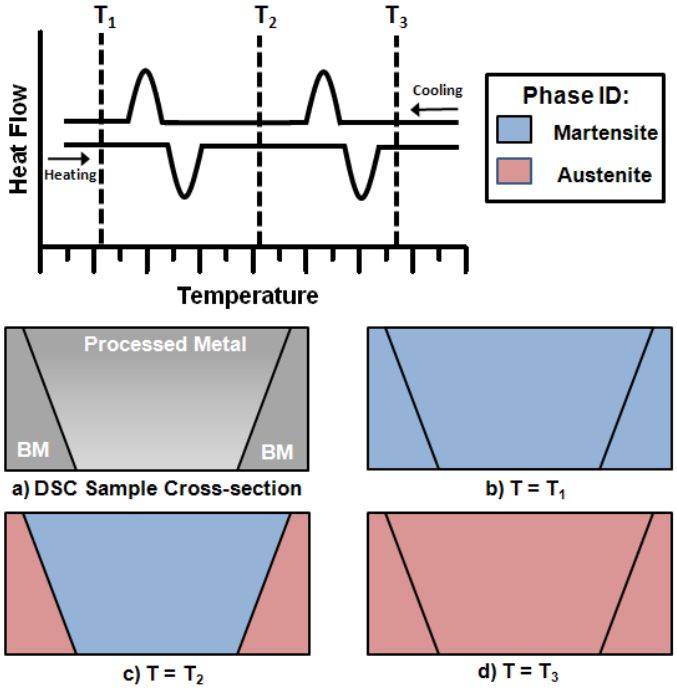

Figure 5-11: Schematic of DSC thermal event

Compared to published research, current results reveal substantial changes to local transformation temperatures induced by pulsed Nd:YAG laser processing. In particular the stable room temperature phase was converted from austenite to martensite. Thus, these results are contradictory to those observed by Hsu et al. who reported a slight decrease in transformation temperature after CO_2 laser welding of Nitinol [46]. A detailed understanding of microstructural and phase changes induced by welding is critical to the design and fabrication of medical devices, particularly when shape memory or good mechanical performance is required. Transformation temperatures are known to be affected by both thermo-mechanical processing and change of the Ti/Ni ratio [64], both of which can be experienced during laser welding due to the applied thermal cycles and local vaporization, respectively. However, the specific mechanisms responsible for the changes detailed in the current study are not fully understood. Therefore, further detailed investigation of the mechanism responsible for phase alteration and methods to either minimize or control these effects is still required.

5.6 Effects of Phase Transformation on the Mechanical Properties

Recalling from Chapter 4 (Section 4.2) during tensile straining, an ‘initial plateau’ was observed during the elastic loading of the bulk austenite in the gauge length. This effect became more prominent as peak power increased, which resulted in an increased width of the processed region within the gauge length. However during cyclic loading the ’initial plateau’ was not present after the first loading cycle and resulted in a larger permanent residual strain; hence, plastic deformation of the local material was suspected. Current results confirmed this by showing a local phase conversion from austenite to martensite induced by laser processing. Consequently, the tested tensile gauge length was in essence a hybrid that contained local martensite, where processing was conducted, and austenite from the unprocessed base material. It is believed that subsequent tensile loading would first induce detwinning of the local twinned martensite; followed by stress-induced martensite transformation (pseudoelastic) of the remaining gauge length. This is shown in Figure 5-12 which shows the effects of stress at different temperatures for Nitinol. The path of the processed metal would follow that of martensite and be detwinned during straining, whereas the original austenite gauge

length would transform into martensite. Hence, the previously observed yielding and larger permanent residual strain during cyclic loading can be attributed largely due to detwinning of the local martensitic region.

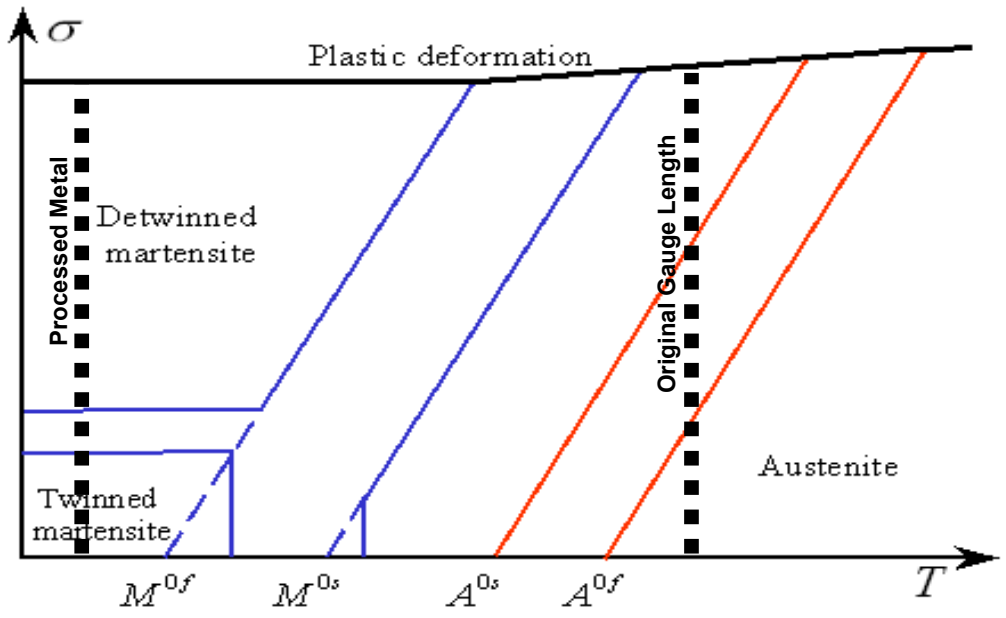

Figure 5-12: Schematic showing the effect of stress at different temperatures for Nitinol

5.7 Chapter Summary

This chapter analyzed the effects of laser processing on the transformation temperature of Nitinol. DSC results revealed additional high temperature transformation peaks that can be attributed to the local phase conversion induced by laser processing. These results were further corroborated with room temperature XRD analysis, showing only austenite in the base metal and added martensite peaks in the melted metal. TEM observations confirmed the presence of room temperature martensite within the processed/melted zone. Furthermore, the submicron particles were identified as Ti_2Ni. Finally, the results from this chapter pose the question: *what is the primary mechanism involved in altering transformation temperatures and can this phenomenon be controlled?*

6. MECHANISM RESPONSIBLE FOR ALTERED TRANSFORMATION

Modification to transformation temperatures induced by laser processing can greatly influence the functionality of Nitinol alloys. Depending on the application, these effects can either be beneficial or detrimental and as a result required to be controlled or even limited. For example, processing can be implemented in some applications to locally alter transformation behavior which can modify or even disable local pseudoelastic properties. In other applications, this reduction in strength may be undesired. Hence, the mechanism involved in altering transformation temperatures first needs to be identified. In this chapter the mechanisms responsible for changing transformation temperatures are investigated. In particular, process parameters were isolated and their effect on the solid-state diffusion-less transformation behavior was investigated using DSC analysis.

6.1 Effects of Process Parameters on Transformation Temperatures

The effects of pulse time, peak power and overlap on the transformation temperatures were individually investigated. In order to isolate the effects of process parameters, DSC test specimens were re-designed to limit the interaction of subsequent pulses. Figure 6-1 shows a schematic of the test sample which contained a space of about 20% of the spot diameter between each pulse. It is important to note that overlapping has similar effects as multiple pulses at the same location and can be mimicked accordingly. For example, 50% overlap is similar to 2 pulses at the same location, and 80% similar to 5 pulses. Table 3 details the parameters selected for analysis, which included pulse times up to 30ms, multiple pulses up to 15 times and low and high peak powers of 0.6kW and 0.9kW, respectively.

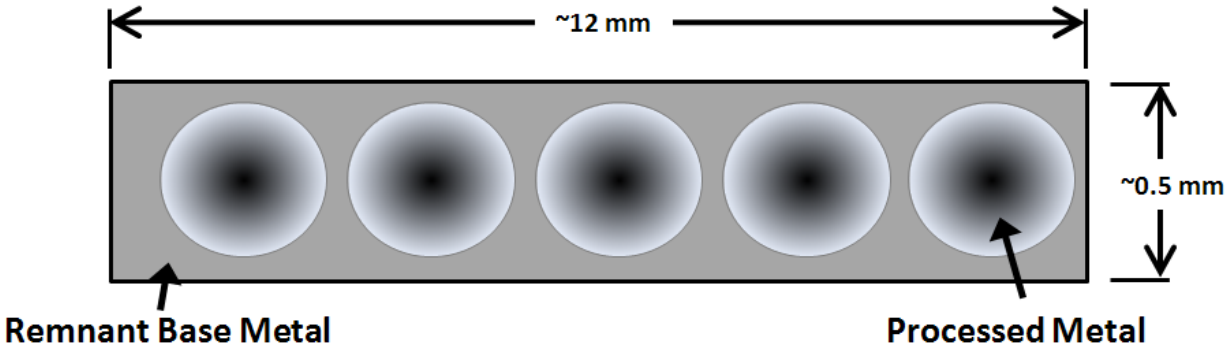

Figure 6-1: Schematic of laser processed DSC sample

Table 3: Select process parameters

Variable	Parameters
Pulse Time (ms)	1,2,3,4,5,10,15,25,30
Peak Power (kW)	0.6, 0.9 (full penetration)
No. of Pulses	1,2,3,5,7,10,15

Heating and cooling DSC traces for 0.6kw single pulse condition, with increasing pulse duration, are shown in Figure 6-2. Each trace clearly showed the transformation peaks of the unaffected base metal. However, very faint additional peaks became visible for the 1 ms pulse from the laser processed region. Increasing pulse duration further defined this new peak. It should be noted that increasing pulse time facilitates the growth of the molten region. In turn, DSC samples with longer pulse durations consisted of a larger sample size yielding more pronounced peaks. M_s temperatures extrapolated from DSC curves as a function of pulse time are shown in Figure 6-3. Interestingly, martensite start temperatures increased slightly with increasing pulse width.

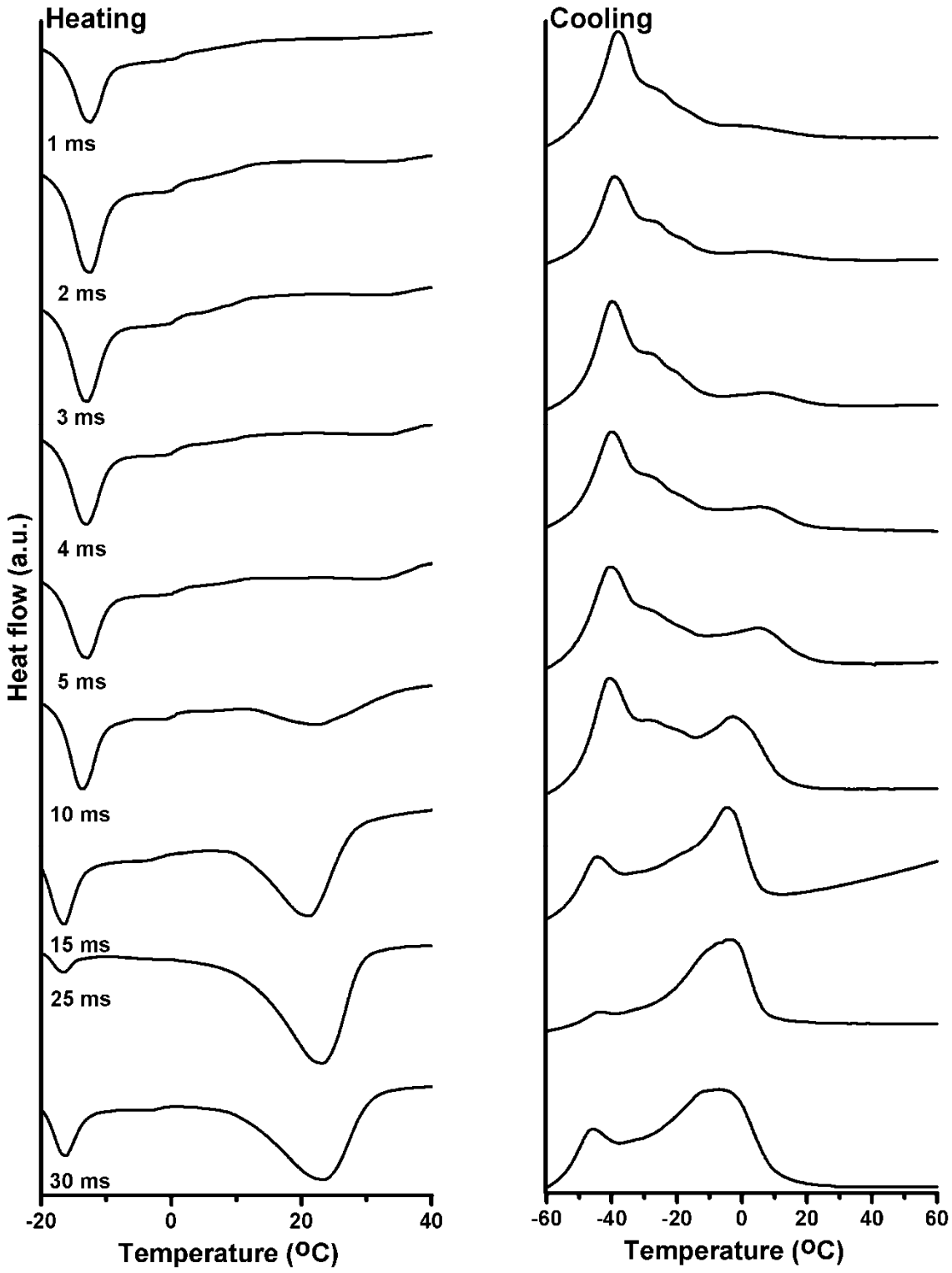

Figure 6-2: DSC plots of samples processed at 0.6kW with increasing pulse time

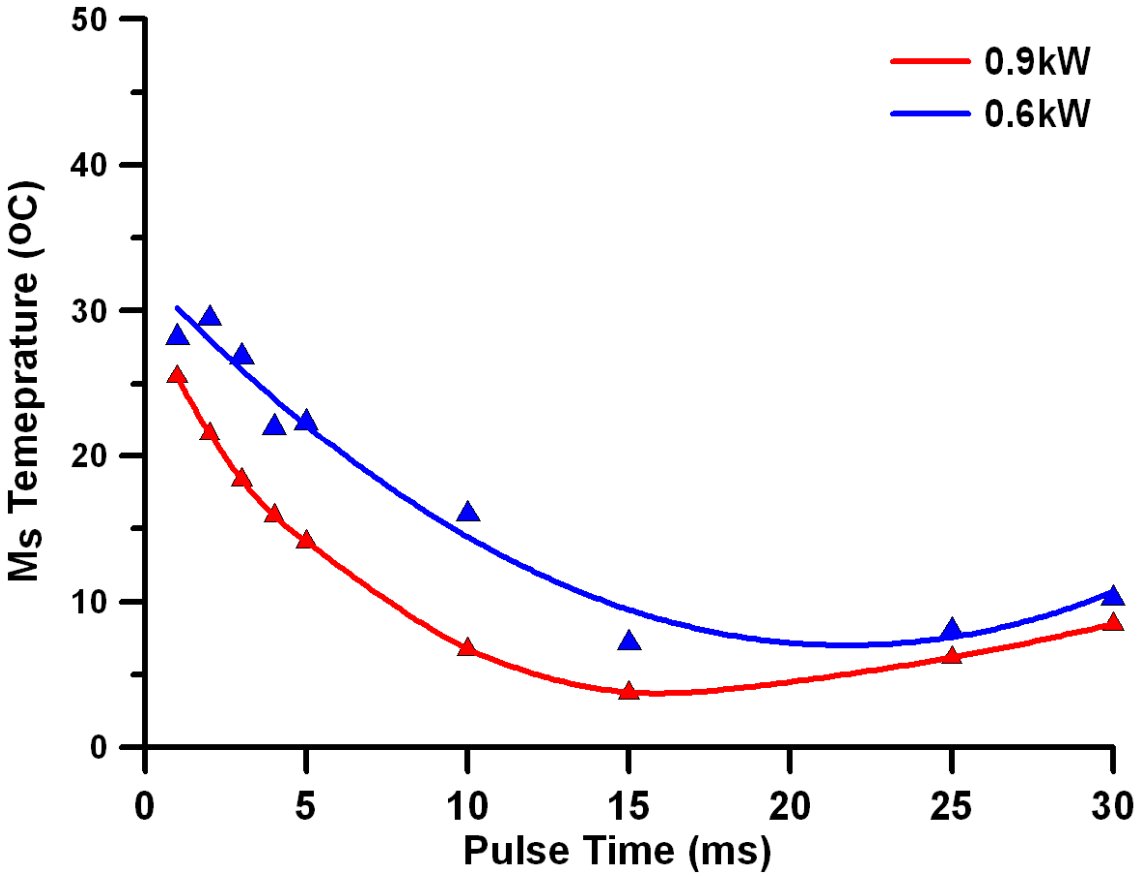

Figure 6-3: Martensite start temperature as a function of pulse time

The effects of the number of pulses on the transformation temperature for 0.6kW peak power and 3ms pulse width are shown in Figure 6-4. After the first pulse, a second peak emerged in DSC results with successive pulses inducing a shift towards higher Ms temperatures. Transformation peaks became increasingly sharp as temperatures approached 65^{o}C, with transformation beginning and ending within 10 degrees. Similar trends were observed when using a 30ms pulse width, as shown in Figure 6-5, although the peaks were more defined due to the larger processed region. Figure 6-6 summarizes the effects of additional pulses on the M_s temperatures for the 3 and 30ms pulse widths. Results showed the 30ms pulse to have consistently lower peak M_s temperature until 7 pulses were applied, beyond which it converged near 65^{o}C for both conditions.

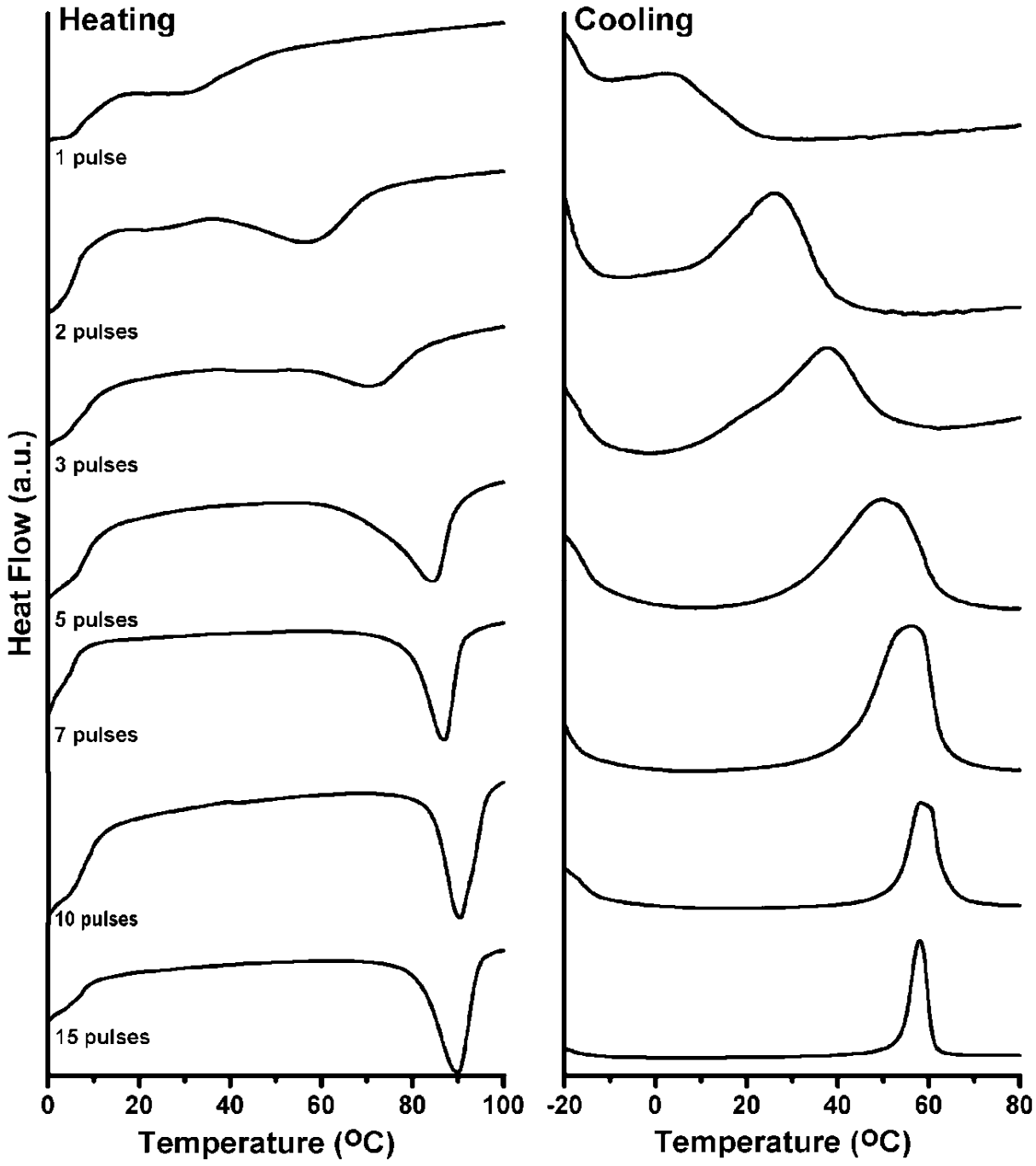

Figure 6-4: DSC plot of sample processed at 0.6kW and 3ms with increasing number of pulses

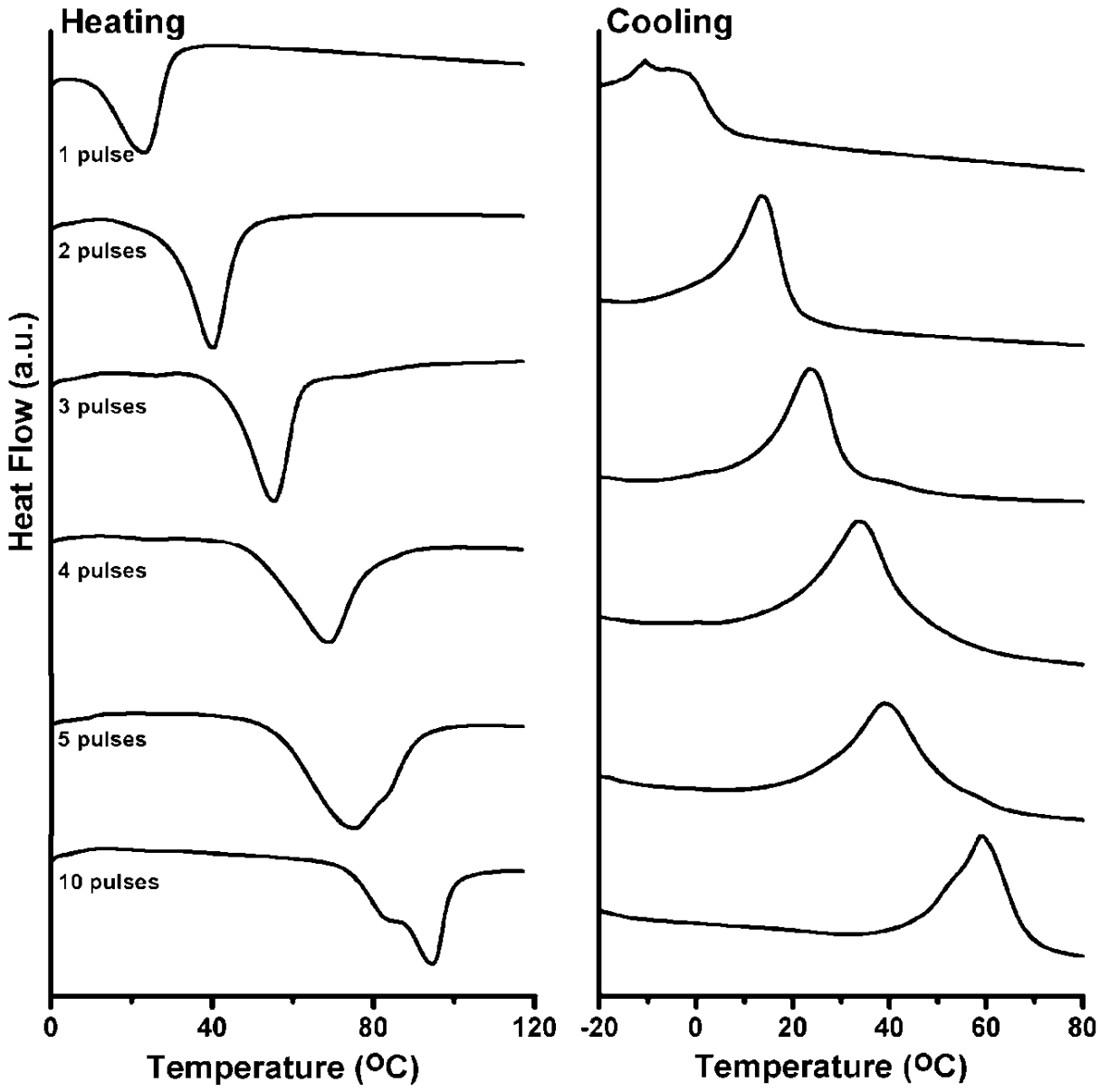

Figure 6-5: DSC plot of sample processed at 0.6kW with increasing number of pulses at 30ms

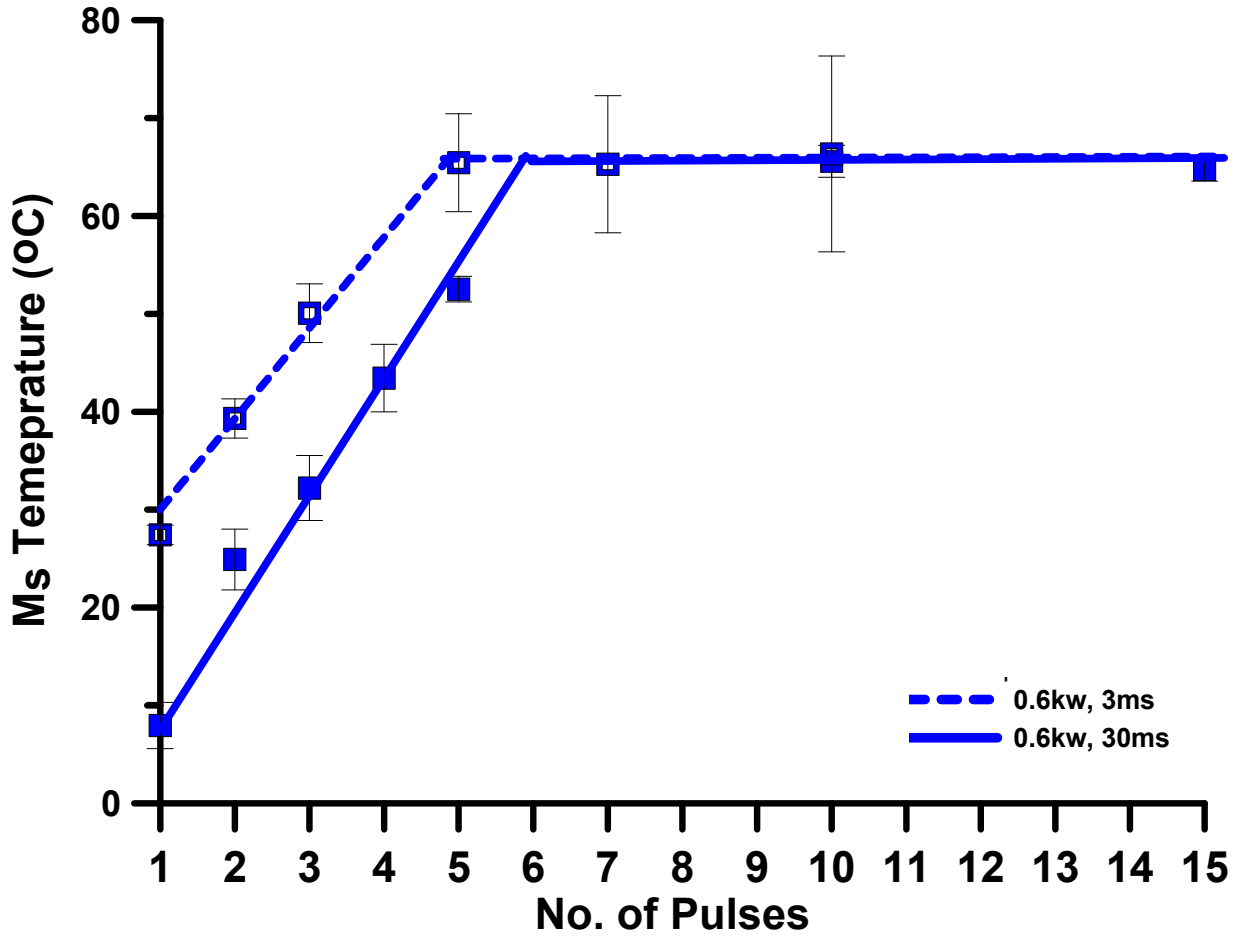

Figure 6-6: Effects of number of pulses on M_s Temperature

6.2 Factors Influencing Transformation Temperature

Current results showed a clear change in transformation temperature induced by laser processing. The next question posed was to determine the cause of these changes since one or more mechanisms may be responsible for altered M_s temperatures. The primary factors influencing the transformation temperature include metallurgical factors, which influence the elastic strain energy and frictional resistance of transformation, and chemical composition [72]. Metallurgical factors are more prominent in materials that have undergone thermo-mechanical processing. For example, the introduction of dislocations through mechanical deformation is known to lower M_s temperatures since dislocations impede transformation. However, in the current study these effects were minimized by subjecting the samples to annealing procedures prior to laser processing.

Hence, chemical composition is thought to play the greater role in altering transformation temperatures.

The effects of chemical composition on the transformation temperatures of Nitinol have been studied extensively [68,69,70,71]. Sensitivity to composition change has been shown to be severe in the nickel rich alloys, with changes of 1at. % altering the M_s temperature by as much as 250^{o}C [15]. Although some inconsistencies exist in prior studies [69-71], recent literature has consistently shown maximum M_s temperature for fully annealed NiTi alloys to reach about 65^{o}C when the Ni content is near or below 50% [72]. This relationship was shown in Figure 2-5c, which plots predicted and experimental transformation temperatures in Ti-rich alloys as a function of Ni content. It can be shown that transformation temperatures are independent of composition and remain near 65^{o}C as Ni content decreases. It is believed that this is because Ti is not soluble in NiTi beyond the equiatomic composition. Similarly, current results showed transformation temperatures increasing with application of laser processing and converging near 65^{o}C with increasing number of applied pulses (Figure 6-6). Hence, DSC analysis from laser processed samples correlated well with the effects of Ni loss in the overall composition.

Change in composition in Nitinol is commonly encountered during aging. Aging promotes the formation and growth of Ni-rich intermetallics (i.e. Ni_3Ti, Ni_3Ti_4), which in turn alters the matrix Ni-Ti ratio (lowering Ni content in the matrix). This results in a rise in transformation temperature, as expected from the change in composition shown in Figure 2-5c. Furthermore it has been shown that after prolonged aging the matrix Ni content can reach near-equiatomic and bring M_s temperatures near 65^{o}C. However, from TEM observations in the the current work the formation of Ni-rich intermetallics in the structure was not observed. Therefore, it was speculated that the composition change was facilitated by a different mechanism which completely removed the nickel from the material. In particular, the occurrence of local vaporization was suspected.

6.3 Influence of Vaporization on Composition Change

Heat generated during laser processing can cause peak temperatures to surpass the liquidus temperature of an alloy, inducing local melting [31]. Laser power densities have also been shown to increase surface temperatures in the molten region to or beyond the boiling point [73,74]. Local vaporization forms a vapor cavity known as the keyhole, a schematic of which is shown in Figure 6-7. In pulsed laser processing, keyhole formation is transient and dynamic. During the application of laser beam energy, the keyhole nucleates and grows by pushing the molten metal out of the cavity along the outer circumference. Upon termination of the laser beam energy, the molten metal flows back, effectively refilling the cavity. Subsequent cooling induces rapid solidification of the molten metal and the formation of the final microstructure. Laser melting often causes the destruction of the base metal microstructure and as a consequence modification to its inherent mechanical properties. The rapid cooling rates associated with the pulsed Nd:YAG process also contribute to the type of solidification experienced.

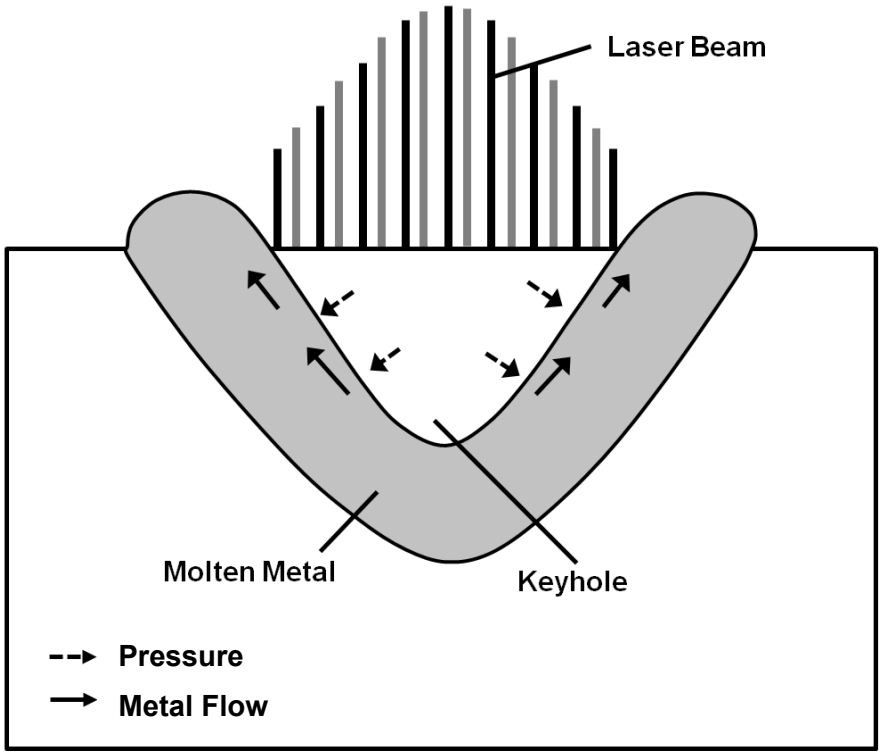

Figure 6-7: Schematic of keyhole formation

The relative loss of elemental constituents due to vaporization during laser processing can be estimated by their respective vapor pressures. The equilibrium pressure of each alloying element is related to the equilibrium temperature and can be calculated using the following equation:

$$log_{10}(p) = A + \frac{B}{T} + Clog_{10}(T) + DT + ET^2$$

where A,B,C,D and E are constant coefficients which usually differ for the various elements and T refers to the temperature. The corresponding coefficients for nickel and titanium are shown in Table 4. Figure 6-8 illustrates the vapor pressures as a function of temperature for nickel and titanium. They clearly deviate for the two elements with nickel requiring higher pressure to maintain an equilibrium state at any temperature. Although peak temperatures will reach high enough that both elements will vaporize, nickel's vaporization rate will be higher than that of titanium.

Table 4: Constant coefficients for calculation of equilibrium vapor pressure of Ni and Ti [75]

	A	B	C	D	E
Ni	-214.3	-3519	74.94	-0.018	15.1E-7
Ti	16.37	-25229	-2.6574	0	0

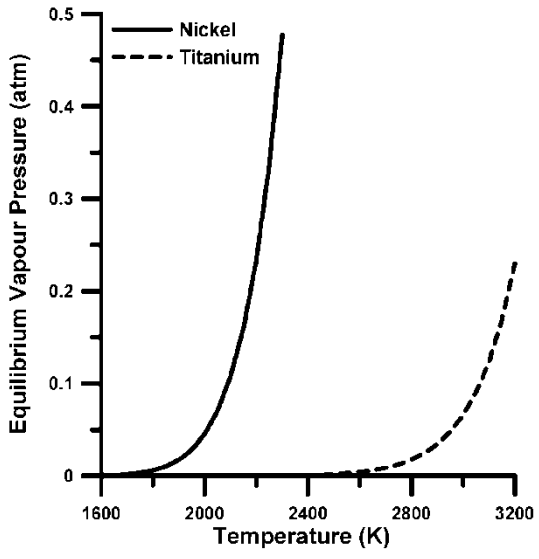

Figure 6-8: Equilibrium vapor pressure as a function of temperature for nickel and yitanium

Inherent challenges exist in obtaining an accurate local compositional analysis in the relatively small processed area obtained in the current study. Although it may be difficult to attain reliable quantitative data, the relative loss may be detected using several methods. In order to detect the loss of nickel, an experiment was carried out to analyze the vaporized constituents. A portion of the vaporized material was captured as condensate in a hollow quartz tube. Figure 6-9 shows the experimental set-up where a tube was mounted coaxial to the laser to insure no disruption of the beam convergence. Nearly 50 pulses were conducted in order to attain a sufficient amount of deposition for analysis. After processing, the quartz tube was fractured and the deposited constituents were analyzed using Energy Dispersive Spectroscopy (EDS). This experiment confirmed the preferential loss of nickel by analyzing the vapor constituents captured inside a quartz tube. Table 5 shows the EDS results, which identified three elements including vaporized nickel and titanium, while Si was also detected from the SiO_2 quartz tube. The relative atomic % of nickel was three times that of titanium.

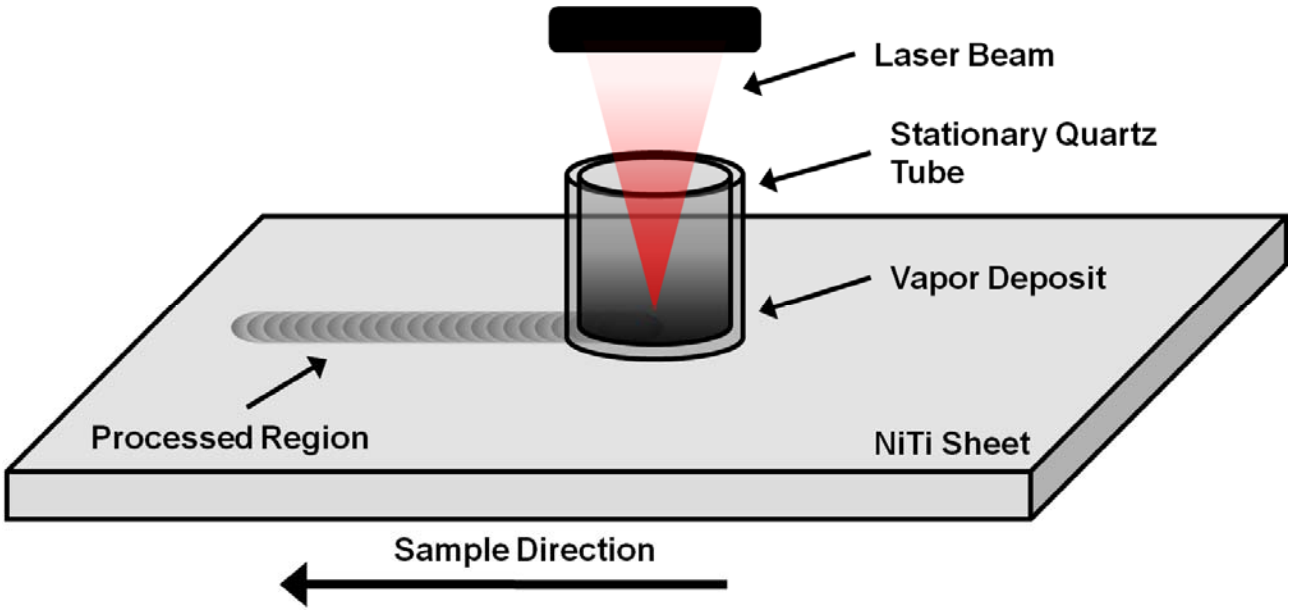

Figure 6-9: Schematic showing nickel capture

Table 5: Composition of vaporized constituents in quartz tube

Element	Composition (at. %)
Ti	24.49
Ni	75.51

Nickel depletion in the processed region was also detectable using EDS composition analysis. A line scan including the base metal and processed region is shown in Figure 6-10. Although EDS techniques are unable to determine an accurate composition, the relative difference in composition was clearly visible. EDS-estimated average nickel content for the base material (50.07 at. % ±0.53) was clearly higher when compared to the processed material (48.36 at. % ±0.84).Therefore, preferential vaporization of Ni in the binary NiTi system was confirmed to be the mechanism inducing higher transformation temperatures.

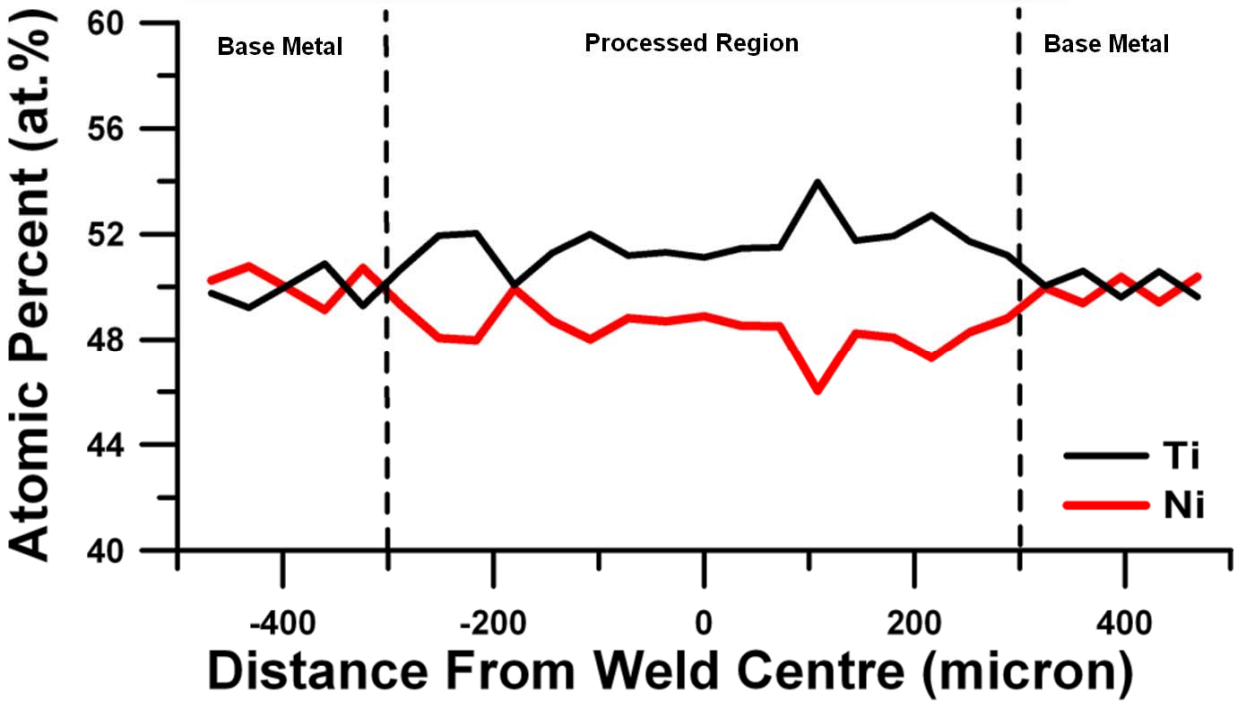

Figure 6-10: EDS line scan across processed region

6.4 Effects of Composition Change on Phase Microstructure

The effects of changing composition (becoming more Ti-rich) on the microstructure can be predicted by examining the partial binary Ni-Ti phase diagram near the equiatomic region, as shown in Figure 6-11. Two distinct eutectic temperatures are present at 1116^{o}C and 984^{o}C in the Ni and Ti-rich domains, respectively. The cooling path labeled C_o represents the original bulk composition of the alloy (nearly 50.7 at. %). Cooling from C_o, results in nearly instantaneous solidification due to the narrow solidus-liquidus gap. As the composition becomes more titanium rich, the solidification range decreases until a congruent solidification is attained at the equiatomic composition (C_1). Further decrease in Ni from C_1 to C_2 results in a drastic increase in solidification range (from 0 to about 300°C) until the eutectic transformation occurs at 984^{o}C. Compositions with Ni contents below C_2 stabilize into a dual-phase structure which includes NiTi and Ti_2Ni below the eutectic temperature. The aforementioned dynamics of solidification will result from equilibrium cooling condition; however, during laser processing rapid solidification can result in changes to the inherent structure.

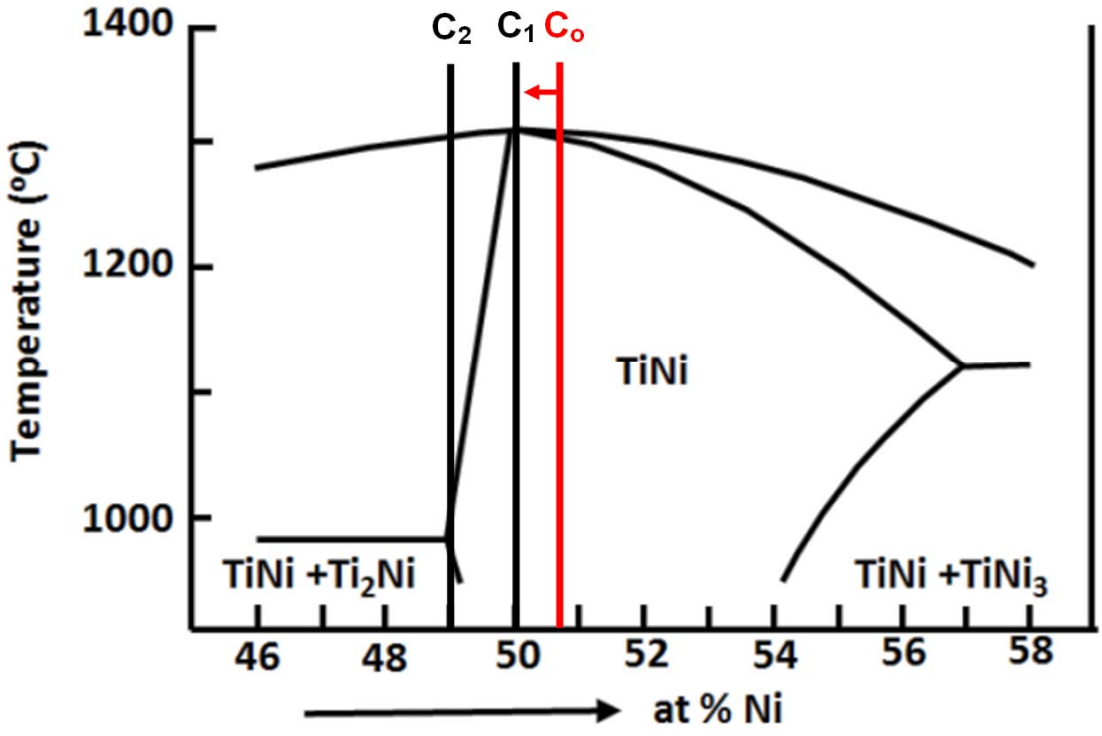

Figure 6-11: Partial-binary NiTi phase diagram

Rapid solidification in a non-congruent binary system can induce segregation of saturated constituents and solidification cracking. The lack of time for diffusion and incomplete mixing play important roles in solute redistribution. The solute will be pushed along with the solidification front with the final liquid to solidify being solute rich. This local area then stabilizes into a solute rich intermetallic (i.e. Ti_2Ni). Although the overall composition of the re-solidified metal is similar to the prior liquid (including matrix and intermetallics) the chemistry of the matrix material will be different. Solute redistribution plays an important role in solidification cracking as it affects the solidification temperature range and amount of terminal liquid.

Effects of the aforementioned phenomena were observed metallographically, as shown in Figure 6-12 for 0.6kw pulse power, 3ms pulse time. Recalling from Figure 6-6, each additional pulse resulted in increased transformation temperatures due to the reduced nickel content. After the first pulse only slight changes to the re-melted region were observed and the microstructure had not drastically changed. Further reduction in nickel content induced by additional pulses (Figure 6-12 b and c) resulted in the formation of Ti_2Ni intermetallics. After 10 pulses the expected concentration was well within the titanium rich domain (i.e. C_2 in Figure 6-11) with a large solidification range making it susceptible to solidification cracking and eutectic reaction. This was confirmed metallographically in Figure 6-12d where solidification cracking was observed within the re-melted region. Furthermore the large solidification range and rapid cooling promoted segregation of titanium along the solidification front, which led to excess production of Ti_2Ni intermetallic. This is shown in Figure 5-10 where Ti_2Ni particles were seen to be aligned within a twinned martensite matrix. It should also be noted that these results emphasize that care is required when laser processing NiTi alloys, since excess processing can induce solidification cracking.

The effect of pulse time was shown to be less prominent than the number of pulses applied. This is consistent with results of a study conducted by Jandaghi et al. who analyzed composition change in stainless steel induced by a pulsed Nd:YAG laser and correlated results to a hydrodynamic physical model [76]. It was observed that during a single pulse, the rate of vaporization decreased with pulse time and increased pool

volume. In other words, the composition change is primarily experienced during the first few moments of lasing, after which there is a decrease in the rate of loss. Furthermore, the pool volume increases and subsequently dilutes the amount of element loss. Hence increased pulse time would decrease the change in M_s temperature, as observed in Figure 6-3. This can also explain increased nickel loss and increase in M_s temperature with the application of multiple pulses.

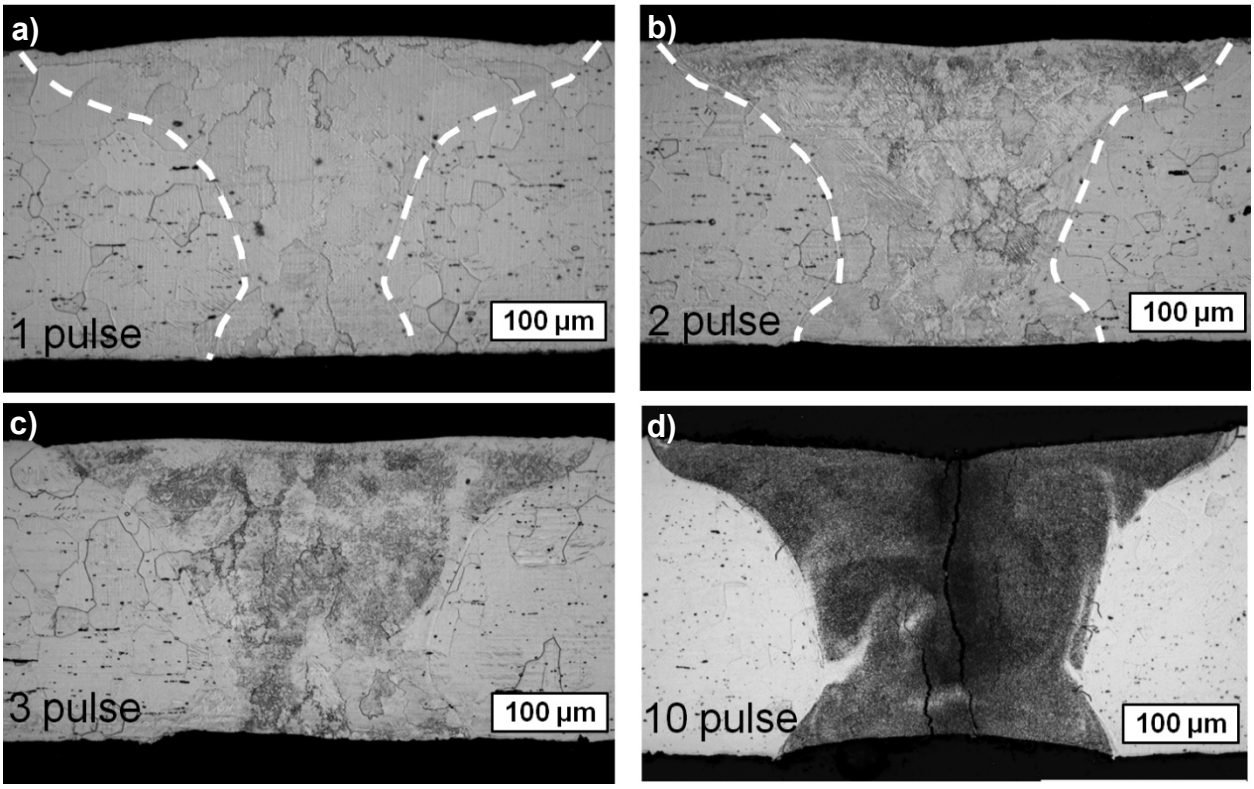

Figure 6-12: Effects of multiple pulses on microstructure

6.6 Chapter Summary

This chapter detailed the factors influencing the local modification of transformation temperatures. The effects of pulse time and peak power were not as prominent as multiple pulses. Furthermore, the change in local composition was determined to be the primary mechanical involved in altering local transformation temperatures. The occurrence of preferential local vaporization of nickel played a key role in the local change in transformation properties. Excess vaporization resulted in the local composition becoming titanium rich, which promoted the formation of Ti_2Ni

intermetallics. Finally, these factors need to be considered in the design and fabrication of devices implementing laser processed Nitinol.

7. DEMONSTRATION OF ALTERED TRANSFORMATION TEMPERATURE

Shape memory effects in shape memory alloys occur primarily due to the solid-state diffusionless transformation from austenite to martensite. In a monolithic SMA this typically happens simultaneously throughout the material, giving it a single shape memory. However, by locally altering transformation temperatures, multiple memories can be embedded into a monolithic object. This can be achieved by using laser process methods described in the current work. A schematic describing the effects of laser processing on either sheet or wire forms is shown in Figure 7-1. The color of each local area corresponds with the respective transformation behavior. Consequently a new technology has been developed which enables multiple memories to be embedded in a monolithic sheet. This technology has been informally referred to as Multi-Memory Material Technology. The current chapter describes several actual demonstrations and acts to provide a proof of principle of this technology.

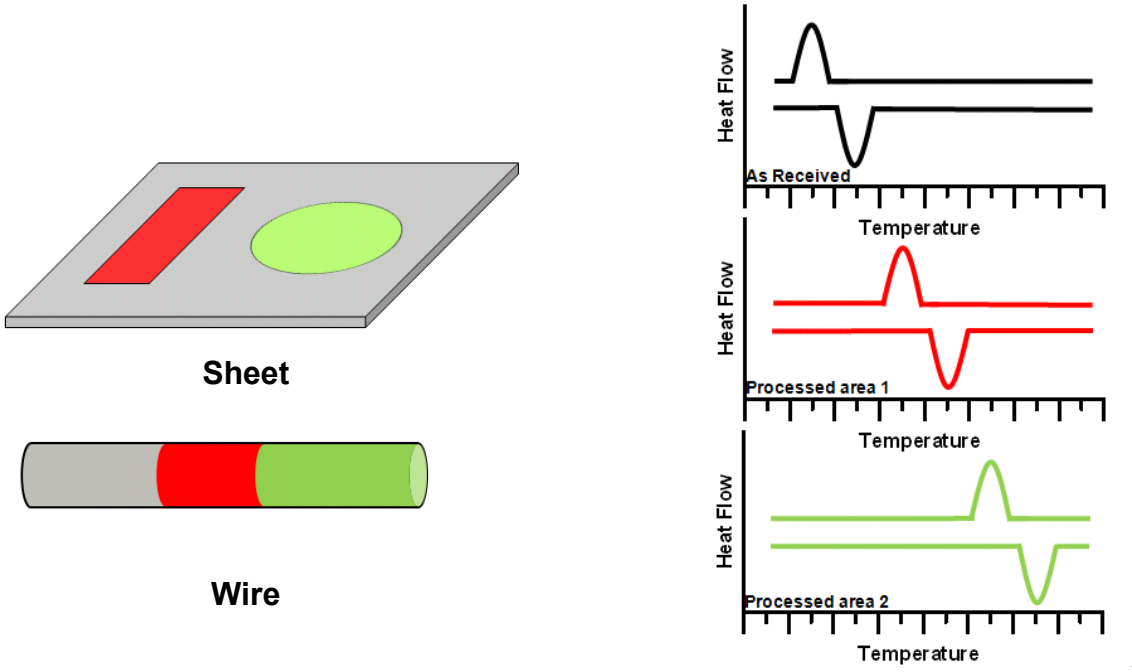

Figure 7-1: Schematic of locally altered transformation temperatures

7.1 Multi-Memory Wire

An attempt was made to demonstrate the local alteration of transformation temperatures by embedding multiple memories in a monolithic strip. A schematic showing the effects of laser processing is shown in Figure 7-2. The previously heat treated bulk material exhibited a single set of transformation temperatures (single memory) similar to most commercially available shape memory alloys. By locally vaporizing nickel using a pulsed Nd:YAG laser, transformation temperatures at four distinct sites were altered, while the untreated regions remained unchanged. Therefore, additional memories were effectively embedded in a monolithic sheet.

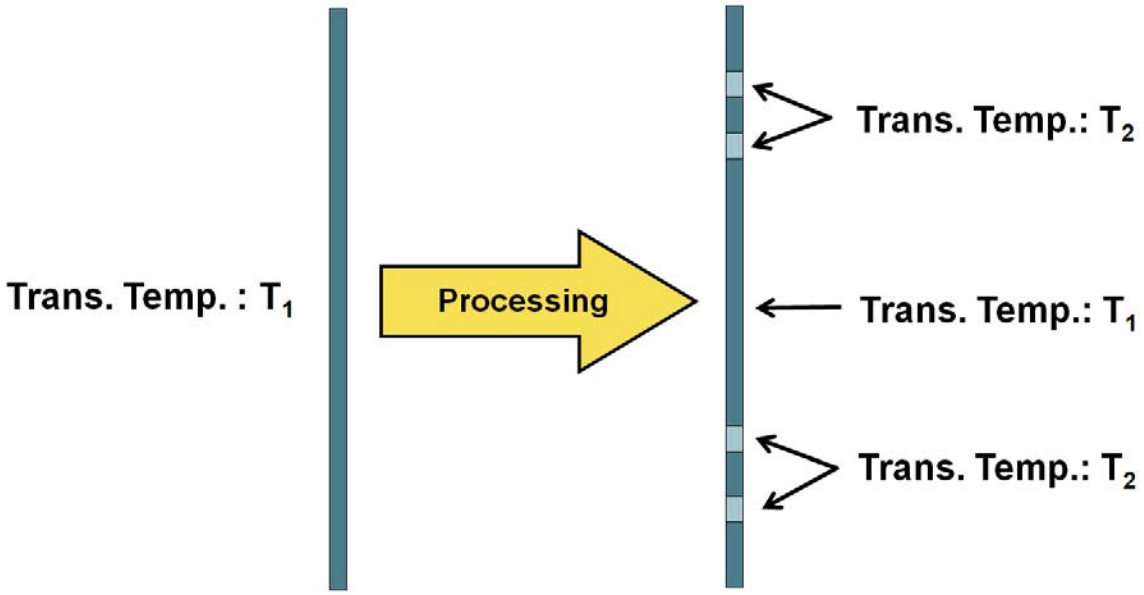

Figure 7-2: Schematic of embedding additional transformation temperature (T2) regions in a Nitinol strip with transformation temperature (T1)

A demonstration of the actual sample and a schematic with increasing temperature is shown in Figure 7-3. At low temperatures the entire sample is in the martensitic phase and easily deformed into a 'C' shape. Upon heating to a temperature greater than T_1, the bulk unprocessed material transforms to austenite and recovers its original shape, while the processed regions remain in the martensite phase. Further heating to above T_2 induces the transformation of the processed regions to austenite and the formation of a second memory (completely straight). Therefore, multiple memories can be embedded by locally vaporizing elemental constituents using high power densities.

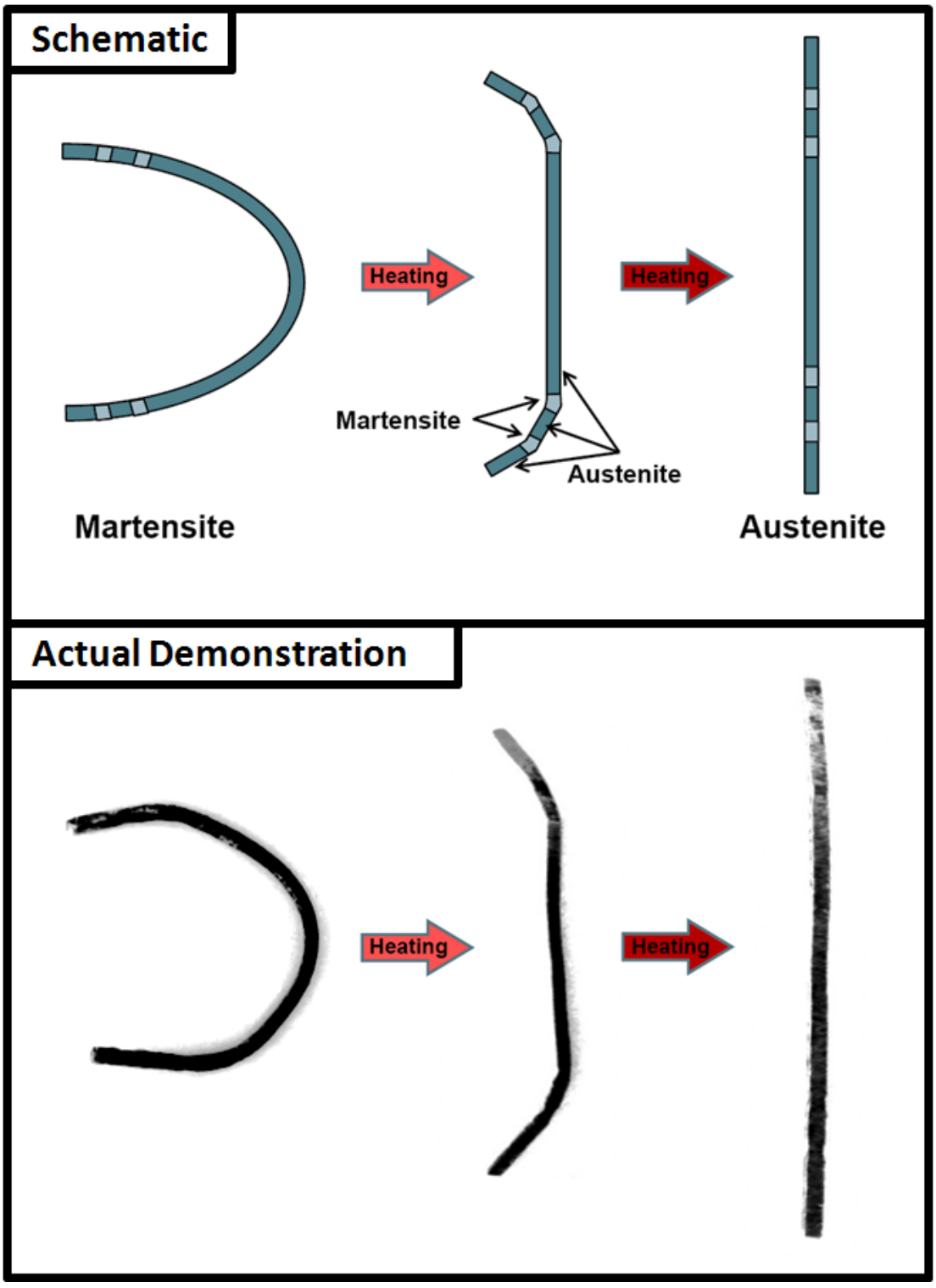

Figure 7-3: Demonstration of multiple memories embedded in a Nitinol alloy

7.2 SMA Diaphragm

Figure 7-4 shows a schematic and actual prototype of a SMA diaphragm that has only been able to be realized by altering local transformation temperatures. In this example, the central area has been treated to have a transformation temperature above room temperature whereas the outer supporting frame transforms below room temperature. Multiple transformation temperatures are important in this situation. This allows the central area to be deformed separately at room temperature since it is in the martensite state, whereas the supporting frame maintains its relatively rigid shape. Such a device can be easily implemented in temperature-induced volume compensation or even pressure biasing for which many polymer diaphragms are already in use.

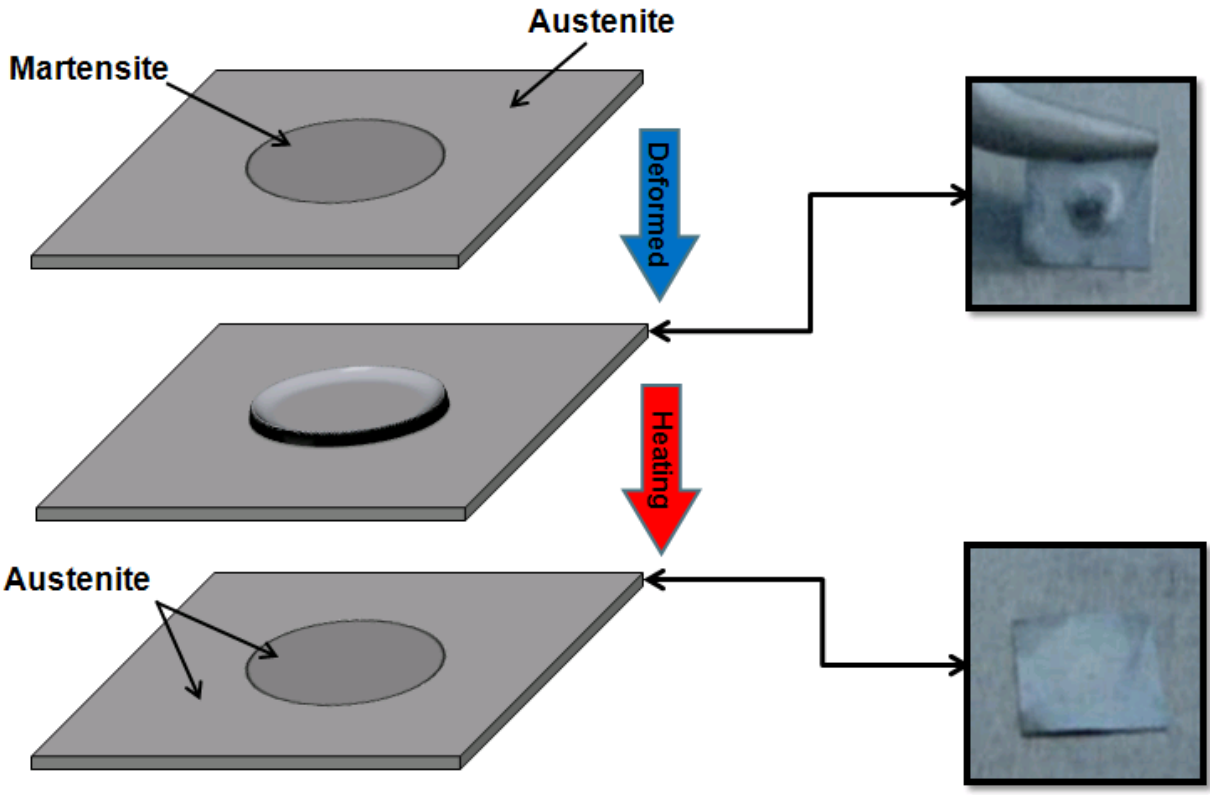

Figure 7-4: Schematic and actual image of SMA diaphragm

7.3 Hybrid SMA Actuator

Figure 7-5 illustrates a potential application of the differing transformation temperatures for an actuator device. This design was published by Toews and Gorbet in 2006 and utilized two different SMA compositions in its creation [77]. In this example, a central arm of a three-armed actuator device can be treated to have a differing transformation temperature than the outer arms. The central arm can subsequently be shape-set out-of-plane from the outer two arms. These altered local transformation temperatures coupled with the differing shape-set enables the creation of a self-biasing two-stage actuator. An actual monolithic design was successfully created by Cluff et al. in 2009 [78] using powder metallurgy to sinter differing Ni compositions which was followed by a shape setting procedure. It was reported to have a tip deflection of 3%-4% of its length.

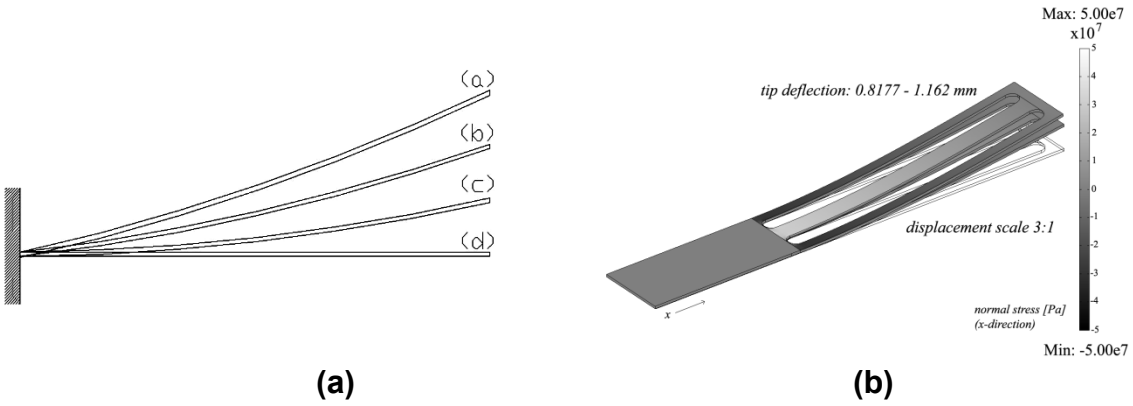

Figure 7-5: Schematic of (a) conceptual actuator operation showing (b) out-of-plane tip displacement [77]

Similarly, an actual hybrid actuator was designed and fabricated by implementing local vaporization of nickel. Figure 7-6 shows the heating and cooling cycle of the 12mm long actuator. In the cold state, the pseudoelastic outer arms pull the martenstic central arm downwards. Upon heating, the central arm transforms from martensite to austenite and counteracts the force of the outer arms, pulling the actuator up. Cooling back down reverses the transformation of the central arm and the actuator deflects back. A total deflection of 3mm was experienced during each thermal cycle, which translates to about 25% deflection. This was consistent for all tested cycles (at least 20 cycles were carried

out). Finally, this design finds many applications, such as microelectromechanical (MEMS) and valve devices.

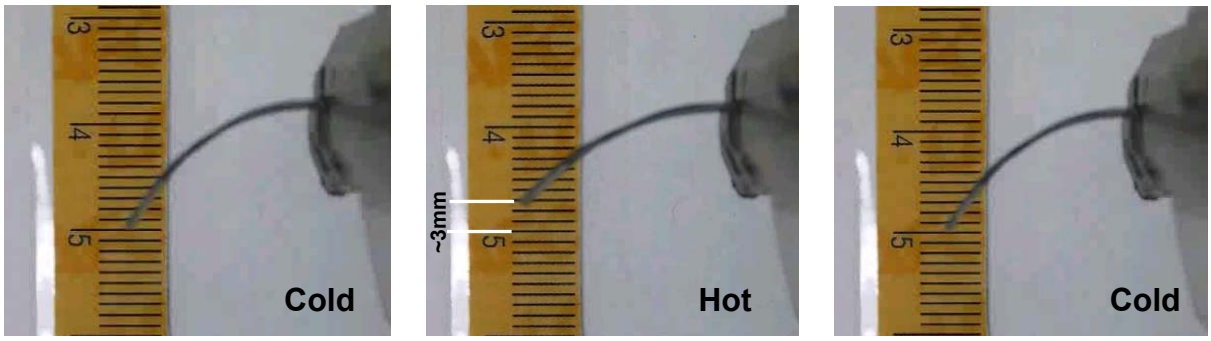

Figure 7-6: Actual hybrid actuator created by local vaporization

7.4 Chapter Summary

In this chapter the potential for altered transformation temperatures was demonstrated by creating actual working prototypes. First, a two-memory wire was demonstrated that showed an additional transformation temperature besides that of the original base metal. The second prototype was a SMA diaphragm designed to have a soft central region and rigid outer frame. The final example of a monolithic actuator having 25% deflection was also demonstrated. All of the aforementioned devices demonstrate the enabling quality of local vaporization induced by laser processing. From this work, a patent has been filed with the United Stated Patent Office (USPTO) in regard to altering local transformation temperatures. [79]

8. CONCLUSIONS AND OUTLOOK

The current thesis has detailed the effects of pulsed Nd:YAG laser processing on the binary Nitinol alloy. More specifically, the effects on mechanical performance, microstructure and phase transformation temperatures were analyzed. The following sections contain the conclusions of this work and recommendations for future research.

8.1 Conclusions

The conclusions are grouped in accordance to the research objectives in section 1.2

8.1.1 Mechanical Performance

1) Processing parameters (energy input and welding speed) were shown to strongly influence the mechanical properties (tensile strength and ductility) of the laser processed Nitinol alloy. Higher energy input and lower speed resulted in improved mechanical performance.
2) Local yielding was observed in laser processed specimens during tensile loading. Two deformation mechanisms occurred during tensile loading of the transverse tensile coupons (processed and base metal). This became more pronounced with increasing peak power.
3) Laser processed samples exhibited higher permanent residual strain and exhibited slightly higher efficiency for energy storage during the initial 5 cycles as compared to the base material.
4) Fracture surfaces of base material revealed ductile dimpled surfaces. Laser processed specimens exhibited both brittle (low peak power) and ductile (high peak power) failure modes with traces of submicron particles on the fracture surface.

8.1.2 Microstructure and Solid-state Phase Transformation

1) Microstructure observations revealed large austenite grains in the annealed base material and columnar dendritic growth along the re-solidified boundary. Varying amounts of segregation within the process material corresponded with mechanical performance (higher segregation exhibited lower strength).
2) DSC results revealed additional high temperature transformation peaks that can be attributed to the local phase conversion induced by laser processing.
3) Room temperature XRD analysis corroborated DSC results, showing only austenite in the base metal and added martensite peaks in the processed metal.
4) Temperature controlled TEM observations confirmed the high temperature peaks seen in DSC results were produced from the processed regions. The room temperature martensite in the material transformed into austenite upon heating above 100^{o}C.

8.1.3 Mechanisms Altering Functional Properties

1) Application of lasers on Nitinol induced local vaporization of both Ni and Ti; however preferential vaporization of nickel occurred. In turn, this resulted in a change of local chemistry.
2) The effects of nickel loss resulted in an increase in transformation temperature with M_s temperature reaching a maximum of 65^{o}C. This correlated well with existing literature detailing the effects of chemistry on the transformation temperature.
3) The formation of submicron Ti_2Ni particles was observed as the local chemistry became increasingly titanium rich. Furthermore, Ti-solute segregation due to rapid solidification was also observed with the terminal liquid stabilizing into Ti_2Ni particles.
4) Excess loss of Ni can push the local chemistry towards the Ti-rich region of the Ni-Ti phase diagram where a large freezing range is experienced. This increases the susceptibility of crack formation, which was observed.
5) A novel method has been developed that can be applied to alter local chemistry, and hence the transformation temperature of shape memory alloys by using a

high power density energy source. A proof-of-concept was successfully demonstrated where current results were used to embed an additional memory into a monolithic Nitinol alloy.

8.2 Outlook

The following topics are suggested for future research:

1) Although the current thesis discovers and details the effects of local vaporization on the transformation temperature of Nitinol, other properties may also be affected. For example, the tenacious oxide layer of Nitinol alloys makes them ideal for medical device applications. By altering the local chemistry and making it more titanium rich, the corrosion performance could be enhanced (due to higher affinity of titanium to oxide). As such, further research on the corrosion performance effects of laser processing on Nitinol is recommended.
2) At temperatures above A_f in the processed region, pseudoelastic behaviour may occur, resulting in the changes to the stress strain behaviour. However, this still needs to be tested using temperature controlled tensile equipment. It is suggested that experimental and finite element method (FEM) studies be carried out to further detail the effects at different temperatures.
3) A numerical model $corr_{el}$ating the process parameters to the vaporization flux can aid in more precisely controlling and predicting transformation temperatures. It is suggested that further quantitative studies be carried out to enhance an understanding of the effects of process parameters on local vaporization.
4) Finally, a more complicated ternary system (or multi-composition) can be envisioned by selectively vaporizing constituents having a lower vapor pressure. Similarly, mixing of additional alloying elements can also be achieved, leading to a ternary or a more complex local system. In this case selected alloys may be added in local regions using consumable material (i.e. thin foil, powder etc.). Further research on other alloys to further enhance an understanding of the possibilities, is recommended.

REFERENCES

1. Lin, H.C., Wu, S.K., “Tensile behavior of a cold-rolled and reverse-transformed equiatomic TiNi alloy,” *Acta Metallurgica et Materialia*, v 42, n 5, 1994, pp 1623-1630.

2. Falvo, A., Furgiuele, F.M., Maletta, C., "Laser welding of a NiTi alloy: Mechanical and shape memory behavior," *Materials Science & Engineering A*, v 412, n 1-2, 2005, pp 235-240.

3. Chau, E.T.F, Friend, C.M., Allen, D.M., Hora, J., Webster, J.R., "A technical and economic appraisal of shape memory alloys for aerospace applications," *Materials Science and Engineering A*, v 438–440, 2006, pp 589–592.

4. Shabalovskaya, S.A., "Biological aspects of TiNi alloy surfaces," *Proceeding of ICOMAT*, 1995, pp 1199-1204.

5. Yan, X.J., Yang, D.Z., Qi, M. “Rotating–bending fatigue of a laser-welded superelastic NiTi alloy wire,” *Material Characterization*, v 57, 2006, pp 58-63.

6. American Society of Testing and Materials Standard F2004, "Standard Test Method for Transformation Temperature of Nickel-titanium Alloys by Thermal Analysis," West Conshohocken, PA, 2005.

7. American Society of Testing and Materials Standard F2005, " Standard Terminology for Nickel-Titanium Shape Memory Alloys," West Conshohocken, PA, 2010.

8. American Society of Testing and Materials Standard F2063, "Standard Specification for Wrought Nickel-Titanium Shape Memory Alloys for Medical Devices and Surgical Implants," West Conshohocken, PA, 2005.

9. American Society of Testing and Materials Standard F2082, "Standard Test Method for Determination of Transformation Temperature of Nickel-Titanium Shape Memory Alloys by Bend and Free Recovery," West Conshohocken, PA, 2006.

10. American Society of Testing and Materials Standard F2129, "Conducting Cyclic Potentiodynamic Polarization Measurements to Determine the Corrosion Susceptibility of Small Implant Devices" West Conshohocken, PA, 2008.

11. Buehler, W. J., Gilfrich, J. V., Wiley, R. C., "Effect of Low Temperature Phase Changes on the Mechanical Properties of Alloys near Composition TiNi, " *Journal of Applied Physics*, v 34, n 5, 1963, pp 1475-1478.

12. Chang, LC, Read, TA. “Plastic deformation and diffusion- less phase changes in metals - the gold-cadmium beta phase,” *Trans AIME*, 1951, pp 47-52.

13. Basinski, Z. S., Christian, J.W., “Crystallography of deformation by twin boundary movements in indium-thallium alloys,” *Acta Metallurgica*, v 2, n 1, 1954, pp 101-113.

14. Kauffman, G. B., Mayo, I., “The story of Nitinol: The serendipitous discovery of the memory metal and its applications,” *The Chemical Educator*, n2, v2, 1997, pp 1-21.

15. Ren, X., Otsuka, K., “Why does the martensitic transformation temperature strongly depend on composition?,” *Materials Science Forum,* v 327, 2000, pp 429-432.

16. Hawkins, T., *Metals Handbook*, Vol. 8, American Society for Metals, Metals Park, OH, 8th edn., 1973, pp 326.

17.Duerig, T. W., *Engineering aspects of shape memory alloys,* Butterworth-Heinemann, Oxford, 1990.

18. Tang, W., “Thermodynamic study of the low-temperature phase B19′ and the martensitic transformation in near-equiatomic Ti-Ni shape memory alloys,” *Metallurgical and Materials Transactions A*, v 28, n 3, v 8, pp 537-544.

19. Van Humbeeck, J., “Shape memory alloys: a material and a technology,” *Advanced Engineering Materials*, v 3, n 11, 2001, pp 837-850.

20. Porter, D. A., Easterling, K.E., *Phase Transformations in Metals and Alloys*, CRC press, USA, 1992.

21. Robert E. Reed-Hill, Reza Abbaschian, *Physical Metallurgy Principles: Third Edition*, PWS Publishing Company, Boston, USA, 1994.

22. Oulu Univeristy Library, *Biocompatibility evaluation of nickel-titanium shape memory metal alloy*, http://herkules.oulu.fi/isbn9514252217/html/x317.html (visited April 29, 2009).

23. Otsuka, K., Ren, X. "Physical metallurgy of Ti–Ni-based shape memory alloys," *Progress in Materials Science*, v 50, n 5, 2005, pp 511-678.

24. Nishida, M., Wayman, CM., Honma, T., “Precipitation processes in near equiatomic TiNi shape memory alloys,” Metallurgical Transaction A, v 17A, 1986, pp 1505.

25. Massalski, T.B., Okamoto, H., Subramanian, P.R., Kacprzak, L., *Binary alloy phase diagrams*, 2nd edition, v 3, ASM International, Materials Park OH, 1990. pp 2874.

26. Russell, S. M., “Nitinol Melting and Fabrication,” SMST-2000: The Inter. Conf. on Shape Memory and Superelastic Technologies, Pacific Grove, CA, USA; 2000.

27. Miller, D. A., Lagoudas, D. C., “Influence of cold work and heat treatment on the shape memory effect and plastic strain development of NiTi,“ *Materials Science and Engineering A*, v 308, 2001, pp 161-175.

28. Matsumoto, H. “Transformation behaviour of NiTi in relation to thermal cycling and deformation,“ *Physica B*, v 190, 1993, pp 115-120.

29. Zheng, Y., Jiang, F., Li, L., Yang, H., Liu, Y. “Effect of ageing treatment on the transformation behaviour of Ti-50.9 at.% Ni alloy,“ *Acta Materialia*, v 56, 2008, pp 736-745.

30. Otsuka, K., Ren, X., “Physical metallurgy of Ti-Ni-based shape memory alloys,” *Progress in Materials Science*, v 50, 2005, pp 511-678.

31. Duley, W.W., *Laser Welding*. John Wiley and Sons Inc., Toronto, 1999.

32. Siegman, A.E., *Lasers*, University Science Books, California, 1986.

33. Ready, J.F., *Effects of High Power Laser Radiation*, Academic Press, New York, 1971.

34. Zhou, Y., *Microjoining and Nanojoining*, Woodhead Publishing Ltd., Cambridge, England, 2008.

35. Dawes, C., Laser Welding, McGraw-Hill, New York, 1992.

36. Crafer, R. C., Oakley, P. J., *Laser Processing in Manufacturing*, Chapman and Hall, New York, 1993.

37. Charschan, S.S., *Laser in Industry*. Van Nostrand Reinhold Company, New York, 1972.

38. Elliot, B. *Weldability of Plated thin sheet and Cu by Pulsed Nd:YAG Laser welding*, MASc thesis, Univeristy of Waterloo, Canada, 2002.

39. Marley, C., “A guide to welding with low-power YAG lasers,” *Welding Journal*, v 75, n 11, 1996, pp 47-50.

40. Fuerschbach, P.W., Hinkley, D.A., “Pulsed Nd:YAG laser welding of cardiac pacemaker batteries with reduced heat input,” *Welding Journal*, v 76, 1997, pp 103S-109S.

41. Crafer, R. C., Oakley, P. J.,“Laser Processing in Manufacturing,” Chapman & Hall, New York, 1993.

42. Schloßmacher, P., Haas, T. Schüßler, A., “Laser welding of Ni-Ti Shape Memory Alloy”, SMST-94, Proc. 1st Intl. Conf. On Shape Memory and Superelastic Technologies, A. R. Pelton, D. Hodgson, S. Russell, and T. W. Duerig, MIAS, Monterey, CA, 1994, pp 85-90.

43. Schloßmacher, P., Haas, T. Schüßler, A., “Laser welding of Ni-Rich TiNi Shape Memory Alloy: Pseudoelastic properties”, SMST-97, Proc. 2st Intl. Conf. On Shape Memory and Superelastic Technologies, A. R. Pelton, D. Hodgson, S. Russell, and T. W. Duerig, MIAS, Monterey, CA, 1997, pp 137-142.

44. Schüßler, A., “Micro-Machining and Joining of NiTi-Alloys Using ND:YAG Lasers: Status and Prospects”, SMST-97, Proc. 2st Intl. Conf. On Shape Memory and Superelastic Technologies, A. R. Pelton, D. Hodgson, S. Russell, and T. W. Duerig, MIAS, Monterey, CA, 1997, pp 143-148.

45. Tuissi, A., Besseghini, S., Ranucci, T., Squatrito, F., Pozzi, M.,"Effect of Nd-YAG laser welding on the functional properties of the Ni-49.6at.%Ti", *Materials Science & Engineering A*, v A273-275, 1999, pp 813-817.

46. Hsu, Y. T., Wang, Y. R., Wu, S. K., Chen, C., “Effects of CO_2 Welding on the Shape Memory and Corrosion Characteristics of TiNI Alloys”, *Metallurgical and Materials Transaction A*, v 32A, n 3, 2001, pp 569-576.

47. M. Nishida, C.M. Wayman and T. Honma, “Precipitation processes in near-equiatomic TiNi shape memory alloys,” *Metallurgical Transactions*, v 17A, 1986, pp 1505-1515.

48. Falvo, A., Furgiuele, F.M., Maletta, C., "Laser welding of a NiTi alloy: Mechanical and shape memory behavior," *Materials Science & Engineering A*, v 412, n 1-2, 2005, pp 235-240.

49. Chau, E.T.F, Friend, C.M., Allen, D.M., Hora, J., Webster, J.R., "A technical and economic appraisal of shape memory alloys for aerospace applications," *Materials Science and Engineering A*, v 438–440, 2006, pp 589–592.

50. Hsu, Y. T., Wang, Y. R., Wu, S. K., Chen, C., “Effects of CO_2 Welding on the Shape Memory and Corrosion Characteristics of TiNI Alloys,” *Metallurgical and Materials Transaction A*, v 32A, n 3, 2001, pp 569- 576.

51. Hall, P.C., “Resistance welding Ti-rich Nitinol wire,“ SMST-2000: The Inter. Conf. on Shape Memory and Superelastic Technologies; Pacific Grove, CA; USA; 30 Apr.-4 May 2000, pp 67-75.

52. Shinoda, T., Tsuchiya, T., Takahashi, H., “Functional characteristics of friction welded near equiatomic TiNi shape memory alloy,” *Transaction Japan Welding Society*, v 22, n 2, 1991, pp 30-36.

53. London, B., Fino, J., Pelton, A., Fuller, C., Mahoney, M. “Friction stir processing of Nitinol, “ Proceedings of Friction Stir Welding and Processing III (edited by K.V. Jata, M.W. Mahoney, R.S. Mishra and T.J. Lienert), TMS, 2005, pp 67-74.

54. Van der Eijk, C., Fostervoll, H., Sallom, Z.K., Akselsen, O.M. “Plasma welding of NiTi to NiTi, stainless steel and hastelloy C276,“ Int. Conf. On Joining of Specialty Materials VI, ASM Materials Solutions Conference And Exposition, Pittsburgh, PA, USA, October, 2003.

55. Qiu, X.M., Li, M.G., Sun, D.Q., Liu, W.H. “Study on brazing of TiNi shape memory alloy with stainless steels,” *Journal of Material Processing Technologies,* v 176, 2006, pp 8-12.

56. Kai, A., Kimura, K., Tobushi, H. “TIG welding and shape memory effect of TiNi shape memory alloy,” *Journal of Intelligent Material Systems and Structures*, v 7, n 11, 1996, pp 646-655.

57. Ogata, Y., Takatugu, M., Kunimasa, T., Uenishi, K., Kobayashi, K.F., "Tensile strength and pseudo-elasticity of YAG laser spot melted Ti-Ni shape memory alloy wires," *Materials Transactions*, v 45, n 4, April, 2004, pp 1070-1076.

58. Li, X, Xie, J, Zhou, Y, "Effects of oxygen contamination in the argon shielding gas in laser welding of commercially pure titanium thin sheet," *Journal of Materials Science*, v 40, n 13, pp 3437-3443.

59. Fuerschbach, P.W., Hinkley, D.A., "Pulsed Nd:YAG laser welding of cardiac pacemaker batteries with reduced heat input," *Welding Journal*, v. 76, 1997, pp 103S-9S.

60. Lin, H.C., Wu, S.K., "Tensile behavior of a cold-rolled and reverse-transformed equiatomic TiNi alloy", *Acta Metallurgica et Materialia*, v 42, n 5, 1994, pp 1623-1630.

61. Miyazaki, S., Otsuka, K.,"Development of shape memory alloys", *ISIJ International*, v 29, n 5, 1989, pp 353-377.

62. Otsuka, K., Ren, X. "Physical metallurgy of Ti–Ni-based shape memory alloys," *Progress in Materials Science*, v 50, n 5, 2005, pp 511–678.

63. Van Humbeeck, J., "Shape memory alloys: a material and a technology," *Advanced Engineering Materials*, v 3, n 11, 2001, pp 837-850.

64. Otsuka, K., Wayman, C. M., *Shape Memory Materials*, Cambridge University Press, Cambridge, 1999, pp 53-58.

65. Gil, F.J., Manero, J.M., Planell, J.A., "Effect of grain size on the martensitic transformation in NiTi alloy," *Journal of Materials Science*, v 30, n 10, pp 2526-2530.

66. Ogata, Y., Takatugu, M., Kunimasa, T, Uenishi, K, Kobayashi, K.F, "Tensile strength and pseudo-elasticity of YAG laser spot melted Ti-Ni shape memory alloy wires," *Materials Transactions*, v 45, n 4, 2004, pp 1070-1076.

67. Kudoh, Y, Tokonami, M, Miyazaki, S, Otsuka, K, "Crystal structure of the martensite in Ti-49.2 at.% Ni alloy analyzed by the single crystal X-ray diffraction method," *Acta Metallurgica*, v 33, n 11, pp 2049-2056.

68. Wasilewski, R. J., Butluer, S. R., Hanlon, J. E., Wordon, D., "Homogeneity Range and the Martensitic Transformation in TiNi, " *Metallurgical Transaction*, v 2, 1971, pp 229-238.

69. Wang, F. E., Beuhler, W. J., Pickart, S. J., "Crystal structure and a unique "martensitic " transition of TiNi," *Journal of Applied Physics,* v 36, 1965, pp 3232-3239.

70. Butler, S. R., Hanlon, J. E., Wasilewski, R. J., "On Martensitic Transformation in TiNi," *Metal Science Journal*, v 1, 1967, pp 104-110.

71. Dautovich, D. P., Melkvi, Z., Purdy, G. R., Stager, C. V., "Calorimetric Study of a Diffusionless Phase Transition in TiNi," *Journal of Applied Physics,* v 37, 1966, pp 2513-2516.

72. Tang W., “Thermodynamic study of the low-temperature phase, B19' and martensitic transformation in near equiatomic Ti-Ni shape memory alloys,” *Metallurgical And Materials Transaction A,* v 28A, pp 537-544.

73. Anisimov, S.I., Bonch-Bruevich, A.M., El'yashevich, M.A., Imas, Y.A., Pavlenko, N.A., Romanov, G.S. “The action of powerful light fluxes on metals,” *Zhurnal Tekhnicheskoi Fiziki*, v 36, n 7, 1966, pp 1273-1284.

74. Dabby, FW., Paek, UC, “High- intensity laser- induced vaporization and explosion of solid material IEEE Journal of Quantum Electronics,” v QE-8, n 2, 1972, pp 106-111.

75. Yaws C L, Handbook of Vapor Pressure, Gulf Pub. Co. in, Houston, 1995.

76. Jandaghi, M., Parvin, P., Torkamany, M. J., Sabbaghzadeh, J., “Alloying element losses in pulsed Nd :YAG laser welding of stainless steel 316,” *Journal of Physics D: Applied Physics*, v 41, n 23, 2008, pp 235503- 235509.

77. L.M. Toews, R.B. Gorbet, “The Design and Prototyping of a Monolithic Actuator Using Shape Memory Alloys,” *Proceedings of the 2004 Cansmart International Workshop on Smart Materials and Structures,* Montreal, QC, October 21-22, 2006. pp. 297-306.

78. Cluff, D., Corbin, S., Gorbet, R. "Powder metallurgy fabrication of hybrid monolithic SMA actuators", Cansmart, October, 2009.

79. Khan, M.I. and Zhou, Y (2009), Methods and Systems For Processing Shape Memory Materials, US Provisional Patent, No: 61232243, (Supported by the University of Waterloo Intellectual Property Management Group) Filed: August 2009.